Winter 2007

Modeling and Simulations of Electrical Breakdown and Thermal Failure in Zinc Oxide and Titanium Dioxide for High-Voltage Dielectric Applications

Guogang Zhao
Old Dominion University

MODELING AND SIMULATIONS OF ELECTRICAL BREAKDOWN AND THERMAL FAILURE IN ZINC OXIDE AND TITANIUM DIOXIDE FOR HIGH VOLTAGE DIELECTRIC APPLICATIONS

by

Guogang Zhao

M. S. E. E. March 1994, China Electric Power Research Institute, Beijing, China
B. S. E. E. July 1991, Tsinghua University, Beijing, China

A Dissertation Submitted to the Faculty of
Old Dominion University in Partial Fulfillment
Of the Requirement for the Degree of

DOCTOR OF PHILOSOPHY

ELECTRICAL ENGINEERING

OLD DOMINION UNIVERSITY

December 2007

Approved by:

_____
Ravindra P. Joshi (Director)

_____
Linda L. Vahala (Member)

_____
Karl H. Schoenbach (Member)

_____
Gene J. W. Hou (Member)

ABSTRACT

MODELING AND SIMULATIONS OF ELECTRICAL BREAKDOWN AND THERMAL FAILURE IN ZINC OXIDE AND TITANIUM DIOXIDE FOR HIGH VOLTAGE DIELECTRIC APPLICATIONS

Guogang Zhao
Old Dominion University, 2007
Director: Dr. Ravindra P. Joshi

The development of transmission lines with higher energy storage capabilities is an important goal for compact pulsed power systems. In this context, ceramic dielectrics are promising candidates from the standpoint of high dielectric constants and breakdown strength. Though such materials look promising, their breakdown response characteristics have not been well studied, nor adequately understood. The electrical response of dielectrics also seems to depend on the internal structure and its granularity. For example, the breakdown strength of nano-crystalline insulators such as titania and zinc oxide have been observed to depend on the internal grain size. In general, the hold-off voltage increases monotonically with decreases in grain sizes. For example, nano-crystalline TiO_2 exhibits higher breakdown strength as compared to micron size TiO_2.

In this dissertation, time-dependent, two-dimensional simulations based on random Voronoi networks have been developed to study the electrical breakdown and thermal failure in ceramic dielectrics in ZnO varistors in response to high-voltage pulsing. Our simulations allow for dynamic predictions of internal failures and to track the progression of hot-spots and thermal stresses in samples. The focus is on internal grain-size variations and relative disorder. Our results predict that parameters such as the device hold-off voltage, the average internal temperature, and average dissipated energy density,

and applied pulse-durations would be higher with more uniform grains. Furthermore, scaling down the average grain size offers similar advantages. Finally, it is shown that for the situations studied, the principle failure mechanism arises from internal localized melting, while thermal stresses are well below the thresholds for cracking.

In addition, the somewhat surprising observation of *lower breakdown fields for TiO2 under pulsed conditions as compared to quasi-DC biasing, was studied.* Our simulation results indicated that electrical breakdown of TiO2 under multiple pulsed conditions can occur at lower voltages as compared to quasi-DC biasing. We hypothesize that the lower breakdown voltages observed in TiO2 under pulsed conditions, is a direct rise-time effect, coupled with cumulative detrapping. Finally, the role of granular dielectrics having non-linear, voltage-dependent capacitances on pulse rise-time sharpening was also probed and has been discussed.

ACKNOWLEDGMENTS

I would like to thank my advisor, Dr. Ravindra P. Joshi, for his valuable academic guidance, encouragement, help, support and patience throughout my five years of graduate study. He set a great model for me in my future work. I would also like to thank Dr. Linda L. Vahala, Dr. Karl H. Schoenbach and Dr. Gene J. W. Hou for their kind help as my dissertation committee members and their precious time.

I would also like to acknowledge the Electrical and Computer Engineering Department, for its support all these years. I really enjoyed the time studying at this department.

Great thanks to the great guys in our simulation group, Dr. Qin Hu, Dr. Jun Qian, Ms. Jiahui Song and for all the others for their all kinds of help. And many thanks to my friends, Dr. Feng Wu, Dr. Bing Xiao, Dr. Li Tao, and Dr. Fangsheng Meng, and many others, who gave me great help in daily life, study and research work. Without them my life here cannot be so great and colorful.

Finally, I would like to dedicate my work to my beloved parents, parents in law and daughter in China. Last but not least, I am most thankful and ever indebted to my wife, Ms. Jing Qiao, for her valuable understanding and support.

TABLE OF CONTENTS

LIST OF FIGURES

Figure   **Page**

Figure   **Page**

LIST OF TABLES

CHAPTER I

INTRODUCTION

1.1 Overview

1.1.1 Overview of Zinc Oxide (ZnO) Varistor

Research on ZnO varistors has continued for many decades since its discovery and subsequent utilization in 1968. However, there is still a need for more sensitive and rugged insulation protection levels and more compact, reliable devices, such as gapless-type lightning arresters in high voltage power grids, and surge absorbers (or surge protectors) in relatively low voltage circuits. At present, more than 1 billion pieces of small ZnO varistors are being produced every year for the application of surge absorbers [1]*. While absorbing the energy of a lightning strike or voltage surge, the electrical current flow through the ZnO varistor is typically nonuniform, and will lead to large and spatially non-uniform temperature increases inside the ZnO varistor. Nonuniform distribution of high temperature may result in varistor cracking, puncture or thermal runaway. The following critical issues then arise in this context: (a) How do the cracks or punctures occur, and what is the physical mechanism and process? (b) How could one endeavor to reduce the probability of such occurrences in order to increase device reliability? (c) How could one manufacture arresters or absorbers that are more compact and more effective while reducing failure rates? All of these questions need to be addressed, and this requires further experimentation and simulation studies to understand and probe the various underlying aspects and physics.

---

* The journal format used for this work is the IEEE Transactions on Plasma Science.

1.1.2 Overview of TiO2 (Titania) Dielectrics

TiO_2 is a promising material with a high dielectric constant (89~173 [2]) and high electrical breakdown strength. It has also been shown experimentally that TiO_2 has an internal granular structure and that the nanocrystalline TiO_2 exhibits higher breakdown strength as compared to micron-sized TiO_2. The nanocrystalline TiO_2 dielectric (i.e., a nano-dielectric) is therefore a promising candidate material for the development of transmission lines with higher energy storage capabilities for compact pulsed power applications. In a recent experimental report, Castro *et al.* [3] made a surprising observation during their high field studies on nanocrystalline TiO_2. They observed lower breakdown fields under pulsed conditions as compared to quasi-DC biasing. The "quasi-DC" case consisted of slow ramped voltages starting from an initial zero value, with increases until device breakdown. The pulsed testing was performed with a burst of ten pulses per shot until failure. Usually, the amount of energy deposited during pulsing is much lower than that under dc conditions. Hence, the "hold off" voltage is almost always lower under pulsed conditions. Physically, this occurs because aspects such as thermal runaway, and internal heating related breakdown should be negligible or non-existent under pulsing conditions.

In this dissertation, an attempt is made to explain this observed phenomenon through modeling and simulations. The underlying mechanisms are also probed. Using a one-dimensional, time dependent simulation model, the experimental observations will be analyzed and explained in the following chapters.

1.1.3 Overview of Nonlinear Transmission Line Based on Barium Strontium Titanate (BST) Dielectrics

The molecular formula of BST is $Ba_xSr_{1-x}TiO_3$, and BST is dielectric with voltage-dependent, nonlinear properties. This mainly arises from its permittivity, which is electric field dependent [4]. The higher the field, the lower the permittivity. Besides, the permittivity level at any field is typically orders of magnitude higher than other semiconductors and ceramics. Capacitors made using BST dielectrics also show a non-linear field-dependence [4]. In addition, thin-film BST also exhibits a high breakdown field above 0.6 MV/cm [5] and, hence, is an excellent candidate for "high-voltage" technology development. Thus BST is a promising candidate material for a nonlinear transmission line, which could be used to generate ultra-short rise-time pulses (or pulse sharpening) for potential usage in pulsed power applications.

In this dissertation, numerical simulations are carried out to study the possibility of using BST in pulsed-power, high-voltage applications. Specifically, its field dependent capacitance is analyzed for use in pulse sharpening. Our results clearly demonstrate rise-time shortening in agreement with published experimental data. Our research can also be used as a design and optimization tool for non-linear transmission lines for pulsed power applications.

1.2 Scope of the Dissertation Research

This work mainly focuses on the modeling and simulation aspects. Three different issues are probed and analyzed. All three are connected to the general area of high-

voltage, pulsed-power engineering. The three aspects probed in this dissertation research are: (i) ZnO varistor electrical breakdown and thermal failure processes, (ii) TiO_2 electrical breakdown under pulsed conditions, (iii) BST nonlinear capacitance calculations and their application to pulse sharpening based on nonlinear transmission lines. Through theoretical analysis and numerical simulation tools, the objective is to get a good understanding of: (i) ZnO varistor electrical breakdown and thermal failure processes and mechanisms. The relative role of the various underlying phenomena and their quantitative assessment is carried out. (ii) The physics of TiO_2 electrical breakdown under pulsed conditions, together with relevant analyses. Potential differences in the breakdown process with regards to dc biasing will also be probed. (iii) Pulse sharpening using BST material based nonlinear transmission lines. The subsequent and broader goal is to provide performance predictions and suggestions for the design, fabrication and system enhancement for given applications.

In this dissertation, chapter 2 provides the relevant literature review and reports on the background knowledge. Some discussions pertaining to the internal mechanisms associated with our models is also given. In chapter 3, the detailed physical models are presented. The approaches and simulation scheme used in this dissertation research are described and explained in detail. Next, chapter 4 shows the results obtained based on the models of chapter 3 and presents detailed discussions of these results. A summary and conclusion of the present research is given in chapter 5. This last chapter also includes suggestions for possible future work.

CHAPTER II

LITERATURE REVIEW AND BACKGROUND

2.1 Introduction to ZnO Varistors

Zinc Oxide (ZnO) varistors (variable resistors) are ceramic semiconductor devices exhibiting highly nonlinear current-voltage characteristics similar to back-to-back Zener diodes but with much greater energy handling capability [6]. The primary function of ZnO varistors is to clamp the transient voltage to a level that is not harmful to the protected electrical or electronic devices and systems. At the same time, the ZnO varistors are capable of absorbing transient surge energy that can protect critical electrical components and devices. ZnO varistors have now been in widespread use for more than 30 years. Applications of ZnO varistors are predominantly in the field of circuit overvoltage protection. Overvoltage protection is necessary for both electronic circuits and in the electrical power distribution and transmission industries. The technology has supplanted generally less useful prior approaches to voltage surge protection such as silicon carbide (SiC) arresters, gas discharge tubes and to some extent semiconductor-based surge suppressors such as Zener diodes. A significant advantage of ZnO varistors as a transient protective device derives from the ceramic nature of the material. The material is polycrystalline with energy absorption occurring essentially at the grain boundaries distributed throughout the volume of the material. Hence, ZnO varistors are inherently able to absorb more energy than single-junction protective devices such as Zener diodes [7].

More than one billion ZnO varistor devices are in service. They protect circuits with voltages ranging from around 10 volts to millions of volts. The larger devices are capable of surviving transient currents greater than 100,000 amperes and can absorb energies greater than 10,000 joules (energy absorption capability > 200 J/cm^3 is routinely available) [7].
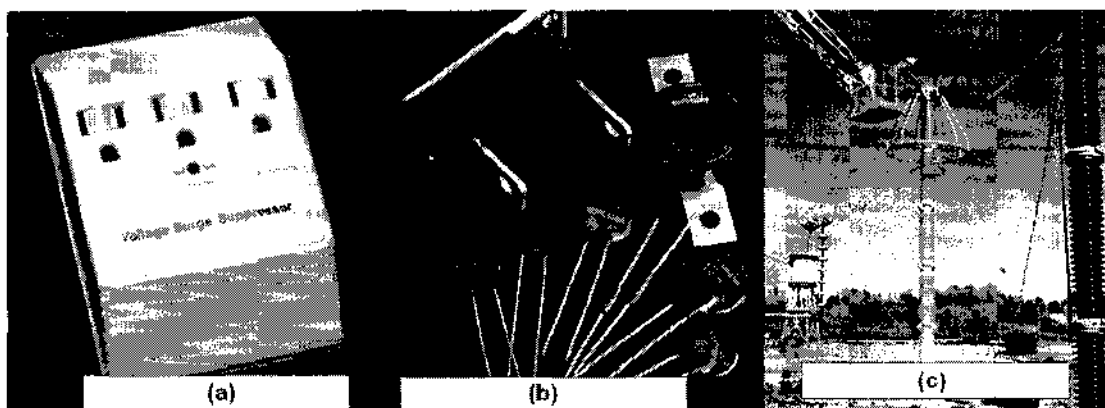
Figure 2-1. Various applications of ZnO varistors. (a) Consumer surge protector; (b) Commercial ZnO varistors; (c) High voltage ZnO arrestors used in power system. After [7].

Consumer-purchased surge-suppressor electrical outlets based on ZnO varistor technology are commonly used to protect computers and other high value electronic equipment.

In addition to the protection of electronic equipment, a major application of ZnO varistors is for the protection of electric power distribution and transmission systems. In these applications, a surge suppressor is required to function reliably on systems with voltages ranging up to a megavolt and to absorb transient energies in the megajoule range. Large volumes of varistor material are needed to meet these requirements [7].

ZnO varistors have found acceptance as a simple, cost-effective way to protect electrical systems from transient voltage surges. By virtue of their ceramic nature, they

can be fabricated into a variety of sizes and shapes, and this feature facilitates a high degree of user flexibility. Varistors are inherently multijunction grain-boundary devices and any transient surge energy absorbed when the device acts in a protective mode is distributed among the many ZnO grain junctions. The multijunction feature of varistor behavior is the heart of the high-current and energy-absorption capability of the material [7].

2.2   Fabrication Methods

The ZnO varistors are produced by sintering ZnO powder with small amount of other metal oxide additives, such as Bi_2O_3, CoO, MnO and Sb_2O_3. A standard molar ratio of composition is Bi_2O_3 : MnO : CoO : S b_2O_3 : ZnO = 0.5 : 0.5 : 1 : 1 : 97. The tolerance toward the increase of the molar percentage of the additives is fairly large. Even if one adds double the amount of additives, one can expect good varistors. The powders are mixed by a conventional method using a mortar in dry form or a ball mill in wet form. After drying, the mixture is pressed into arbitrary forms, such as disks of 3-100 mm in diameter and 1-30 mm thickness, by a conventional molding method. The pressed disks are sintered in an electric furnace at 1150-1350°C for 1-5 hours in air. The temperature is increased or decreased at 50-200°C per hour. Finally, electrodes are prepared on both surfaces. The best ohmic electrodes are painted In-Ga alloys or evaporated Al films. In order to obtain high-performance ZnO varistors, the compositions, impurities, mixing methods, particle sizes, and sintering conditions (maximum temperature and holding time, temperature rising and/or lowing rates, oxygen and Bi_2O_3 partial pressures) should be controlled precisely [1].

2.3 Electrical Characteristics

ZnO varistors have highly non-ohmic current-voltage (J-V) characteristics above a threshold voltage. Since the range showing the highly non-ohmic property is wide, the J-V characteristics are usually expressed logarithmically and are classified into three regions, as shown in Figure 2-2. The observed current-voltage characteristic of varistors is often empirically described by the power-law relation [8]:

$$J = kV^{\alpha} ,\qquad\qquad (2\text{-}1)$$

where k is a constant, and the non-ohmic exponent $\alpha = \dfrac{d(\ln J)}{d(\ln V)}$ is a measure of the device nonlinearity, and it varies with voltage. α is also called the nonlinearity coefficient. When $\alpha = 1$, it is an ohmic resistor, and when $\alpha = \infty$, it is an ideal varistor, as can be seen from Figure 2-3(b). Typical α values of ZnO varistors range from 30 to 100, and these devices have excellent current and energy absorption capabilities. On the contrary, α values of conventional varistors such as SiC varistors do not exceed 10 [1]. This is why SiC varistors have been totally replaced by ZnO varistors used in arresters.

The J-V characteristics of ZnO are classified into three regions, as shown in Figure 2-2. In region I, below the threshold voltage (typically a voltage at 1 $\mu A/cm^2$), the non-ohmic property is not so prominent and is highly dependent on temperature. In region II, between the threshold voltage and a voltage at a current of about $100 A/cm^2$, the non-ohmic property is very prominent and almost independent of temperature. In region III, above 100 A/cm^2, the non-ohmic property gradually decays. ZnO varistors are characterized by the magnitude of the α values and the width of the range where the highly non-ohmic property is exhibited [1].
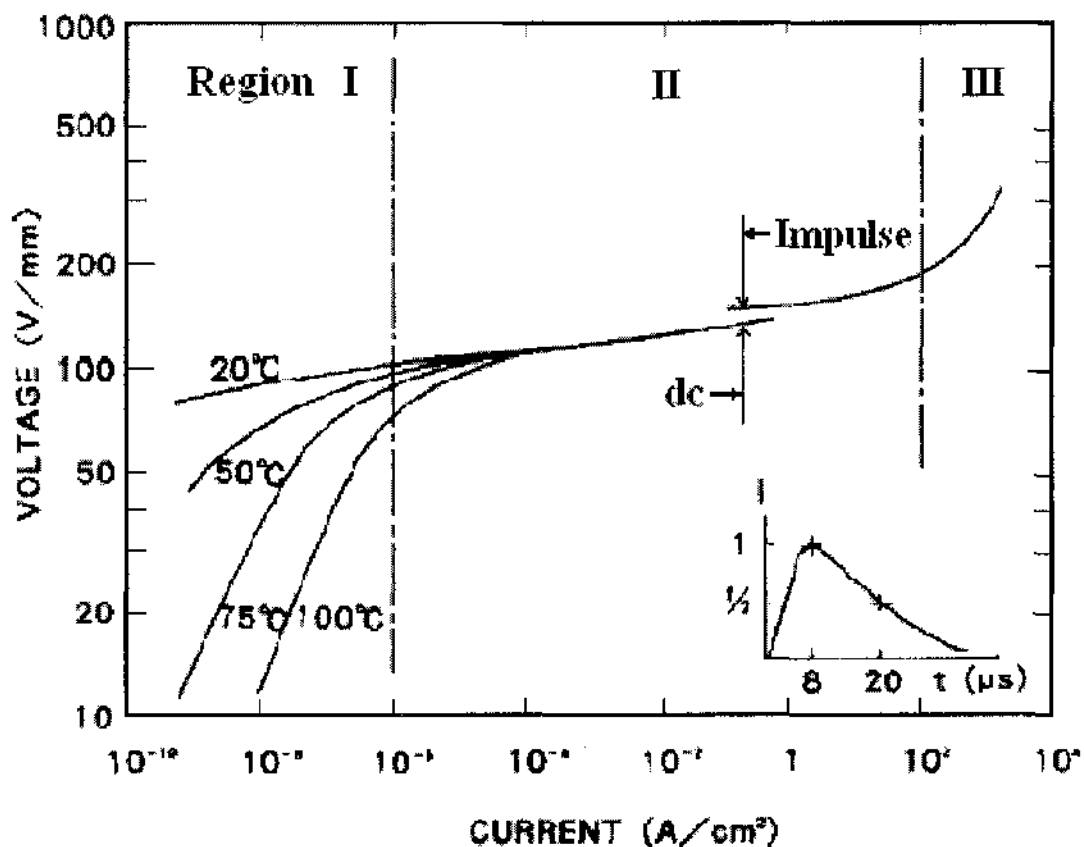
Figure 2-2. *J-V* characteristics of a typical ZnO varistor. Usually *J-V* characteristics below 100 mA/cm2 are measured by DC, and those above 1 A/cm^2 are measured by impulse currents, whose waveform is shown at the lower right corner. The voltages measured by the impulse currents are slightly higher than those measured by DC as shown by the arrows. The discrepancy is caused by the response delay of the varistor. After [1].

The *J-V* characteristics below 100mA/cm^2 are usually measured using a DC electric source, whereas those above 1 mA/cm^2 are measured by an impulse current source to avoid heat generation and thermal breakdown. The waveform of the impulse current is an 8-μs rise time and 20-μs decay time up to one-half the peak value, as shown in Figure 2-2. This waveform is used as a standard impulse current to test lightning arresters. The *J-V* characteristics measured by the impulse currents show voltages higher than those measured using DC. The discrepancy is usually 10%-20%, as shown by the arrows in

Figure 2-2. This discrepancy is caused by the delay of electrical response in the ZnO varistors. The response delay is speculated to be caused by electron trapping and hole creation at the grain boundaries [1].
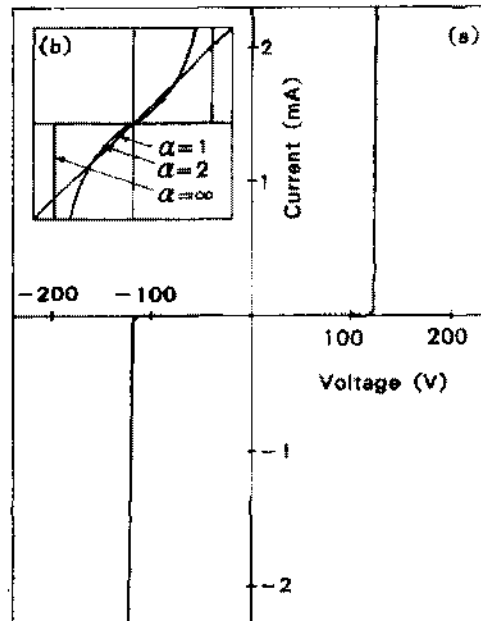
Figure 2-3. ZnO varistors are voltage-dependent switching devices. (a) Current–voltage curve of a typical ZnO varistor. (b) Schematic *J-V* curves for different α values. After [1].

Another important electrical characteristic of ZnO varistors is their dielectric properties. Below the threshold voltage, ZnO varistors are highly capacitive. The dielectric constant of ZnO is 8.5, whereas an apparent dielectric constant of a ZnO varistor is typically 1000. The dielectric properties are mainly caused by thin depletion layers (~100nm) at the grain boundaries [1].

2.4   Microstructure

ZnO varistors are polycrystalline materials composed of semiconducting ZnO grains (Figure 2-4) with a distribution of internal grain sizes. The grain size varies in the range of 5 μm -30 μm according to its recipe and fabrication technologies. The resistivity of a ZnO grain is 0.1-1.0 Ωcm. The grain boundaries are shown in Figure 2-5. The thickness of grain boundary varies in the range of several nanometers to several tens of nanometers.
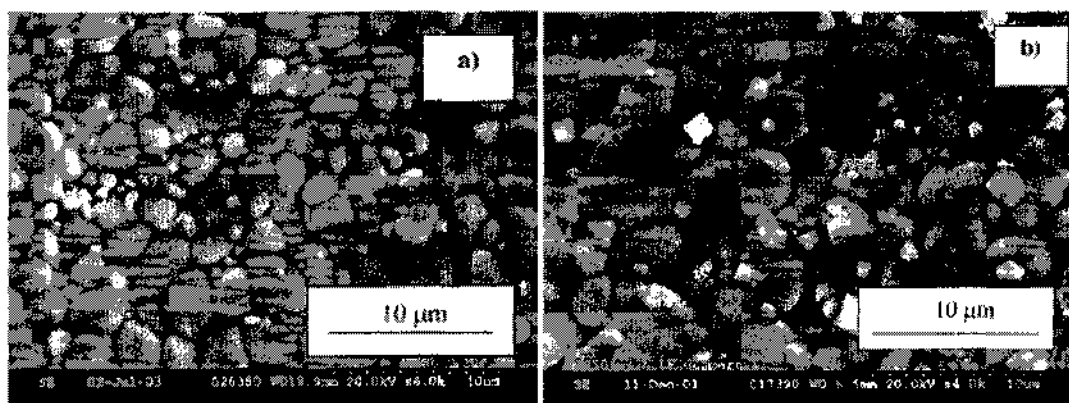
Figure 2-4. FESEM images of the ZnO varistor samples sintered at 1050 °C. (a) "Core-shell" samples, and (b) Commercial samples. After [9].
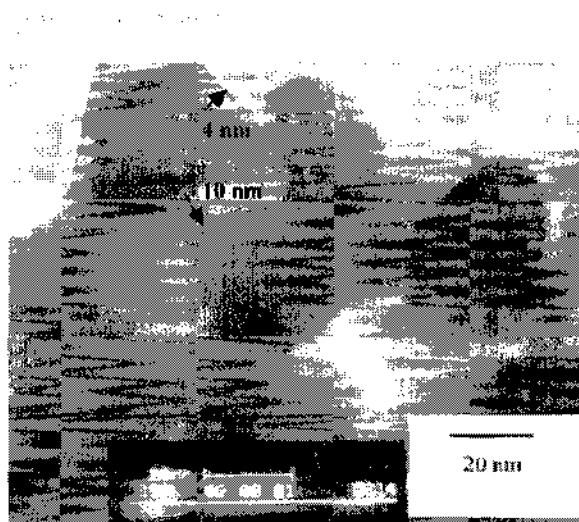
Figure 2-5. HRTEM of ZnO grain boundaries consisting of (Sb, Bi and Co) oxide precursors. After [9].

Tao *et al.* [10] measured the electrical characteristics of a single ZnO varistor grain-to-grain junction. The experimental results are described in statistical terms because each single barrier has been found to present its own electrical characteristics. They gave out the distributions of barrier voltages and nonlinear coefficients of single grain boundary, as
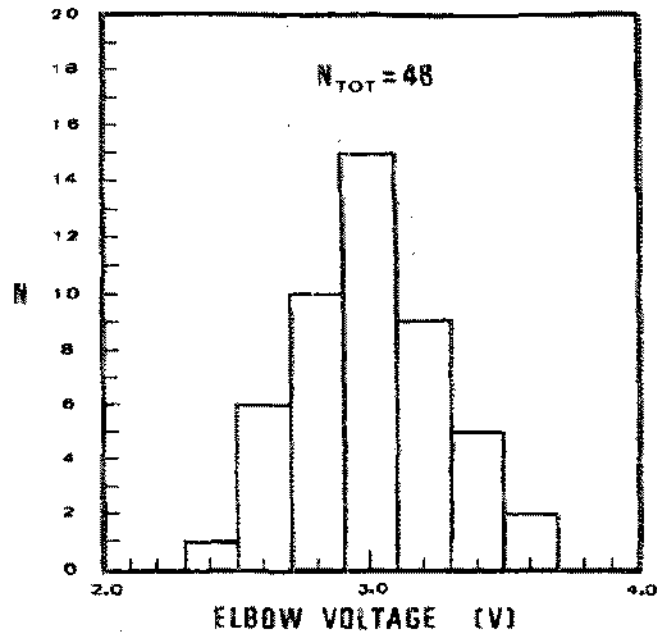
Figure 2-6. Histogram of barrier voltage V_B, proposed by Tao [10].

shown in Figure 2-6 and Figure 2-7. Based on this distribution of nonlinear coefficients, Tao *et al.* classified the barriers into two groups: (1) "good" junction (i.e. with high nonlinearity) and (2) "bad" junction (i.e. with poor nonlinearity). Later, Bartkowiak and Mahan [11] extended this classification and proposed the third group, (3) "ohmic" barrier (i.e. linear with low-resistivity), and gave out the typical J-V characteristics of these three kinds of microjunctions, listed in Equations (2-2), (2-3) and (2-4). The J-V characteristics are shown in Figure 2-8.
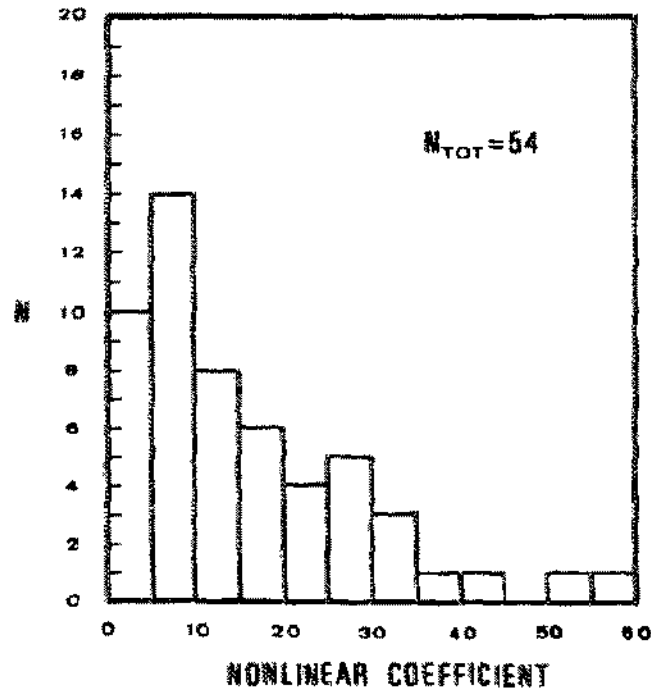
Figure 2-7. Histogram of nonlinear coefficient α, proposed by Tao [10].

A "good" microjunction characteristic is described by the switching function[11]:

$$
J(V) = \begin{cases}
\dfrac{V}{R_g}\left[1 + \dfrac{V^{50}}{V_B^{50}}\right] & for \quad V \le V0_g \\[4mm]
\dfrac{V}{R_g}\left[1 + \dfrac{V0_g^{\,50}}{V_B^{50}}\right]^{7/2}\left[1 + \dfrac{V0_g^{\,70}}{V_B^{50}V^{20}}\right]^{-2.5} & for \quad V > V0_g
\end{cases}
, \qquad (2\text{-}2)
$$

where $R_g = 10^9$ $\Omega \cdot cm^2$, the leakage resistance of a unit area of grain boundary; $V0_g = 3.467$ V and is a switching point of Equation (2-2), and $V_B = 3$ V is the breakdown voltage of the junction (barrier voltage). Basically, V_B is the voltage for which the nonlinearity coefficient α reaches half of its maximum and corresponds to the position of the "knee" of the characteristic.

Similarly, the "bad" grain boundary J-V characteristic is [11]:

$$J(V) = \begin{cases} \dfrac{V}{R_b}\left[1+\dfrac{V^{50}}{V_B^{50}}\right]^{1/5} & for \quad V \leq VO_b \\[2em] \dfrac{V}{R_b}\left[1+\dfrac{VO_b^{50}}{V_B^{50}}\right]^{1/5}\left[1+\dfrac{VO_b^{55}}{V_B^{50}V^5}\right]^{-2} & for \quad V > VO_b \end{cases} \quad , \tag{2-3}$$

where $R_b = 10^7 \quad \Omega \cdot cm^2$, $VO_b = 3.622 \ V$, and $V_B = 3 \ V$.

Finally, the ohmic grain boundaries have a linear characteristic [11] of the form:

$$J(V) = \frac{V}{R_o} \ , \tag{2-4}$$

where $R_o = 2 \times 10^5 \quad \Omega \cdot cm^2$, the resistance of a unit area of the boundary.
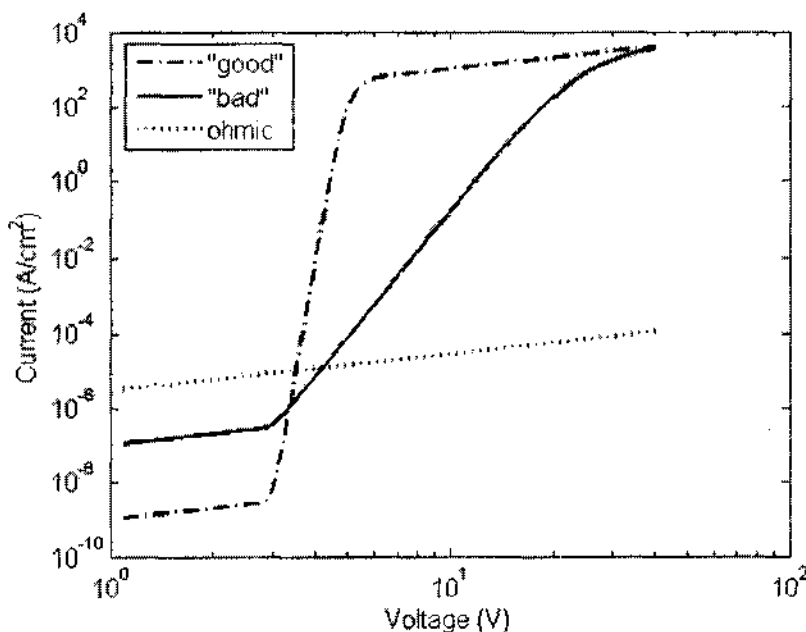
Figure 2-8. J-V characteristics of the three kinds of grain boundaries. After [11].

As shown in Figure 2-8, the microjunctions referred to as "good" have high leakage resistance and high nonlinearity (i.e., $\alpha \geq 30$). Estimates of the relative number of such good microjunctions have been reported to vary from 15% to 60%. "Bad" micro-junctions have 2-3 orders of magnitude lower leakage resistance and much lower

nonlinearity (i.e., $\alpha \approx 10$), and their relative number is around 30%-35%. Finally, Ohmic, or nearly ohmic, microjunctions with resistance 2-5 orders of magnitude lower than the leakage resistances of the good junctions are also found, and their number has been estimated to be between 5% and 10%.

Based on the large amount of published experimental measurement data, in 2002 Chen *et al.* [12] further proposed that the nonlinearity coefficient α of the ZnO grain boundary follows a normal distribution, given as:

$$p(\alpha) = \frac{1}{\sqrt{2\pi} \times 50} \exp\left[\frac{(\alpha - 7)^2}{2 \times 50^2}\right], \quad \alpha \geq 1. \tag{2-5}$$

More recently in 2004, He *et al.* [13] revised it to an **exponential distribution**:

$$p(\alpha) = ae^{-b\alpha}, \quad \alpha > 0 \quad , \tag{2-6}$$

where a = 0.27 and b = 0.053. The accumulating probability $P(0 < x \leq \alpha)$ for such an exponential distribution can be calculated by:

$$P(0 < x \leq \alpha) = \int_0^\alpha ae^{-bx}dx \quad . \tag{2-7}$$

Actually, both distributions match Tao's experimental histogram shown in Figure 2-7. The above formula can be used in numerical simulations and calculations. The constants *a* and *b* can be modified by special application [13]. This model not only incorporates the characteristics of "good", "bad" and "ohmic" junctions together in a quantitative manner, but also makes progress towards describing the complexity of ZnO grain boundaries.

The barrier voltages per grain boundary are 3.3 V according to Mahan *et al.* [1, 14] and 3.6 V according to Kemenade *et al.* [15] as determined by using direct measuring

methods. A number of other researchers have also measured and reported values for the breakdown voltage based on different direct methods. The reported breakdown voltages lie in a range from 1.8 to 6.0 V, which covers a wide parameter space [13]. One explanation for this relatively wide range of results is the difficulty in defining the cross-sectional area. In addition, different criteria were used to measure the breakdown voltages. Even if the same criteria are to be used (e.g., at 1 μA or at the maximum of the nonlinearity coefficient α), the barrier voltages could still be largely different because of variations in prescription, sintering courses and processing details. Jinliang He [13] reported a statistical average value of 3.3 V and proposed that this barrier voltage follows a **normal distribution** with a **mean value of 3.3 V** and **standard deviation** between **0.02 and 0.2 V**.

The breakdown voltage of the sintered body is proportional to the number of grain boundaries between the two electrodes. This indicates that the breakdown voltage is proportional to the inverse of the ZnO grain size. Small grain sizes result in high threshold voltages per unit thickness. The sizes of ZnO grains are usually 5μm -30μm and depend on the material composition, sintering temperature, and time. Sb_2O_3 or SiO_2 are elements used to suppress grain growth. On the contrary, TiO_2 or BeO promotes grain growth. Higher temperatures and longer sintering times also result in large ZnO grains. However, bismuth oxide easily vaporizes above 1400°C [1], and if Bi_2O_3 vaporizes extensively, the non-ohmic property will disappear. The presence of Bi_2O_3 is therefore thought to be responsible for the highly nonlinear current-voltage (J-V) characteristics.

The microstructures at the grain boundaries are quite complicated. They are roughly classified into three types of structures [16-19]. The first one (type I) is the grain boundary having a relatively thick (0.1-1μm) Bi_2O_3-rich intergranular layer, as depicted in Figure 2-9. The melting point of Bi_2O_3 is 820°C [1]. Hence, a liquid phase is likely to gather at the holes created by the packing of the ZnO grains. Therefore, one can easily find the thick Bi_2O_3-rich intergranular layers at the packing holes in the sintered body. The Bi_2O_3-rich intergranular layer becomes thinner (1-100nm) as it approaches the contact points of the particles. This is labeled a type II structure, as shown in Figure 2-7. Finally, at the contact points no distinct intergranular layer can be observed by a scanning electron microscope (SEM) or transmission electron microscopy (TEM). This is called a type III structure, as shown in Figure 2-7. For the type III structures, Bi, Co, and an excess amount of oxygen ions were detected in the interfacial region of the grain boundaries at a thickness of several nanometers by Auger electron spectroscopy (AES) or x-ray photoelectron spectroscopy (XPS) measurements [1].
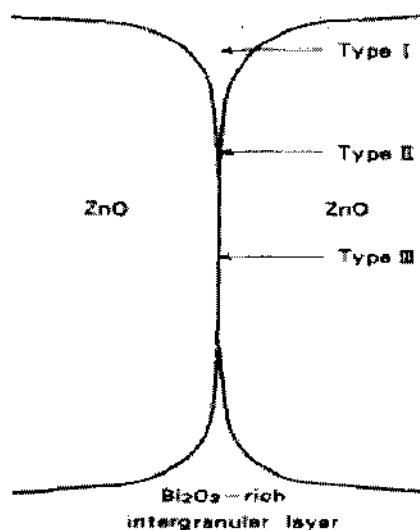
Figure 2-9. Schematic microstructure of a ZnO varistor. Type I has a fat (0.1-1μm) Bi_2O_3-rich intergranular layer ; type II has a lean (10-1000⊕) Bi_2O_3-rich intergranular layer; Type III has almost no intergranular layer, except for excess amounts of Bi, Co, O ions, etc. After [16].

The occupation ratio among these three types of microstructure is quite different and dependent on both composition (especially Bi_2O_3 content) and sintering conditions. The ZnO varistors with 0.5 molar percentage of Bi_2O_3 added to the starting material and sintered at 1250°C for 2 hours, have mainly the type II and III structures, whereas the varistors sintered at 1400°C for several hours have mainly the type III structure. The varistors with more than 5 molar percentage Bi_2O_3 added to the starting material mainly have the type I structure. Even in this case, highly non-ohmic properties are still observed [16].

2.5 Conduction Mechanisms

Currently, the conduction mechanism in the ZnO varistor is still not very clear. However, several possible mechanisms have been proposed and are listed below:

1) "Space-charge-limited current (SCLC)" by Matsuoka in 1971 [6];

2) "Tunneling through a thin layer at the grain boundary" by Levinson and Philipp in 1975 [20];

3) "Tunneling through Schottky barriers caused by interface states" [21-26]. In this case, there were two models proposed. One did not take into consideration the heterojunctions composed of ZnO and the Bi_2O_3-rich intergranular layer [21-24]. These reports supposed that the type III structure as described earlier was essential for the highly non-ohmic property. The other model took into consideration the heterojunctions [25,26];

4) "Tunneling through Schottky barriers with hole creations" [8]. This model demonstrated the importance of minority carriers (holes) at the grain boundaries;

5) "Tunneling through homojunctions of ZnO" [27, 28], which pointed out the importance of thermal equilibrium of defects formed during cooling at the grain boundaries;

6) "Hole-induced breakdown" [29-33]. The energy band diagram proposed by Pike and Kurtz [30] is shown in Figure 2-8. According to their theory, the highly non-ohmic property is caused by lowering of the potential barriers at the grain boundaries due to hole accumulation. The holes are created by accelerated electrons in the depletion region. The potential barriers depend both on the interface states and the bulk traps;

7) "Bypass effect" [34, 35], which represented the important role of the Bi_2O_3-rich intergranular layer in the small current region and supposed that parallel current paths through the heterojunctions and the Bi_2O_3-rich intergranular layers should be considered;

8) "Induced space-charge current at the heterojunctions" composed of thin films of ZnO and Bi_2O_3 [36].

Of these various proposed mechanisms, the "hole-induced breakdown" model is consistent with the highly non-ohmic property, the high α values, the interface state effects, the bulk trap effects, the hole creation mechanism, and the dynamic properties. The production of holes by impact ionization in the depletion region near the grain boundaries during the electrical breakdown of varistors, and the recombination of these holes with free electrons have been directly verified by electroluminescence experiments [31]. This is why most researchers have accepted this conduction mechanism. The underlying theory behind this mechanism is briefly introduced in the following paragraph.
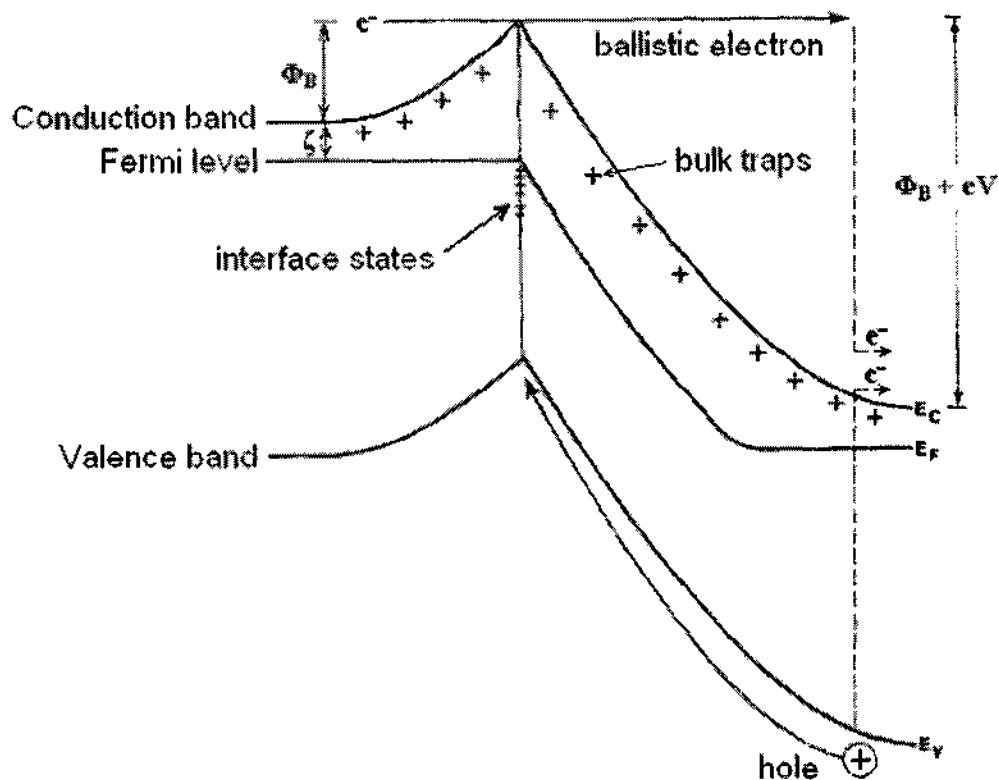
Figure 2-10. Energy band diagram near a varistor grain boundary under applied voltage V. Electrons trapped at the boundary cause a double depletion layer structure of ionized donors to form. Ec, Ev, and E_F are respectively the conduction band, valence band, and the Fermi level. The process of interband impact ionization for the thermionic emission model is shown. After [31].

In the micro-structured ZnO devices, energy states are created due to dislocations and dangling bonds arising from the crystallographic mismatch between adjacent grains. As shown in Figure 2-10, free carriers (usually electrons present in the slightly n-type ZnO material) are trapped, leading to the creation of electro-static barriers at the interface. Thus, a thin interfacial charged layer sandwiched between depletion regions with donor charge on either side is formed. The potential barrier prevents current conduction and offers the large impedance at relatively low voltages. At increasing external bias, asymmetric "band bending" results and leads to nonlinear increases in current with voltage.

Eventually, electrons moving downstream, past the barrier, generate minority holes through impact ionization. The back-flow of holes towards the barrier, and the annihilation of electrons trapped within the interface states, reduces the effective barrier height. The net effect is a dynamic current increase leading to eventual breakdown. Thus, the breakdown processes and their dynamics are dictated by the following aspects: (i) The height (hence, interface charge) of each GB, (ii) The semiconductor band-gap that influences the downstream hole generation through impact ionization. (iii) The detrapping rate that dynamically leads to barrier reductions. (iv) The number of grain boundaries present in a given sample, and hence, the average grain size. Samples with smaller grains present higher breakdown voltages. (v) The operating (or localized) temperature since carrier mobilities, thermionic emission rates past the GB barrier, impact ionization parameters and electron-hole capture rates are all temperature dependent. Internal heating and temperature increases can naturally be expected to influence the breakdown thresholds and sequential dynamics as well. Unfortunately, the electro-thermal aspects have not been studied extensively in the literature.

2.6 Energy Absorption Capability and Failure Modes

The nonohmic property of the ZnO varistor is caused by grain boundaries in the polycrystalline-sintered body. Therefore, the ZnO varistors are multijunction devices composed of a number of tiny nonohmic devices connected in parallel and in series. As a result, generally speaking, a thicker device has a higher threshold voltage, and a device having a wider electrode area has greater energy handling capability. In actuality, however, the polycrystalline-sintered body is not uniform, so the energy handling

capability does not increase proportionally with the electrode area. The energy handling capability is one of the most important properties for application to transient surge suppression [37]. It can be defined as the amount of energy that a varistor can absorb before it fails [38, 39].

There are three main failure modes of varistor elements: **thermal runaway, puncture, and cracking**. The leakage current and, consequently, the Joule heating of a varistor increase with temperature. Thus, if the temperature is raised above the thermal stability temperature T_s (around 200°C), power input may exceed heat dissipation, and thermal runaway may occur, as illustrated in Figure 2-11.
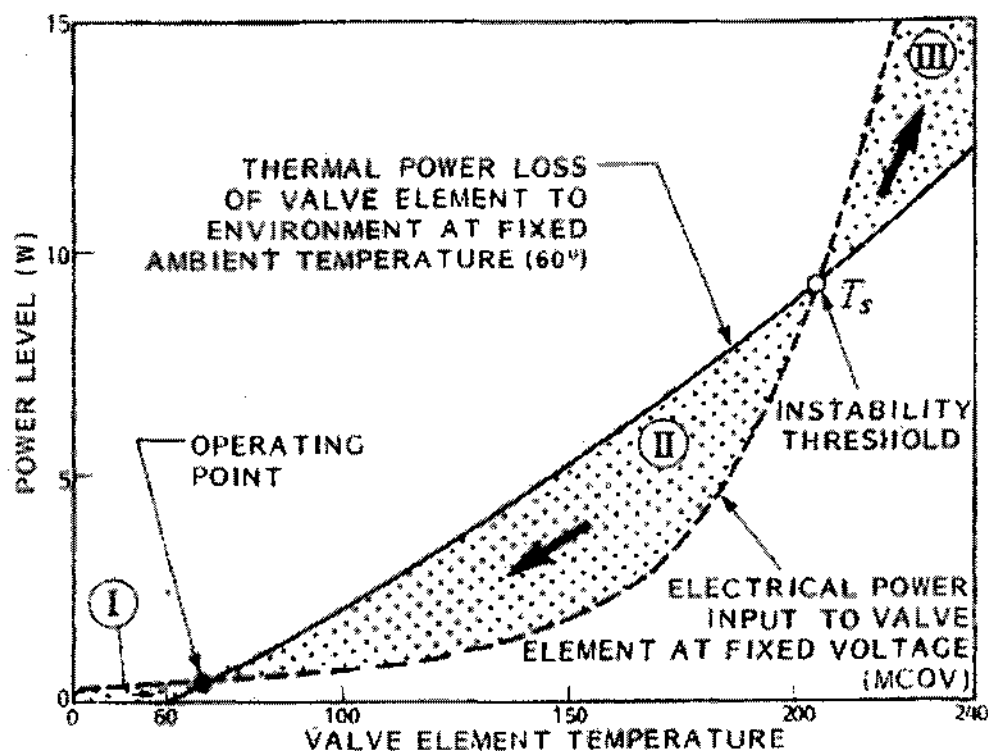
Figure 2-11. Evaluation of ZnO varistor steady state stability using the heat loss-input balance diagram. After [40]. Note: "**valve element**" refers to ZnO disk used in arresters.

As shown in Figure 2-11, the power dissipation of a typical valve element (i.e. a ZnO disk)(presented with broken line), due to a constant applied 60 Hz voltage, is extremely temperature dependent. At the same time, the ability of the element structure to dispose of heat is nearly proportional to its temperature rise above the ambient (presented with solid line). Consequently, there are two intersections of the two curves: one at low temperature — a so-called stable operating point, and the other at high temperature — a so-called instability threshold. To obtain thermal stability, the electrical power dissipation in the element must be balanced against heat output to the environment. If power dissipation exceeds heat losses from the element (regions I and III in Figure 2-9), then excess energy is stored in the element, and its temperature slowly increases. Conversely, if heat loss exceeds power dissipation, temperature of the element decreases (region II in Figure 2-9). Consequently, the valve element temperature always settles at the stable operating point between regions I and II, as long as the initial valve temperature does not exceed the instability threshold. As the two characteristics diverge beyond the instability threshold point, a thermal runaway will invariably result from element temperature excursions above this point [40].

In device puncture, a small hole results from melting of the ceramic in a region where high current is concentrated [37, 39], as shown in Figure 2-12 [41]. Nonuniform heating can also cause thermal stresses higher than the failure stress of the material and can lead to cracking, shown in Figure 2-13 [42]. Currents in the nonlinear region of the J-V characteristics tend to concentrate into a few narrow paths. This nonuniform current distribution has been detected by applying small spot electrodes to the surfaces of varistor disks, by using infrared thermo-cameras, and by electroplating techniques.

Cracking and puncture are caused by a localization of the current, which causes local heating leading to nonuniform thermal expansion and thermal stresses. Puncture is the dominating failure mode for only slightly nonuniform disks, but cracking becomes more likely as the degree of nonuniformities increases [43].
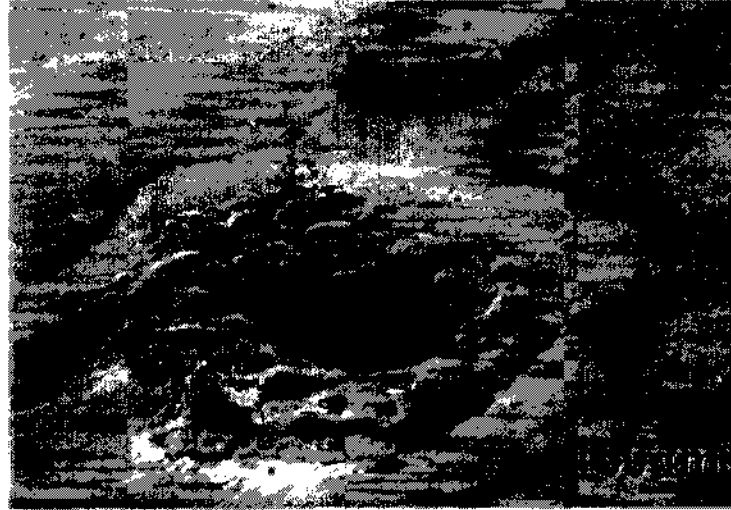
Figure 2-12. Scanning electron micrograph of a ZnO varistor sample failed in the puncture mode. After [41].
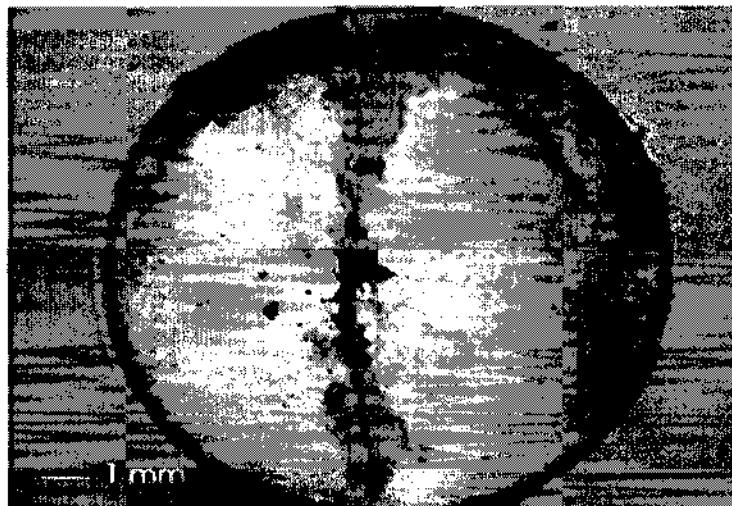
Figure 2-13. Cracking sample degraded with long current pulses. After [42].

Puncture is most likely in varistor disks with a low geometrical aspect ratio (i.e., height : diameter) when the current density has intermediate values. Cracking dominates at higher current densities and for disks with a high aspect ratio. Puncture and cracking do not occur when the current is small because the time evolution of the nonuniform heating is slow enough for the temperature distribution to flatten. They are also unlikely at very large currents corresponding to the upturn region of the J-V characteristic, since in this case the current becomes uniformly distributed. For low and very high current densities the most likely failure mode is thermal runaway [38, 39, 43].

The energy handling capability at high currents strongly depends on the position of the upturn region in the varistor J-V characteristic. This position is determined by the resistivity of ZnO grains, and can be controlled by the level of aluminum doping. Therefore, it is possible to minimize the change of a failure of varistor disks by adjusting this resistivity to the requirements of particular applications [43].

Chen [12] studied the distribution of temperature and thermal stress in ZnO varistor with computer simulation and proposed that the temperature difference and the thermal stress in ZnO varistor ceramics can be greatly decreased by increasing the uniformity of ZnO grain size or decreasing the average size of ZnO grains to improve the surge energy absorption capability of the ZnO varistors. The uniformity of ZnO grain size is hard to improve due to the limitation of the fabrication technology, but the average size of a ZnO grains can be controlled by inhibiting the grain growth during the manufacture process, which can be realized through the use of additives, milling the raw material to smaller particles, or decreasing the sintering temperature and so on.

2.7 Introduction to TiO$_2$ and Its Surprising Breakdown Property

The development of various robust components such as transmission lines with higher energy storage capabilities is an important goal for compact pulsed-power systems. In this context, ceramic dielectrics are emerging as promising candidates from the standpoint of their high dielectric constant and breakdown strength. High dielectric constant (ε) ceramic materials can lead to shorter pulse forming lines, since the length L scales as: $(ct_{pulse})/\varepsilon^{\frac{1}{2}}$. Other advantages include a lower system impedance Z (since $Z \sim \varepsilon^{-1/2}$) and larger energy storage capability.

Though such materials look promising, their breakdown response characteristics have not been well studied, nor adequately understood. The electrical characteristics of dielectrics also seem to depend on the internal structure and its granularity. For example, the breakdown strength of nano-crystalline insulators (e.g., titania) has been observed to depend on the internal grain size. In general, the hold-off voltage increases monotonically with decreases in grain sizes [8, 32, and 44-47]. The low conductivity and high hold-off voltage in these materials arise from the presence of a fixed charge at grain boundaries that establishes localized Schottky barriers to charge transport. Samples with smaller average grains present more barriers for a given length; hence, there is a larger impediment to conduction. In Castro's experiments [3], nano-crystalline TiO$_2$ was seen to exhibit higher breakdown strength as compared to micron sized TiO2 as shown in Figure 2-14. The breakdown strength of Figure 2-14 is given as a function of dielectric thickness for both nano-crystalline and coarse-grained TiO$_2$. It can be seen that as the dielectric thickness increases, the electrical breakdown strength decreases. This could arise from the increased likelihood of internal flaws and defects as the material volume is

increased. Examples of flaws include air bubbles, increased pore sizes between crystals due to sintering, and mechanical failures such as micro-cracks.
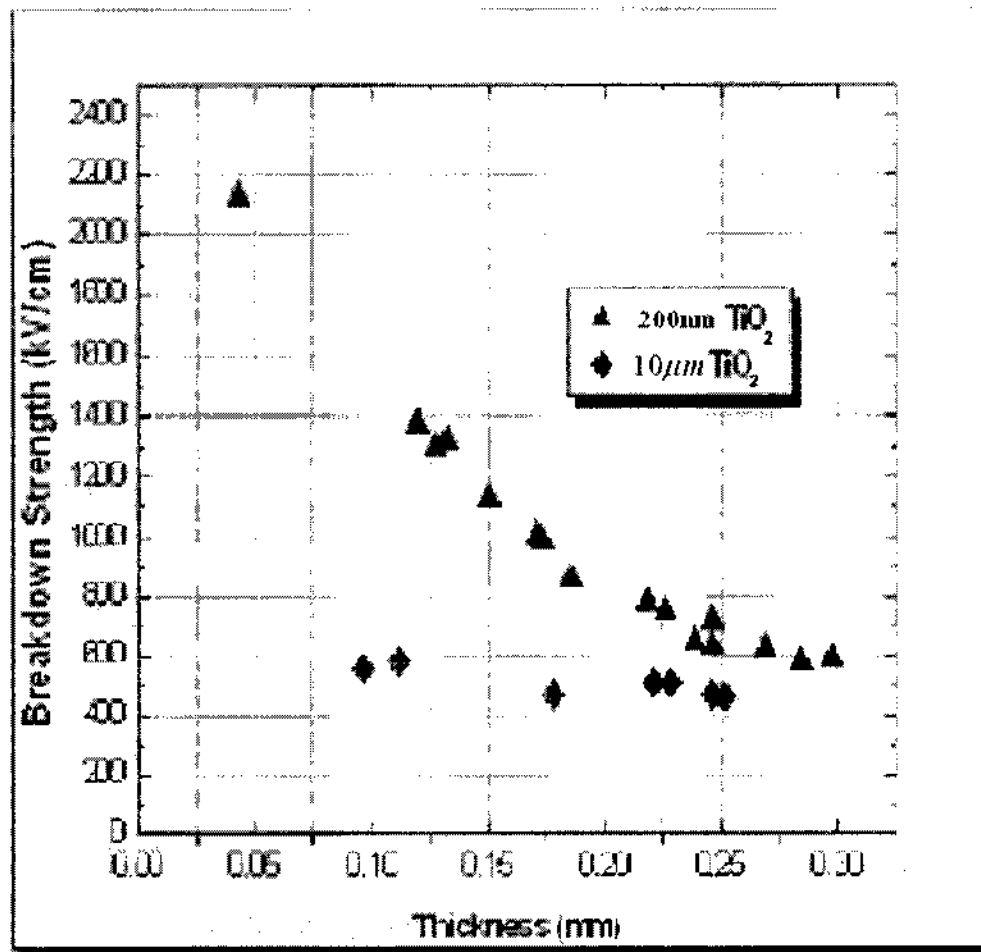
Figure 2-14. Breakdown strength versus TiO₂ thickness for nano-crystalline and course-grained materials [3].

A second and somewhat surprising observation with regards to high field studies on nano-crystalline TiO₂ has been the *lower breakdown fields under pulsed conditions* as compared to quasi-DC biasing [3]. In these experiments, the "quasi-DC" case consisted of slow ramped voltages (starting from an initial zero value), with increases until device breakdown. The pulsed testing, on the other hand, was performed with a burst of ten pulses per shot until failure. Although only six samples were tested, the results were still

able to show a lower breakdown strength under pulsed conditions, as given in Table 2-1

[3].

Table 2-1. Breakdown data under DC and Pulsed testing.

Sample number	Sintering Temp (°C)	Thickness (mils)	Breakdown voltage (kV)	Breakdown field (kV/cm)
1	800	6.5	DC: 10 Pulsed: 4.8	DC: 606 Pulsed: 291
2	800	6.0	DC: 14 Pulsed: N/A	DC: 919 Pulsed: N/A
3	800	6.0	DC: 7.5 Pulsed: N/A	DC: 492 Pulsed: N/A
4	850	7.0	DC: 18 Pulsed: 13.5	DC: 1012 Pulsed: 759
5	850	8.5	DC: 16 Pulsed: 17	DC: 741 Pulsed: 787
6	850	6.0	DC: 11.5 Pulsed: N/A	DC: 755 Pulsed: N/A

The energy delivered to the TiO_2 under pulsed conditions is substantially less than under the DC case. Hence, for such transient pulsing, issues related to possible heating and thermal charge generation can be expected to be relatively weak and cannot be the probable cause for breakdown. Almost universally, solids have been shown to sustain much higher applied voltages before eventual breakdown under pulsed conditions as compared to DC biasing [48]. The only reports of higher breakdown fields under DC conditions, to our knowledge, were observations made on Metal Semiconductor Field Effect Transistors (MESFETs) containing surface traps [49, 50].

2.8 Introduction of Non-Linear Transmission Line and Its Application to Pulsed Power Waveform Shaping

The generation of high-voltage electrical pulses with very fast rise-times is important for several pulsed power applications. These include high-intensity, ultra-fast lasers; particle accelerators for experimental nuclear physics; radar engineering; and pulsed technologies for purification of gaseous discharges, neutralization of wastes, and sterilization of food and water. The pulsed power systems are designed to deliver a quantity of energy at a specific voltage and current to a load over the duration of a pulse. In common pulsed power systems, energy is initially delivered from a prime power device, stored in an intermediate storage device, transferred to a pulse forming and voltage–current scaling device and then transferred to a load using multiple switches. Such high-voltage pulses are typically realized based on two main approaches: initially storing the energy in capacitors and then switching the current to a load through a closing switch; or by storing the energy in inductors and subsequently delivering to the load via opening switches. Ideally, the pulse-shaping device should also provide a relatively "square" pulse and be matched to the load such that the ratio of delivered pulse energy to stored energy approaches unity.

The problem of high-power switching has conventionally been approached with the help of switching devices such as spark gaps, thyratrons, non-linear ferrite lines, and plasma/electric explosive opening switches. However, the main focus and requirement for many emerging applications is the ultra-fast rise time that should be in the sub-nanosecond range [51]. In this regard, semiconductor opening switches (SOSs) have been reported for purposes of attaining fast rise times [52-54]. However, high-voltage solid

state switches suffer from several problems such as "lock-on," filamentation and device degradation [55]. Besides, the lifetime of these devices is relatively short and their high voltage capability is limited [56]. High-pressure hydrogen-filled [57] or oil filled [58] spark gaps are capable of switching very high voltages in less than 200 ps but are limited in their pulse repetition rate. Additionally, in high-power systems, the working life of spark gaps is severely limited by electrode erosion. Other methods such as optical and over-voltage triggering of liquid gaps have been explored for pulsed power applications. [59-61]. However, these systems require large energy input, have a low repetition rate and can easily change their response characteristics due to electrode contaminants and dissolved gases [62]. The triple-point issue [63] can also be an operational hurdle.

A way around the problem of ultra-fast, yet reliable, switching is to first generate a relatively slowly rising voltage pulse. It can then be fed to the load via a nonlinear system such as a magnetic switch or a non-linear electric device that alters its temporal profile. This reduces the rise-time demands placed on the primary switch so that reliable long lifetime devices such as thyratrons or thyristors can be used. To achieve pulses with rise-times of less than one nanosecond, the last component of the nonlinear system can be a transmission line with nonlinear characteristics. The nonlinearity may be due to changes in the capacitance or inductance distributed along the transmission line [64]. In the past, transmission lines containing ferrites with nonlinear magnetic materials have received some attention [65,66]. Although it has long been recognized that transmission lines containing nonlinear ferroelectric dielectrics could also be used as nonlinear components in high-voltage systems [56], little experimental work or theoretical analyses appears to have been published.

Pulse sharpening by shrinking the rise- and fall-times is also useful in applications other than pulsed power technology. For example, in high-speed sampling and timing systems, both pulse shaping and solitary wave propagation have been demonstrated using GaAs technology [67,68]. The importance of non-linear transmission lines to digital signals was first discussed by Landauer [69] and was later assessed in the context of ceramic dielectrics by Smith *et al.* [70]. With advances in ceramics technology, leading to increased breakdown voltage capability and strongly voltage dependent capacitances, it becomes more meaningful and germane to consider applying such materials as nonlinear transmission-line elements. In this context, **barium strontium titanate (BST)** is a promising candidate material with a field-dependent permittivity. There has been a strong interest in thin-film BST, as a high permittivity dielectric with breakdown fields above 0.6 MV/cm [5], for dynamic random access memory [71], and in radio-frequency or microwave [72,73] applications. Work has focused on reducing dielectric losses for microwave devices and in attaining increased tunability of the dielectric constant with bias [74]. Given the emerging importance of BST as high-voltage material with non-linear characteristics, the potential for its application to rapid rise-time and pulse shaping, and the dearth of reported studies in this field, we attempt to present a simulation analysis in this contribution. Details of the model developed, the numerical solution scheme and results obtained are provided and discussed in the following chapters.

CHAPTER III

MODELING AND SIMULATION DETAILS

3.1 Model of Microstructure of ZnO Varistor Ceramics

The non-linear current-voltage characteristic of the ZnO varistor is determined by its microstructure and the characteristics of it grains and grain boundaries. To successfully model the microstructure of a ZnO varistor, the following features should be considered and included: (a) non-uniformity and relative disorder of grain sizes and shapes and (b) non-uniformity of electrical characteristics of the various grain boundaries. These aspects are discussed in greater detail in the following sections.
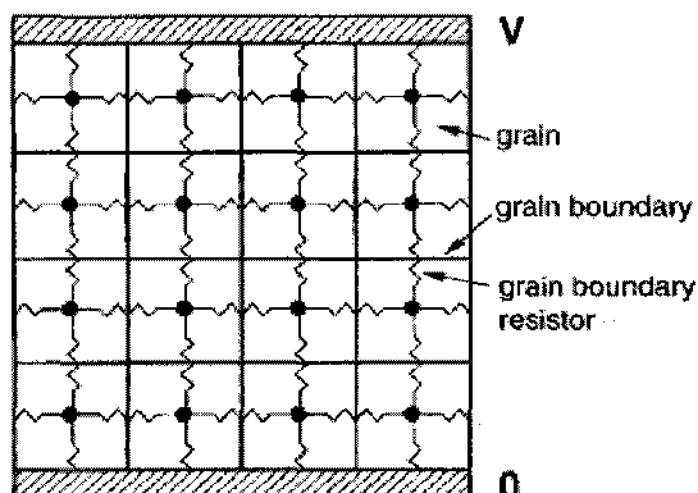
Figure 3-1. "Brick" model proposed by Wen and Clarke, used to compute the current flow and the overall varistor characteristics. The array of grain boundary resistors, assumed to be nonlinear with values selected at random, is the topological dual of the microstructure of square grains. After [75].

3.1.1 Nonuniformity and relative disorder of grain sizes and shapes:

ZnO varistors are composed of a large number of grains with different sizes and shapes, as shown in Figure 2-4. With current technology, it is impossible in practice to

fabricate ZnO varistors with uniform grain size and shape. Thus, the "brick" network model proposed by Wen and Clarke [75], shown in Figure 3-1, which has a regular geometry and inherent symmetry, is not ideal to model the non-uniformity and relative disorder of grain sizes and shapes.

This issue was first addressed by Bartkowiak and Mahan [44] who introduced a Voronoi network model, as shown in Figure 3-2. This closely modeled the non-
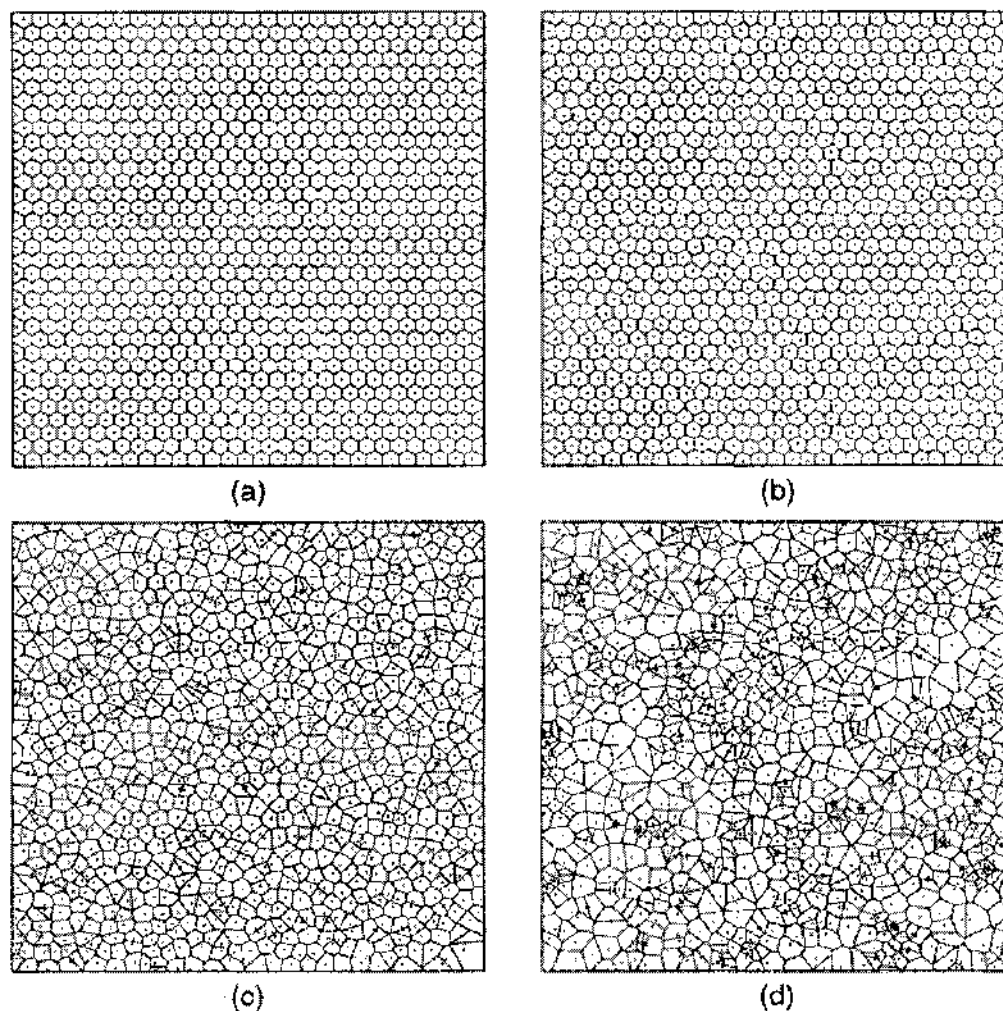
Figure 3-2. Voronoi cell structure for different values of disorder parameter d (see text). (a) $d = 0$ (regular hexagonal structure); (b) $d = 0.18$ (deformed hexagonal structure); (c) $d = 0.6$; (d) $d = 8.0$, for which the structure can be regarded as generated form a fully random distribution of seed points. After [44].

uniformity and disorder very well and is now well accepted and widely used by researchers. Consequently, this model is also used in this dissertation research.

To generate this Voronoi network, one starts with an orderly distribution of seed points (i.e., the x- and y- coordinates) in the two-dimensional simulation region. The number of seed points is first controlled to meet the demand of the specified average distance "s" between adjacent seeds. This ensures that the density of seed points within the chosen simulation region matches the desired value. Then the position of these seeds is allowed to deviate by a displacement vector determined by two parameters: (i) the disorder parameter d (d>0) and (ii) an angle θ ($0 \le \theta \le 2\pi$). The radius and angle of the displacement vector are uniformly distributed within the intervals [0, $d \times s$] and [0,2π], respectively. By varying this displacement vector, the internal distance between neighboring seeds (and hence, the cells within the Voronoi network) can be made to change from a very ordered value and structure to an extremely random and disordered configuration. Thus, the cellular geometry effectively changes from that of Fig. 3-2(a) to the picture of Fig. 3-2(d). The Voronoi network itself, and the cells within the two-dimensional simulation region, are obtained by drawing perpendicular bisectors of the lines joining adjacent seed points. The intersections of the perpendicular bisectors then naturally define self-contained polygons. These polygons are taken to the internal, irregularly shaped grains. When $d \ge 5$, the 2D Voronoi network is very similar to the planar microstructure of ZnO varistor ceramics [12]. For very small values of d (e.g., d=0), a completely ordered "honey-comb" pattern results. Physically, one can represent a 2D growth process as starting simultaneously at all nucleation seed points and proceeding in the plane at a uniform rate. This growth process naturally terminates whenever two

approaching growth fronts reach each other. Therefore, the geometry and topology of Voronoi networks closely resemble those found in grain growth from random nucleation sites. In this way Voronoi networks provide a natural model for the study of transport through disordered structures such as polycrystalline materials. Random Voronoi lattices are topologically disordered, i.e., the coordination number is not constant; rather, it locally deviates from its average value, which in 2D is 6 [76].

In our simulation, it is assumed that each polygonal cell represents a ZnO grain and each edge l_{ij} shared by neighboring cells i and j corresponds to the grain boundary between these two grains. The thickness (along the perpendicular, third direction of the z-axis) of the ceramic is assumed fixed and denoted as H.

3.1.2 Nonuniformity of Electrical Characteristics of Grain Boundaries

The high variability exists in barrier voltages and nonlinearity coefficients in different grain boundaries. The barrier voltages can roughly be assumed to have normal distributions arising from the "Law of Large Numbers" of probability. Not all of the grain boundaries are electrically active, and the grain boundaries can simply be classified into "good", "bad", and "ohmic" ones according to their individual electrical characteristics. These few good grain boundaries are responsible for the non-linear varistor effect, the energy absorption, and control the leakage current of ZnO varistor at low values of applied voltage [13].

In ZnO varistors, the dominant resistance arises from the grain boundaries, while each grain has a significantly lower resistance by comparison. Hence, in this dissertation each grain was assumed to be a conductor, and only the current-voltage characteristic of

each grain boundary was considered. In particular, two different sets of *J-V* characteristics (after [11,12]) were used to model each grain boundary.

The first set of *J-V*, stated in Equation (2-2)-(2-4), was proposed by Barkowiak and Mahan [11]. For the reader's convenience, we list them again. For an "ohmic" grain boundary, the *J-V* is as [11]:

$$J(V) = \frac{V}{R_o}, \tag{3-1}$$

where $R_o = 2 \times 10^5 \ \Omega \cdot cm^2$, is the resistance of a unit area of the boundary. For a "good" grain boundary [11], the characteristic is taken as:

$$J(V) = \begin{cases} \dfrac{V}{R_g}\left[1 + \dfrac{V^{50}}{V_B^{50}}\right] & for \quad V \le V0_g \\[3mm] \dfrac{V}{R_g}\left[1 + \dfrac{V0_x^{50}}{V_B^{50}}\right]^{7/2}\left[1 + \dfrac{V0_g^{70}}{V_B^{50}V^{20}}\right]^{-2.5} & for \quad V > V0_g \end{cases} \tag{3-2}$$

where $R_g = 10^9 \ \Omega \cdot cm^2$, $V0_g = 3.467 \ V$, $V_B = 3 \ V$. Finally, for "bad" grain boundaries [11], the *J-V* relation is taken to be:

$$J(V) = \begin{cases} \dfrac{V}{R_b}\left[1 + \dfrac{V^{50}}{V_B^{50}}\right]^{1/5} & for \quad V \le V0_b \\[3mm] \dfrac{V}{R_b}\left[1 + \dfrac{V0_b^{50}}{V_B^{50}}\right]^{11/5}\left[1 + \dfrac{V0_b^{55}}{V_B^{50}V^5}\right]^{-2} & for \quad V > V0_b \end{cases} \tag{3-3}$$

where $R_b = 10^7 \ \Omega \cdot cm^2$, $V0_b = 3.622 \ V$, and $V_B = 3 \ V$.

The second set of *J-V* characteristics were proposed by Chen and He [12], and it is a universal equation for all grain boundaries no matter how nonlinear its coefficient. Their *J-V* expression is:

$$J_{ij}(U_{ij}) = \begin{cases} \dfrac{A_1}{\rho_{gb}}\exp\left[-\dfrac{E_g-\beta\sqrt{|U_{ij}|}}{K_bT}\right] + A_2\left[\dfrac{|U_{ij}|}{V_B}\right]^{\alpha} ; & |U_{ij}| \le V_U \\[2em] \dfrac{A_1}{\rho_{gb}}\exp\left[-\dfrac{E_g-\beta\sqrt{V_U}}{K_bT}\right] + A_2\left[\dfrac{V_U}{V_B}\right]^{\alpha} + \dfrac{[|U_{ij}|-V_U]}{d_{ij}\rho_g}, & |U_{ij}| > V_U \end{cases}$$
(3-4)

where J_{ij} denotes the current density flowing through the grain boundary between grains i and j in A/cm^2, and $U_{ij} = (U_i - U_j)$, with U_i and U_j being the voltages across grains i and j, and T the grain boundary temperature in Kelvin. Also in (3-1), V_B is the barrier voltage taken to be a non-uniform, random variable for each grain boundary chosen from a normal distribution function $p(V_B)$. This distribution function is given by:

$$p(V_B) = \frac{1}{\sqrt{2\pi}\times 0.2}\exp\left[\frac{(V_B-3.2)^2}{2\times 0.2^2}\right], \quad V_B > 0.$$
(3-5a)

The parameter α denotes a nonlinear coefficient and also follows a normal distribution $p(\alpha)$:

$$p(\alpha) = \frac{1}{\sqrt{2\pi}\times 50}\exp\left[\frac{(\alpha-7)^2}{2\times 50^2}\right], \quad \alpha \ge 1.$$
(3-5b)

Finally, V_U is the critical upturn voltage in the high electrical field region, $V_U = V_B(J_U/A_2)^{1/\alpha}$, where J_U is the critical upturn current in high electrical field region. Here J_U was chosen to be 10^3 A/cm^2 as reported elsewhere [12]. The other parameters in (3-1) are listed in Table 3-1. Based on these values, the J-V curve for different α values with $V_B = 3.2$ V and $d_{ij} = 15\times10^{-4}$ cm, can be obtained and is shown in Figure 3-3.

The above formulation allows for stochastic variations via the barrier voltage V_B. For example, V_B has been reported to roughly follow a normal (Gaussian) probability distribution [13]. Here we adopt a mean barrier voltage of 3.2 V and report on simulations with different variances.

Table 3-1. The various parameters of Equation (3-4).

Symbol	Meaning	Unit	Value
A_1	constant	$A \cdot \Omega / cm$	2.5×10^{16}
A_2	constant	$A \cdot \Omega / cm^2$	0.01
ρ_{gb}	resistivity of grain boundary	$\Omega \cdot cm$	10^{12}
ρ_g	resistivity of grain	$\Omega \cdot cm$	1
E_g	barrier height	eV	0.8
β	constant	$eV^{1/2}$	2.83×10^{-2}
K_b	Boltzmann's constant	eV/K	8.625×10^{-5}
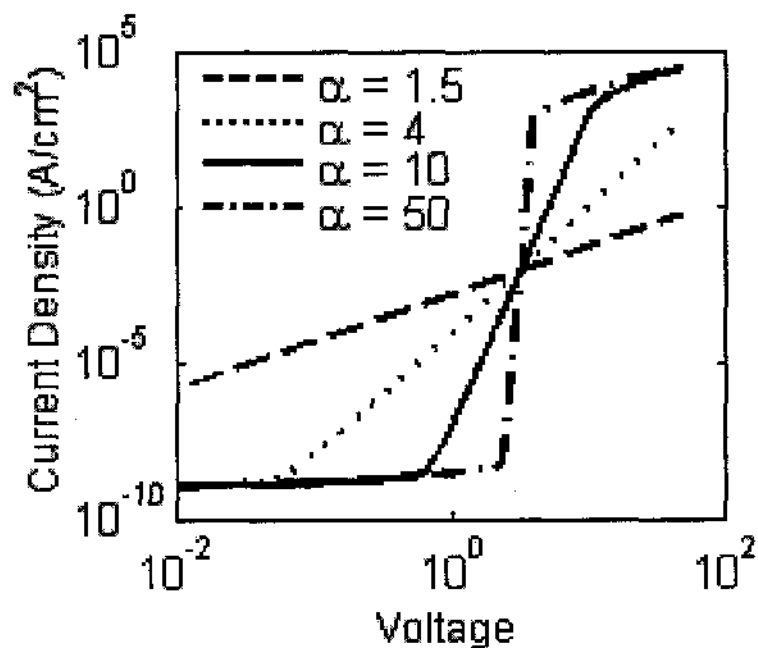
Figure 3-3. The J-V characteristics of a single GB for different α values with mean $V_B = 3.2$ V, $d_{ij} = 15 \times 10^{-4} cm$ and other parameters as listed in Table 3-1.

The next step is generating two groups of random numbers, and the total number of these random numbers in each group is equal to the total number of grain boundaries in the Voronoi network. One group of numbers is the barrier voltage V_B of every grain

boundary, which follows the distribution given by Equation (3-5a); another group is the nonlinear coefficient α of every grain boundary, which follows Equation (3-5b). Then each grain boundary is assigned a V_B number and an α number, and with these two numbers, the current-voltage characteristics of each grain boundary is specifically determined.

3.2 Model for the Solving Nonlinear Resistor Network and Calculations of Joule Heat in ZnO Varistors

After generating the Voronoi network and randomly assigning each grain boundary characteristic, the distribution of voltage and current within this microstructure is calculated based on the nodal analysis of circuit theory. The circuit solver uses the topology of the Voronoi network. A nonlinear resistor network corresponding to the dual of the network of Voronoi polygons is shown in Figure 3-4.
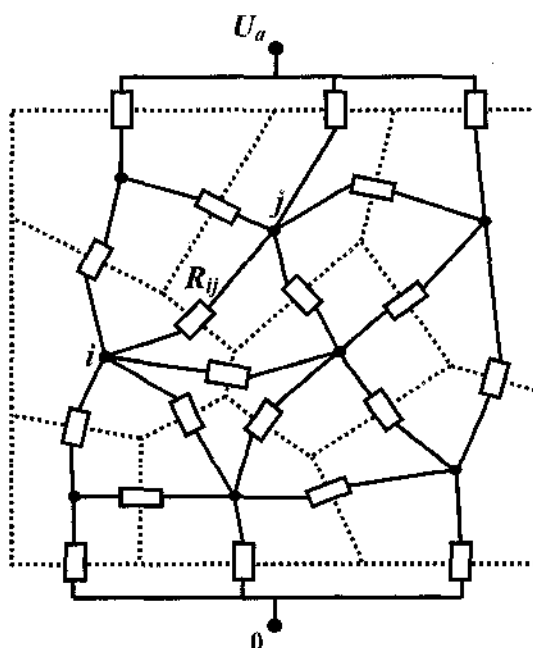
Figure 3-4. Conceptual circuit for the microscopic simulation of a ZnO varistor.

The external, electrical voltage is applied between the top and bottom edges of the Voronoi network. The nonlinear resistor R_{ij} by the real lines as shown in Figure 3-4 is used to describe the electrical characteristic of the grain boundary between grains i and j. The current flowing through the resistor R_{ij} is assumed to be the product of the area $\left(l_{ij} \times H\right)$ of the grain boundary and the current density J_{ij} flowing through the grain boundary between grains i and j, defined by Equation (3-4) or Equations (3-1)-(3-3). The nodal voltage equations are derived from the branched circuit schematic shown in Figure 3-4. By applying the Kirchhoff current law at the ith node of an N-node circuit we get:

$$I_i(V) = \sum_{\substack{j=1 \\ j \neq i}}^{N} l_{ij} H\left(sign\left(V_i - V_j\right) J_{ij}\left(V_i - V_j\right)\right) = 0 \quad , \tag{3-6}$$

where V is the node voltage vector $\left(V_1, V_2, \cdots, V_N\right)$, and H is the thickness of the sample; l_{ij} is the length of the common grain boundary between grains i and j. If the grain j is not a neighbor of the grain i, then $l_{ij}=0$. This large-scale, non-linear set of coupled node voltage equations can be solved at each time step by the Newton iterative method. The solution then yields currents flowing through the GBs as calculated by (3-1). The Joule heat generated at each GB is then given as:

$$P_{ij} = l_{ij} H V_{ij} J_{ij}, \tag{3-7}$$

where V_{ij} and J_{ij} denote the voltage difference and current density between adjacent granular regions, and l_{ij} is the length of their common grain boundary, and H is the thickness of the sample. Here, H is assumed to equal the average size of the grains.

3.3 Method of Calculation of Heat Transfer and Thermal Stress in ZnO Varistors

Bartkowiak and Mahan [38] calculated the temperature variations in the granular microstructure, assuming the severe case of heating only the grain boundaries with a power input $2 \times 10^7 W / cm^3$. The results showed that differences between the temperature at the grain boundary and the grain interior quickly reached approximately 35°C (after about 1μs) and did not increase any further during the heating. This means that the heat transfer on the scale of the grain size is too fast to permit a temperature difference that can cause cracking, so in our model, only inter grains heat transfer and thermal stress are considered and calculated. The physics and mechanical tearing associated with possible cracking is ignored.
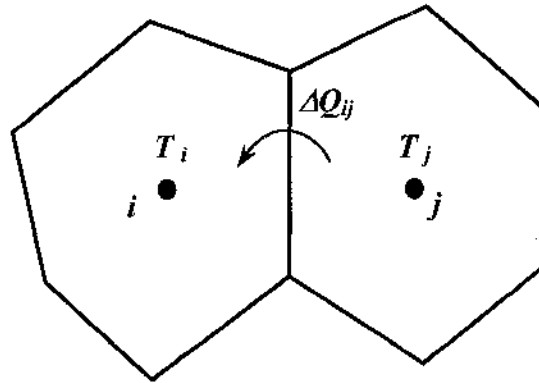
Figure 3-5. Schematic for heat transfer at grain i between adjacent granular regions.

It is assumed that the average temperatures of cells i and j are T_i and T_j and that their initial values are at the ambient temperature (300 K in this dissertation). A schematic of the geometry involved in this heat-flow problem is shown in Figure 3-5. The heat (dQ_i) transferred into cell i during time duration dt is approximately determined by:

$$dQ_i = \sum_j \Delta Q_{ij} = \sum_j \left(T_i - T_j\right)\frac{l_{ij}H}{d_{ij}}k_T dt \quad (J) \quad , \tag{3-8}$$

where l_{ij} is the length of the common side between adjacent grains, d_{ij} is the distance between the centers of the two adjacent grains, T_j the average temperature of the adjacent grain j, and k_T the thermal conductivity of ZnO varistors. Previous studies [12] have used $k_T = 5.7 \times 10^{-2} W \cdot cm^{-1} \cdot K^{-1}$ as the thermal conductivity value. However, since the thermal conductivity depends strongly on temperature [77, 78], it is not a fixed constant. Several groups, including Touloukian et al. [79], list experimental data for ZnO. Using these data, the following fitting equation for the temperature dependent thermal conductivity $k(T)$ was obtained and used here:

$$k_T(T) = -5.2705 \times 10^{-10} T^3 + 1.7283 \times 10^{-6} T^2$$
$$-1.8926 \times 10^{-3} T + 0.72696 \quad [W/(cm \cdot K)] \tag{3-9}$$
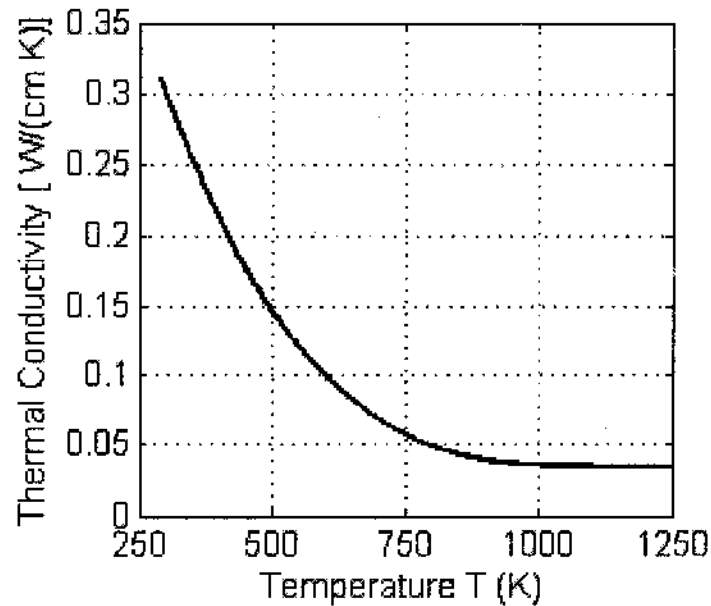
Figure 3-6. Temperature dependent thermal conductivity of ZnO varistor.

This relationship is shown in Figure 3-6. The reduced conductivity at higher temperatures reduces the heat removal and, hence, works to heighten the temperature at local hot spots. This is, in effect, a positive feedback mechanism since the higher local temperature then lowers the thermal conductivity further. This can sharply enhance the temperatures of local "hot-spots".

The temperature rise dT_i of grain i during dt is then given by the following equation:

$$dT_i = \frac{P_i dt + dQ_i}{S_i H \rho C_p} \quad (K),$$

(3-10)

where S_i denotes the area of the grain i, the ZnO varistor film thickness H is the average grain size, $\rho = 5.6$ g/cm^3 is the mass density of ZnO, $P_i = 0.5 P_{ij}$ (P_{ij} is defined in Equation (3-7)), and C_p is the thermal capacity of ZnO ceramics taken to be [12]:

$$C_p = 0.498 \left[1 + 0.000828 (T_i - 20) \right] J / (g \cdot K) .$$

(3-11)

If the temperatures between two adjacent grains (say i and j) are unequal, then a thermal stress f_{ij} develops between them [80]. The expression for f_{ij} is given by:

$$f_{ij} = \frac{E \lambda (T_i - T_j)}{1 - \mu} \quad (MPa),$$

(3-12)

where E is the Young's modulus taken to be 6.9×10^4 MPa, μ is the Poisson ratio equal to 0.3, and λ is the linear expansion coefficient of ZnO varistor ceramics of about $4.86 \times 10^{-6} K^{-1}$. The above values were taken from Chen $et\ al.$ [12].

With large current flowing through ZnO varistors, the localized temperature at grain boundaries can dramatically increase and even exceed the $820°C$ melting point of Bi_2O_3 in the grain boundaries [12]. Upon melting, as the barrier in the grain boundary vanishes, the localized grain boundary is assumed to be permanently destroyed. The conductivity

can then be expected to switch over to an Ohmic, highly resistive characteristic for two reasons. First, liquids are known to present large impedance to electrical conduction due to the solution of charges and higher atomic disorder that leads to lower mobility. Second, the solid-liquid interfaces at locally melted zones and resulting discontinuities in band structure would further impede current flow into the liquid. Thus, large localized increases in resistance can dynamically be expected within a ZnO sample, in response to large current surges. Also, the large current driven heat dissipation in ZnO varistors containing a heterogeneous distribution of grain boundaries is likely to generate thermal stresses that can lead to localized cracking. This would also produce localized insulator-type behavior and effectively increase the local resistance. In order to include these melting and/or cracking aspects into our model, a dynamic ZnO conduction was used. In this research, the J-V characteristics of (1) were switched over to the following curve for a melted and/or stressed GB:

$$J = V/(2 \times 10^7) \quad \left(A/cm^2 \right) \; . \tag{3-13}$$

Though other J-V representations are possible, the general qualitative features and trends are expected to remain well represented by this current approach.

In addition, simulations with pores are also carried out. To model pores, 5% grains were randomly picked up and assumed to be vacuum, i.e. no mass, no current conduction, no thermal conduction, and no thermal stresses at its boundaries.

In order to study the failure of grain boundary barrier dominated ZnO samples, simulations were carried out with a bias chosen to make the current density equal to $100 A/cm^2$. Two different disorder parameters d=1 and d=5 were used in a Voronoi network with 492 grains. For each disorder parameter, the average grain size was varied

from 1 μm to 30 μm. Voltages at the center of each grain within the Voronoi network representation were computed. Thus, node analysis based on the Kirchhoff current law (KCL) of circuit analysis was used to self-consistently solve for the voltages at each node of a given Voronoi network. Dirichlet boundary conditions at the top and bottom (electrode) locations and Neumann "zero current" transverse requirement at the left and right boundaries were applied. This amounted to a simultaneous solution of a system of non-linear, coupled equations, as already stated in the context of Equation (3-6). The solving of this non-linear system led to dynamic evaluation of the distributed currents and localized power generation within the sample. Local temperatures at each grain were tracked until the Bi_2O_3 melting point of 820 °C was reached. As reported in the literature [12], when temperatures within the ZnO ceramic rise to values above 820 °C, the Bi_2O_3 in the GBs melts, and the varistor has a localized permanent breakdown. For grains reaching this melting threshold, the J-V characteristics were switched to those of Equation (3-13) in a dynamic fashion. Thus, this procedure allowed the sequential analysis of successive localized failures and phase-transitions.

Our time-dependent simulations were continued in time without any dynamic J-V updates as long as the grains remained below 820°C and the 137.9 MPa critical stress threshold [39] was not reached. If two or more segments exceeded the set thresholds, the simulation was terminated. In this model, only resistive currents are considered. Thus, any time dependence of currents is related only to Joule heating. Capacitive and inductive effects were not considered. However, these could easily be included by adding terms to the governing current Equation (3-6) to obtain a modified matrix. The implicit discretization scheme could then be applied for numerical solution. Since the

thermal processes are typically much slower, and the present focus is on potential electro-thermal failures, the transient displacement currents (due to the capacitance) or inductive voltage effects were ignored.

In order to investigate the effects of grain size and its internal random structure, the following procedure was adopted.

(i) The Voronoi network was first generated, with a fixed disorder parameter "d". This value was taken to lie in the range between 0.2~6.0.

(ii) The barrier voltages V_B for each of the grain boundaries were chosen from a set of random numbers that follow the normal distribution of defined by (3-2a).

(iii) The nonlinear coefficients α were similarly selected from another set of random numbers according to the normal distribution of (3-2b).

(iv) For this chosen network and parameters, the average grain size was selected from within the 1 μm - 30 μm range. It may be mentioned that the sample thickness was taken to equal the average grain size, so the thickness did change with the average grain size. For a given selected average grain size, the actual granular blocks varied about this chosen mean, via the Voronoi network construction.

(v) For each value of average grain size and Voronoi network, the bias voltage corresponding to an internal ZnO current density of 100 A/cm^2 was calculated. For this voltage, simulations runs were performed until two or more segments exceeded the set thresholds. These limits, as discussed earlier, were for temperatures at the internal grains to remain below 820°C and a critical stress of 137.9 MPa to be reached.

3.4   Model of TiO₂ Breakdown Under Pulsed Conditions

In order to analyze and study the breakdown behavior of TiO_2, here we propose a continuum model that includes the presence of internal traps, especially at the grain boundaries. TiO_2 has a similar granular structure as ZnO. Application of an external electric field works to release electrons from the traps. If sufficiently high electric field magnitudes exist within the TiO_2, then the emitted electrons can undergo impact ionization and contribute to current enhancements. However, if the external voltages were driven very slowly, then most of the trapped charge would gradually be emitted and drift out of the device long before the creation of high electric fields. The slow ramped, quasi-DC conditions would then preclude strong charge accumulation and multiplication through internal impact ionization. We hypothesize that the lower breakdown voltages observed in TiO_2 under pulsed conditions, is *a direct rise-time effect, coupled with cumulative detrapping*. Under conditions of multiple short-duration pulsed bursts, trapped electrons could periodically be released within the device during times of high applied voltages. However, these electrons might not have the requisite time, nor be subjected to the continued high external fields (due to finite pulse duration) necessary to drive them out of the semiconductor. Hence, cumulative build-up of mobile charge from preceding pulses could likely occur. Breakdown during a subsequent pulse can then result. This is brought out more clearly through our transport model and simulation results.

A one-dimensional (1D), time-dependent simulation based on the continuum, drift-diffusion model of semiconductor transport was used, as shown in Figure 3-7. A 25 µm TiO_2 ceramic divided into 1000 cells was used with a time step of 10^{-10} second. Six

grain-boundaries were randomly placed within the simulation region. A copper electrode was assumed and the electric field obtained by solving Poisson's equation under Dirichlet boundary conditions. Holes were neglected, since observations indicate that electrons dominate the electrical behavior [81] of nano-crystalline TiO_2. The basic parameters of this model are listed in Table 3-2 and were taken from the literature [82-86]. A trap level located 2.4 eV from the valence band edge with a density of 10^{17} cm^{-3} was assumed. The electron capture cross-section was taken to be 10^{-13} cm^2.
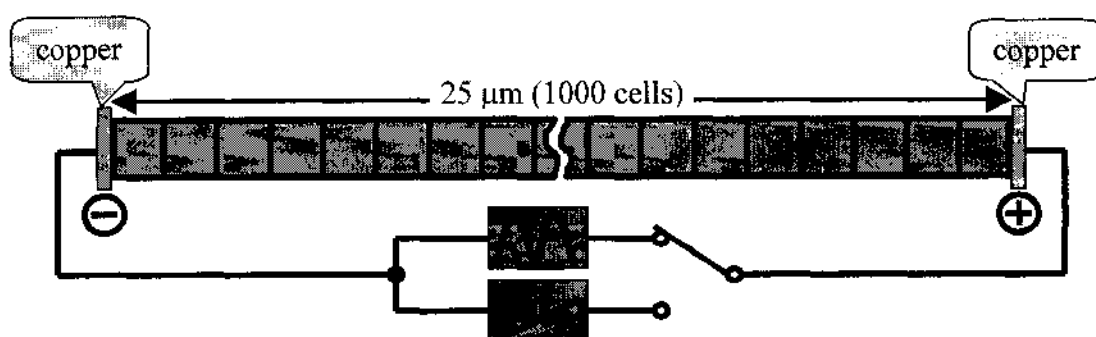
Figure 3-7. Illustration of one-dimensional TiO_2 ceramic model.

Table 3-2. Parameters used in the simulation model.

Dielectric constant	114 [3]
Trap density	10^{23}/m^3 [48]
Electron effective mass	45m$_0$ [3]
Electron mobility	0.33 cm^2/V sec [49]
TiO_2 Electron affinity	3.9 eV [50]
Copper work function	4.7 eV [81]
Free electron density	10^{20}/m^3
Temperature	300 K
Diffusivity	8.527 x 10^{-7} m^2 s^{-1}

The following standard semiconductor transport equations to include the drift and diffusion currents, along with the generation recombination terms, were used [87, 88]:

$$
\begin{cases}
\dfrac{\partial n}{\partial t} = \dfrac{1}{q} divJ_n + G_n - R_n \\[2mm]
J_n = qn\mu_n E_n + qD_n \nabla n \\[2mm]
\dfrac{dE}{dx} = \dfrac{q}{\varepsilon}\left(p - n - N_t^-\right)
\end{cases}
\qquad , \qquad (3\text{-}14)
$$

where n and p are the electron and positive ion densities; J represents current densities; G and R the carrier generation and recombination rates, respectively; μ carrier mobility; D the diffusivity; E the electric field; and N_t^- the trapped electron concentration. Our model included field emission current J taken to be [87]:

$$
\begin{aligned}
J &= \frac{4\pi q m_n^* k^2}{h^3} T^2 \exp\left(-\frac{q\phi_{B0}}{kT}\right)\exp\left(\frac{q\Delta\phi}{kT}\right) \\[2mm]
&= 0.181158 \times \exp\left(\frac{q}{kT}\sqrt{\frac{qE}{4\pi\varepsilon_s}}\right)(A/m^2)
\end{aligned}
\qquad , \qquad (3\text{-}15)
$$

and field-dependent drift velocity $v_e(E)$ given by [89]:

$$
v_e = \frac{3.3\times10^{-5}E}{\left[1+\left(3.3\times10^{-5}E/89\right)^{1.7}\right]^{1/1.7}}(m/\sec) \cdot \qquad (3\text{-}16)
$$

The impact ionization coefficient α for electrons was taken to be:

$$
\alpha = 9.1\times10^{10}\exp\left(-\frac{7.7\times10^8}{E}\right) \cdot \qquad (3\text{-}17)
$$

Finally, the following expressions were used for electron emission and capture rates from traps:

$$
R_{capture} = 9\times10^{-18}\cdot\left(10^{23} - N_t^-\right)\cdot n \qquad , \qquad (3\text{-}18)
$$

$$
R_{emit} = \frac{N_t^-\cdot\exp\left(1.3\times10^{-4}\sqrt{E}\right)}{4.751848} \cdot \qquad (3\text{-}19)
$$

3.5 Non-Linear Transmission Line Model

3.5.1 Representation of the Granular BST Material

Another aspect of the present research focused on the study of using non-linear transmission lines with voltage-dependent parameters (e.g., the capacitance) for sharpening the rise-time of pulses for high-voltage, pulsed-power applications. In this context, barium strontium titanate (BST) was chosen as the relevant material for the study. The choice of BST as the dielectric media was based on its high permittivity and strong voltage-dependent capacitance. The latter arises from the internal granular structure associated with internal grain boundaries. This voltage dependent capacitance is an important factor for this non-linear transmission line application.
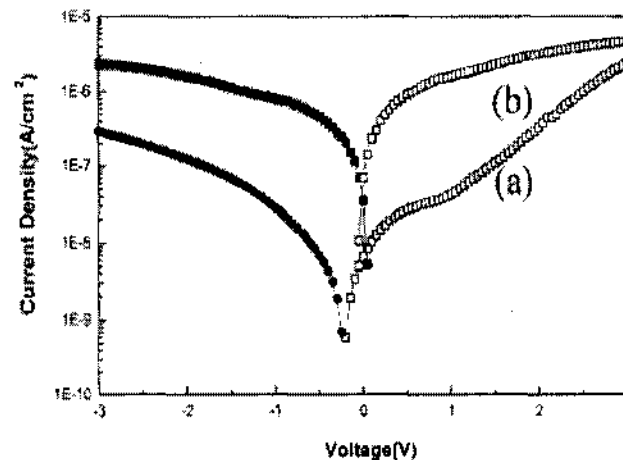
Figure 3-8. Current–voltage (J-V) curves of (Ba,Sr)TiO$_3$ thin films deposited at the temperature of (a) 520 and (b) 440°C for (□) positive bias and (■) negative bias. After [91].

Like ZnO varistor, BST also has a granular micro-structure that can be modeled in terms of a random, two-dimensional, Voronoi network [76,90]. The only difference between the BST and the ZnO varistor is the current-voltage (J-V) characteristic of grain boundaries. In the present simulation, the following J-V characteristics (after Lee and

Rhee [91], curve (a) shown in the Figure 3-8) were used to model each BST grain boundary:

$$J(V) = 10^{0.7453|V|-7.8935} \ (\text{A/cm}^2) \ , \tag{3-20}$$

where V is the applied voltage across a grain boundary.

Similarly, by solving Equation (3-6) the node voltage vector $(V_1, V_2, \cdots, V_N)$ could be made available, and then yield the currents passing through the grain boundaries as calculated by Equation (3-20). Voltages and average electric fields across the grain boundaries could also then be computed.

3.5.2 Voltage Dependent Capacitance of Grain Boundary

In order to compute the grain boundary capacitances of TiO_2 ceramic, the voltage dependence and its associated nonlinearity needs to be determined first. This is discussed here, based on the Park and Payen [92] model for the microstructure at each grain boundary. The energy band of the model grain boundary layer (GBL) capacitor is shown in Figure 3-9. It assumes a central intrinsic grain boundary region and unintentionally doped n-type sections at the two ends. The potential barrier V_B for the central grain boundary junction in this model is similar to that of an Schottky diode. On application of a bias voltage, the barrier decreases to $(V_B - V_1)$ in the forward case and increases to $(V_B + V_2)$ in the reverse case. Let C_c^F and C_c^R represent the forward and reverse bias capacitances per unit area on either side of the central insulating barrier of width 2δ. The total series capacitance C_s per unit area is given by the capacitance of the insulating layer C_i and the series connected forward C_c^F and reverse C_c^R biased compensation layers, as:

$$\frac{1}{C_s} = \frac{1}{C_i} + \frac{1}{C_c^F} + \frac{1}{C_c^R} \quad . \tag{3-21}$$

This can be expanded to a voltage dependent form as:

$$\frac{1}{C_s} = \frac{2\delta}{\varepsilon_0 K_i} + \sqrt{\frac{2(V_B - V_1)}{qN_D\varepsilon_0 K_c}} + \sqrt{\frac{2(V_B + V_2)}{qN_D\varepsilon_0 K_c}} \quad , \tag{3-22}$$

where ε_0 is the permittivity of the vacuum; K_i and K_c are the relative dielectric constants of the insulating and compensation layers, respectively; q the electronic charge; and N_D the concentration of uncompensated ionized donors. Since the decrease of the forward-biased barrier V_1 is negligibly small [93], the second term in Equation (3-22) can be regarded as a constant, and V_2 is approximated to the applied voltage V. Then, the following equation results:

$$\frac{1}{C_s} = \frac{2\delta}{\varepsilon_0 K_i} + \sqrt{\frac{2V_B}{qN_D\varepsilon_0 K_c}} + \sqrt{\frac{2(V_B + V)}{qN_D\varepsilon_0 K_c}} \quad , \tag{3-23}$$

where $V = V_1 + V_2 \approx V_2$.
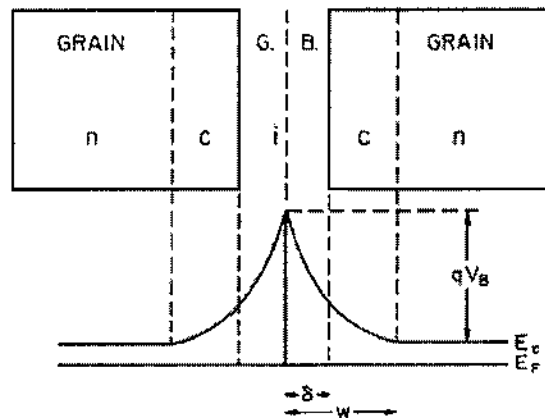
Figure 3-9. Energy band diagram for equivalent grain-boundary barrier model. After [92].

3.5.3 Voltage Dependent Permittivity and Capacitance

In order to compute the capacitance and take account of its nonlinearity, the voltage (or electric field) dependence of the permittivity must be considered. Chen et al. [4] measured the field dependent relative dielectric constant of BST $(Ba_{0.6}Sr_{0.4}T_iO_3)$ and obtained experimental data. The field dependent dielectric constant was shown to be given in terms of the following fitted polynomial:

$$\varepsilon_r = \begin{cases} 4242.2 - 66.9E^{2.31}, & E < 6.0271 \quad kV/cm \\ 1, & E > 6.0271 \quad kV/cm \end{cases} , \tag{3-24}$$

where K_r is the dielectric constant and E the electric field in kV/cm.

Using the above non-linearity, the voltage-dependent grain boundary capacitances, as given by equation (3-23), can be evaluated. This allows for the calculation of the overall voltage dependent capacitance of the entire granular BST sample based on the following procedures: (1) construct the Voronoi representation of the overall sample with the various grain boundaries given the mean grain boundary size and its variance; (2) obtain the voltages across each grain boundary by solving the system of N-coupled simultaneous equations derived from Kirchhoff's current law for the circuit; (3) use the voltage at each grain boundary to calculate the permittivity and capacitance; (4) use the grain boundary voltages and capacitance, the total charge stored across each grain boundary as well as the total charge Q_a at the anode plate is made available through the computation. At last the total capacitance of the BST sample will be:

$$C = \frac{Q_a}{V_a} \quad (nF/m) . \tag{3-25}$$

The relationships of capacitance per unit length versus voltage calculated from this model are listed in Table 3-3 and also shown in Figure 3-10.

Table 3-3. Voltage dependent capacitance per unit length.

Average grain size	Curve-fitting Equation	Sample dimension
20 µm	Equation (3-26)	
25 µm	Equation (3-27)	300µm X 300µm X 20µm
30 µm	Equation (3-28)	

$$C(V) = -0.02843V + 8.294 \text{ (nC/m)}, \tag{3-26}$$

$$C(V) = 10^{-6}\left(-1.875V^3 + 579.2V^2 - 87603V\right) + 11.089 \text{ (nC/m)}, \tag{3-27}$$

$$C(V) = 10^{-7}\left(0.5726V^4 - 213.6V^3 + 29235V^2\right) - 0.2142V + 14.607 \text{ (nC/m)}. \tag{3-28}$$
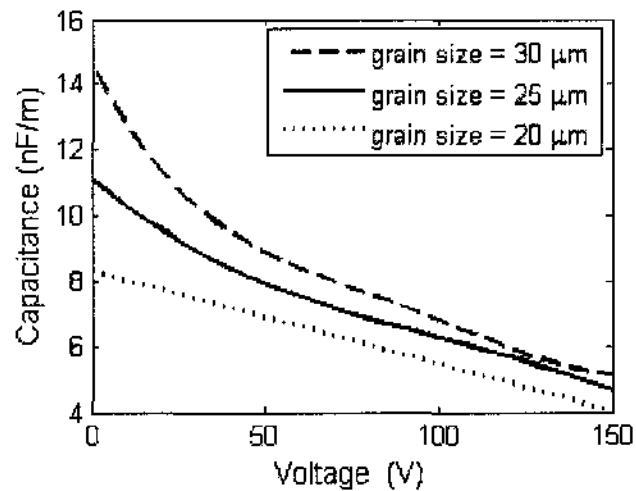
Figure 3-10. Voltage dependent capacitance from the BST model.

As might be expected, Figure 3-10 shows that the capacitance decreases monotonically with applied voltage. Furthermore, the capacitance magnitude increases with increasing grain size. This can qualitatively be understood in terms of the impedance to current flow associated with the grain boundaries. A smaller GB size translates into a higher number of grains for a given sample. Thus, an increased number of GB barriers would typically be encountered during current flow in such samples, leading to lower

overall current. Hence, the charge present in the system would progressively decrease with smaller grain sizes.

3.5.4 Model Of Transmission Line With Nonlinear Capacitance

Having discussed the non-linear capacitance and its calculation scheme for the overall granular BST material, the analysis for voltage waveforms propagating over an actual transmission line and their rise-times is presented.
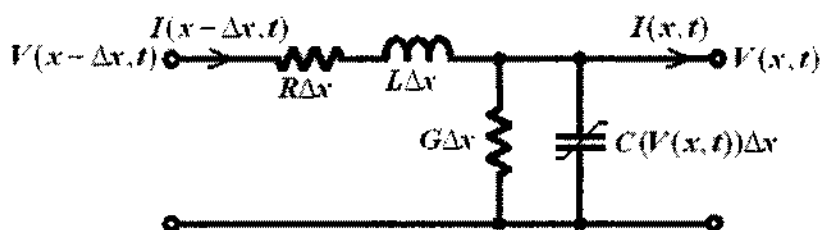
Figure 3-11. Circuit model for an infinitesimal, internal element of a nonlinear transmission line.

Consider a nonlinear transmission line of length l terminated with a load resistance R_L. A distributed circuit model for an infinitesimal, internal element of length Δx is depicted in Figure 3-11. Here R, L, G, and C are the resistance, inductance, conductance, and capacitance per unit length, respectively. C is voltage dependent and defined in Equations (3-26)~(3-28). By applying the Kirchhoff current and voltage laws, one obtains:

$$V_x(x,t) = -LI_t(x,t) - RI(x,t), \tag{3-29a}$$

$$I_x(x,t) = -GV(x,t) - C(V(x,t))V_t(x,t) , \tag{3-29b}$$

where the subscripts, x or t, denote the partial derivative with respect to x or t.

Combining the above equations yields the following second-order, quasi-linear partial differential equation (PDE) governing the internal voltage of the transmission line:

$$V_{xx}(x,t) = LC(V(x,t))V_{tt}(x,t) + RGV(x,t) +$$
$$[LG + RC(V(x,t)) + LC'(V(x,t))V_t(x,t)]V_t(x,t). \qquad (3\text{-}30)$$

Termination of the transmission output end by a load resistance, R_L, leads to the relation:

$$I(l,t) = \frac{V(l,t)}{R_L}, \qquad (3\text{-}31)$$

where "l" is the total transmission line length. The boundary condition at the terminal end is then:

$$V_x(l,t) = -\frac{L}{R_L}V_t(l,t) - \frac{R}{R_L}V(l,t). \qquad (3\text{-}32)$$

For a specified input voltage, $h(t)$, the boundary condition at the input end is prescribed as:

$$V(0,t) = h(t) \qquad . \qquad (3\text{-}33)$$

We also assume that the initial voltage (and its temporal derivative) at each point on the transmission line is zero. Thus:

$$V(x,0) = 0, \qquad (3\text{-}34a)$$
$$V_t(x,0) = 0, \qquad (3\text{-}34b)$$

With the above equations, the transmission line voltage $V(x,t)$ can be solved numerically. Some parameters used in our simulation are listed in Table 3-4.

Table 3-4. Parameters used in the transmission line model.

$L = 3\mu H/m$	$R = 0.3m\Omega/m$	$G = 0.5nS/m$
$\Delta t = 0.4ns$	$\Delta x = 0.1m$	$l = 10m$

CHAPTER IV

SIMULATION RESULTS AND DISCUSSION

4.1   Introduction

Some relevant and selected simulations results, together with their analyses and discussions, are given in this chapter. The modeling of ZnO varistors introduced in sections 3.1, 3.2 and 3.3 was carried out on the basis of a 2D Voronoi network and the associated nonlinear resistance circuit network. The pertinent simulation results and discussion are presented in sections 4.2 and 4.3. The simulation results and discussions relating to the TiO2 breakdown under a pulsed condition have been given in section 4.4. Finally, the results of nonlinear transmission line, using barium strontium titanate (BST), are discussed in section 4.5.

4.2   Simulation Results and Discussion of Current – Voltage Characteristics of ZnO Varistors

4.2.1. Influence of "Bad" and "Ohmic" Grain Boundaries in ZnO varistor

As introduced in section 2.4, good grain boundaries have high leakage resistance and high nonlinearity ($\alpha \geq 30$) and their relative percentage in ZnO samples have been reported to vary from 15% to 60%. Bad microjunctions have 2-3 orders of magnitude lower leakage resistance and much lower nonlinearity ($\alpha \approx 10$), with relatively lower percentages of around 30%-35%. Ohmic, or nearly ohmic, microjunctions with resistances that are 2-5 orders of magnitude lower than the leakage resistances of the

good junctions are also found. The percentage of such microjunctions has been estimated to be between 5% and 10%.

To determine the influence of "bad" and "ohmic" grain boundaries on the current-voltage characteristics, two separate models were setup to evaluate and assess the role of the J-V characteristics. One was an ideal composite consisting only of "good" grain boundaries, while the other was a real ZnO composite in which the percentage ratio of "good", "bad", and "ohmic" boundaries numbers was taken to be: 60% : 35% : 5%. The result is shown in Figure 4-1 [94]. As might be expected, the currents are much lower at the lower voltages for the "ideal" case (i.e. sample with all good grain boundaries), and a much sharper transition is seen. The nonlinear coefficient of the ideal case is 50.8, but the heterogeneous case is only 36.7, so increasing the percentage of "good" grain boundaries will improve the nonlinearity of the ZnO varistor. But, in practice, trying to physically achieve this target will require lot of experimental research work and process improvements of the fabrication technology.

4.2.2. The Nonuniformity of Spacial Current Distributions

The non-uniform growth of a ZnO grain during the sintering process leads to a variety of ZnO grain sizes and microstructure shapes. This variability arises, in part, due to such factors of the ZnO fabrication technology as: a variety of raw material particle sizes, the unevenly mixed raw materials, the difference in density of the biscuit, and so on. In addition, the additives often do not get evenly mixed, and this causes differences in the components. Due to the highly nonlinear coefficient associated with the J-V characteristics of grain boundaries, the current flowing through ZnO varistors is often
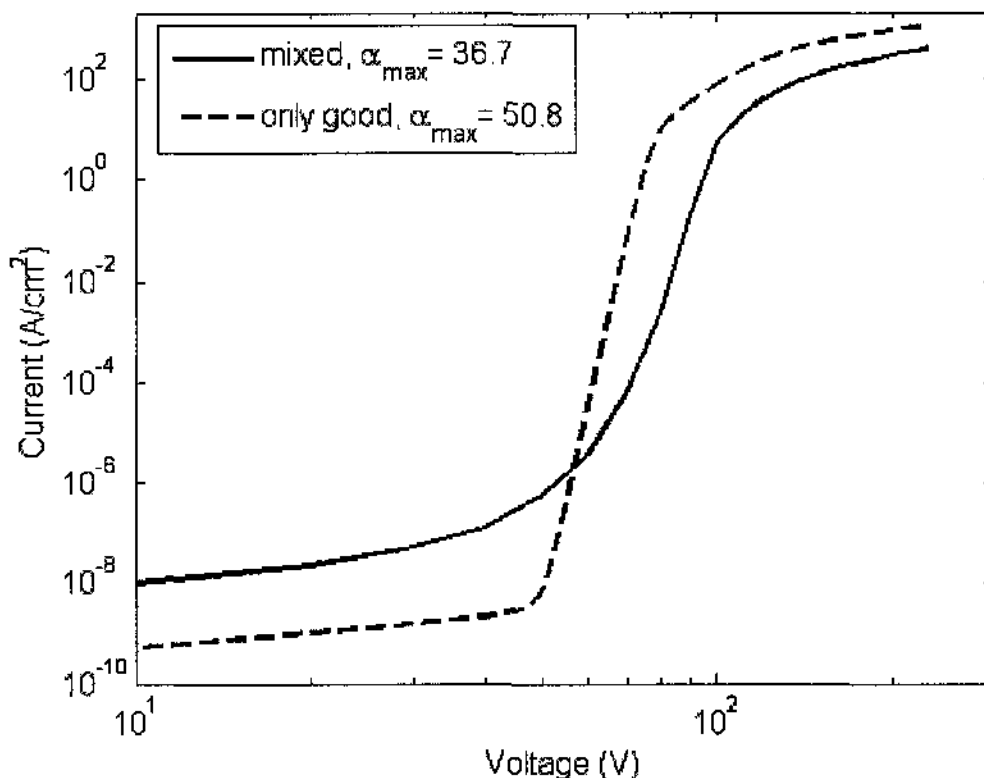
Figure 4-1. *J-V* comparison between 586 cell samples with idealized "good" grain boundaries and heterogeneous grain boundaries [94].

concentrated over some internal paths containing fewer ZnO grains, higher nonlinear coefficients, and lower internal resistances. Figure 4-2 shows the spatial current distributions within the model for different bias voltages and different values of disorder parameters. Figure 4-2 clearly shows that:

(1)   If the disorder parameter is the same (e.g. 5 or 1), then the lower the bias voltage (e.g. 40V), the higher is the non-uniformity of current distributions.

(2)   If the bias voltages are the same (e.g. 40V or 70V), then the higher the disorder parameter (e.g. 5), the higher the internal non-uniformity of current distributions.

(3)   If the bias voltages (e.g. 40V or 70V) and disorder parameter are the same (e.g. 5), then the larger the average grain size and the higher the non-uniformity in current distribution.

(4)   In addition, from the values marked on the color bars, especially under higher bias voltage, one can observe that the higher the disorder parameter, or the larger the average grain size, the higher is the maximum current magnitude flowing through the ZnO samples. This higher current will lead to higher temperature variations and larger thermal stresses in the ZnO ceramics samples. For example, comparing cases shown in Figures 4-2B, 4-2D, and 4-2F, the maximum current of Figure 4-2B is roughly 7 times higher than that shown in Figure 4-2D, and roughly 27 times higher than that of Figure 4-2F. The results indicate that increasing the uniformity of ZnO grain size (i.e. reducing the value of disorder parameters) or reducing the average grain can improve the uniformity of current distribution, and thus, reduce the amplitude of maximum current within the ZnO varistor.

4.2.3. Current-Voltage (J-V) Characteristics Under Different Disorder Parameters and Average Grain Sizes

The current-voltage (J-V) characteristics of ZnO varistors are determined by the J-V capability of individual grain boundaries, the varistor dimension, average grain size and disorder parameters. Figure 4-3 shows the varistor J-V characteristics with different
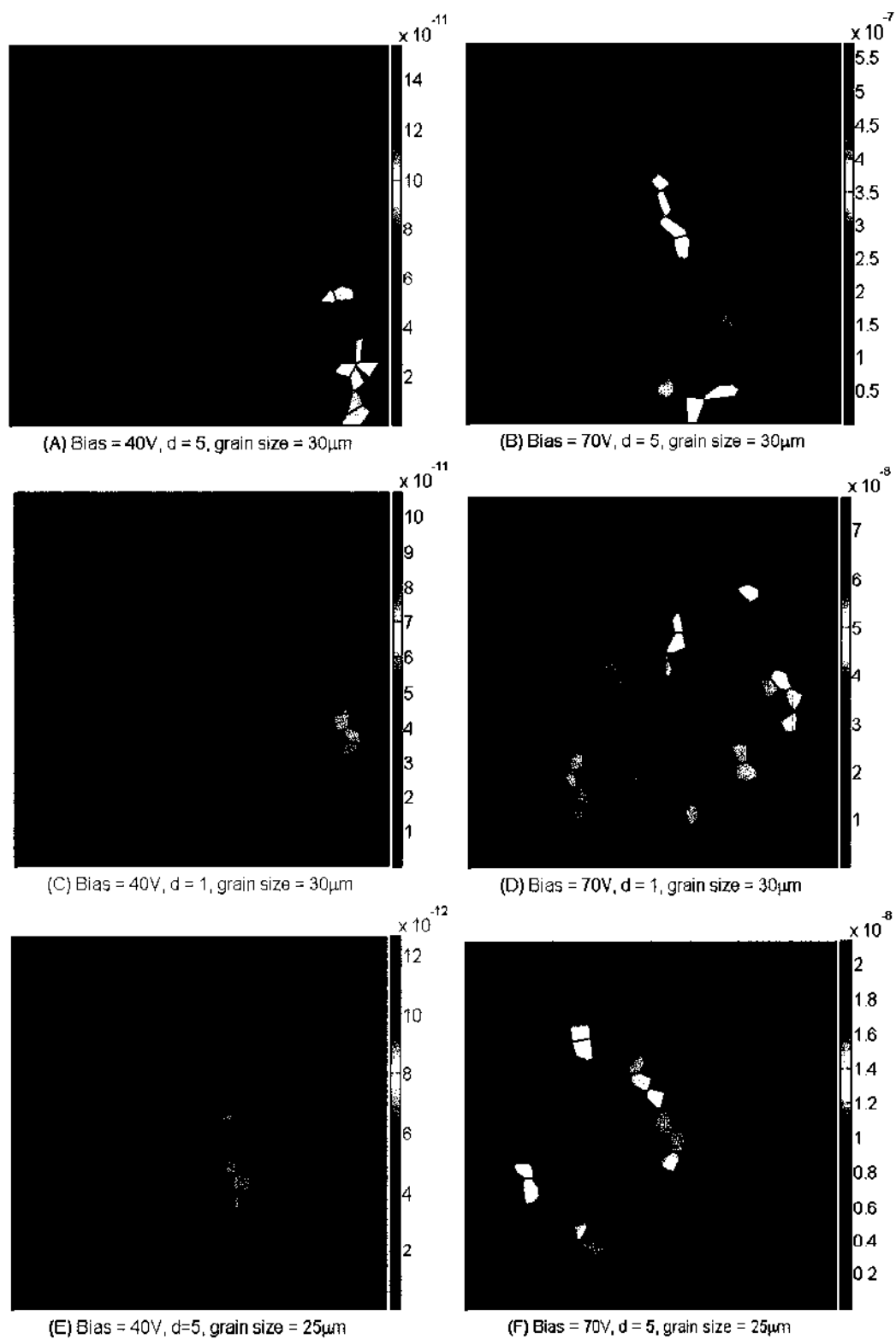
Figure 4-2. Comparison of spacial current distributions under different voltages and different values of disorder parameter d (average grain sizes are 30μm or 25μm, and the sample dimension is 300μm X 300μm X 30μm, bias voltages are 40V or 70V).

disorder parameters. The varistor with a lower disorder parameter is seen to have lower leakage current density under low voltage biasing and a larger breakdown voltage and higher nonlinear coefficient α. This is because varistors with lower disorder parameters have more uniformity in their current distribution and higher resistances, as discussed in section 4.2.2.
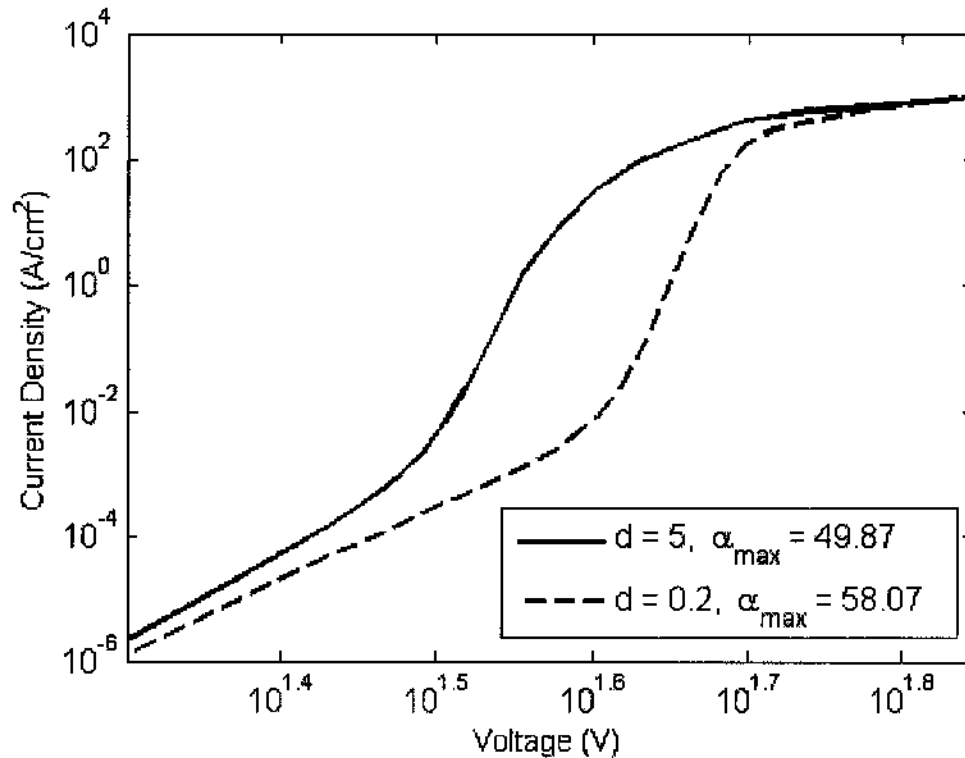
Figure 4-3. J-V characteristics under different values of disorder parameters (average grain size = 30μm, sample dimension 300μm X 300μm X 30μm).

With the same disorder parameters and same sample dimension, the varistor J-V characteristics for different average grain sizes are depicted in Figure 4-4. This figure indicates that the smaller the average grain size, the higher the breakdown voltage of ZnO varistors. This means with the same current injection, varistors with smaller average grain size have a higher voltage gradient or higher surge energy absorption capability.

The average size of the ZnO grain of common ZnO varistor ceramics is about 15μm

as discussed in Reference [12], while that of high voltage gradient is about 9μm. The

latter is only 0.6 times that of the former, but it has 2.3 times the surge energy absorption

capability as compared to the former. Hence, developing a high voltage gradient ZnO

varistor (with smaller average grain size) will be an important and promising direction

within the ZnO varistor industry.
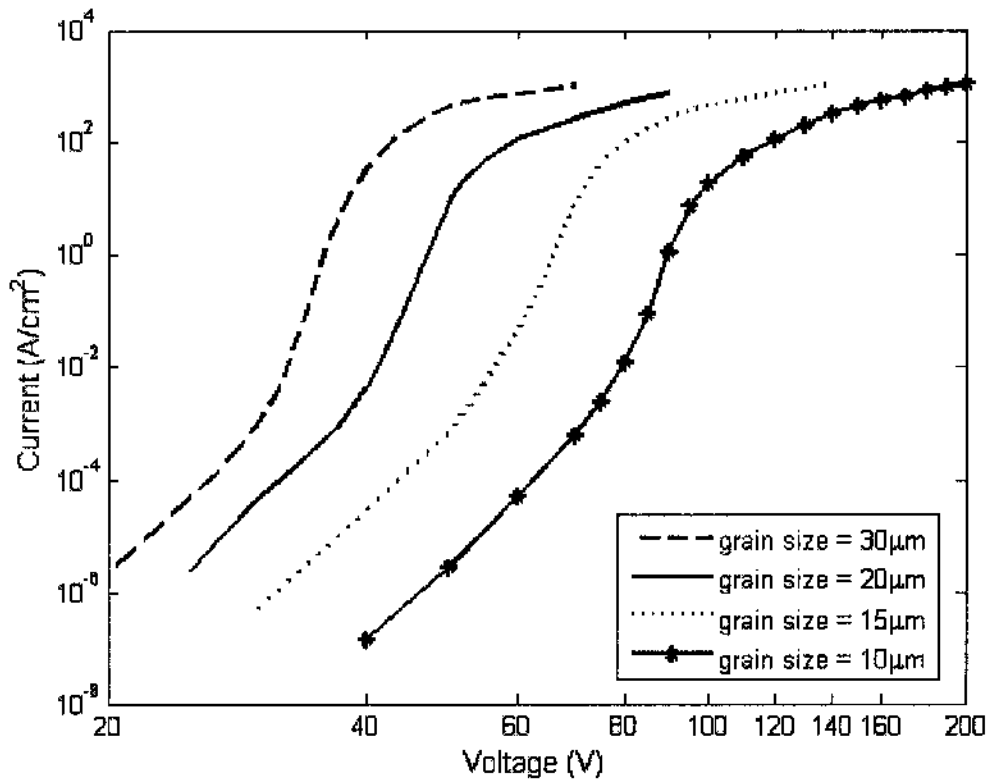
Figure 4-4. J-V characteristics under different average grain sizes (disorder parameter d = 5, sample dimension 300μm X 300μm X 30μm).

4.3 Simulation Results and Discussion of Electrical and Thermal Characteristics of ZnO Varistors Under High Current Density

4.3.1. Bias Voltage and Electric Fields Under High Current Density

Figure 4-5 shows the global bias voltage for the d=1 and d=5 cases, necessary to drive a sample current density of 100 A/cm^2. A Voronoi network with 492 grains and a Gaussian distribution of barrier voltages V_B was used for the simulation results shown in Figure 4-5. The bias voltage was selected by varying its value for the given Voronoi network until the 100 A/cm^2 current density was obtained. As evident from Figure 4-5, the bias voltage is predicted to increase as the disorder parameter gets smaller. A higher disorder parameter, "d", implies a more heterogeneous granular structure with higher grain size variability. A sample with a higher disorder parameter tends to have many more grains that are larger than the average size. If a collection of such larger grains happens to lie within a random anode-to-cathode path, then the number of grain
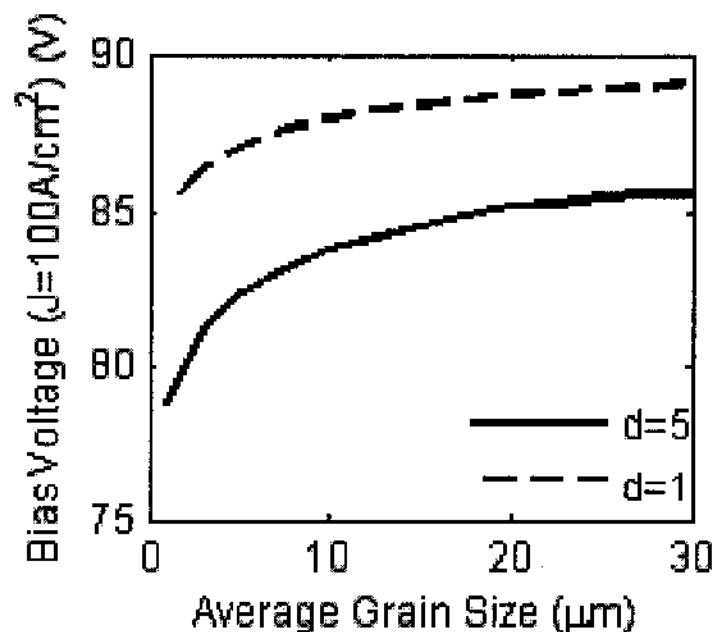
Figure 4-5. Variation of bias voltage with different grain sizes for a current density J=100 A/cm^2.

boundaries encountered between the electrodes would correspondingly be lower. Since the sample resistance mainly comes from grain boundary contributions, such a random path between the electrodes would present the weakest resistance to current flow and allow for the highest Joule heating. Thus, the presence of such heterogeneous grains provides a larger probability for current channeling via a low resistance path. The net result would be a decrease in the requisite bias voltage as predicted here in our simulations.

Based on the results of Figure 4-5, the average electric field across the simulated sample was computed as the grain size varied from 30 μm down to 1μm. This grain size reduction corresponds to a decrease in sample dimensions by 96.7%. The bias values

Figure 4-6. Variation of average electric field for different grain sizes and a current density J = 100 A/cm^2.

shown in Figure 4-5 correspond to voltage reductions in the 4%-9% range for the two disorder parameter values. The average electric field of Figure 4-6, however, increased roughly 27 times with reductions in sample dimensions. From a practical standpoint, this

boundaries encountered between the electrodes would correspondingly be lower. Since the sample resistance mainly comes from grain boundary contributions, such a random path between the electrodes would present the weakest resistance to current flow and allow for the highest Joule heating. Thus, the presence of such heterogeneous grains provides a larger probability for current channeling via a low resistance path. The net result would be a decrease in the requisite bias voltage as predicted here in our simulations.

Based on the results of Figure 4-5, the average electric field across the simulated sample was computed as the grain size varied from 30 μm down to 1μm. This grain size reduction corresponds to a decrease in sample dimensions by 96.7%. The bias values

Figure 4-6. Variation of average electric field for different grain sizes and a current density J = 100 A/cm^2.

shown in Figure 4-5 correspond to voltage reductions in the 4%-9% range for the two disorder parameter values. The average electric field of Figure 4-6, however, increased roughly 27 times with reductions in sample dimensions. From a practical standpoint, this

implies that if varistors with smaller grain sizes were fabricated then the device size would be reduced dramatically, while maintaining the biasing voltages at an approximately constant level. The advantages of a more compact varistor with negligible loss in the high-voltage strength are obvious. The result of Figure 4-6 arises in part to the strong role of the grain boundary and the minimal resistance offered by the bulk granular regions. Hence, shrinking the grain size merely changes the grain bulk resistance without altering the average number of grain boundaries in samples subjected to a given applied electric field. Since the grain bulk resistance has a small role, the biasing voltage capability remains practically unchanged.
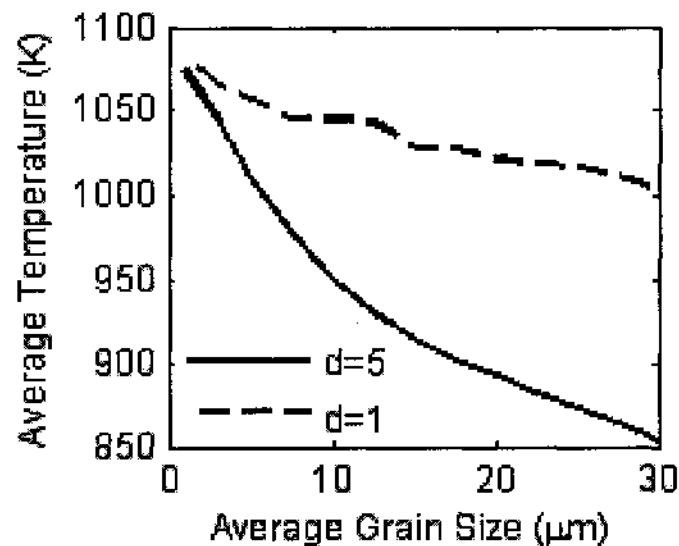
Figure 4-7. Variation of global average temperature with grain size when the maximum temperature is 1093°K.

4.3.2. Internal Temperature, Thermal Stress, and Dissipated Energy Under High Current Density

Time-dependent simulations were carried out starting with the bias voltages of Figure 4-5 until the maximum temperature of the samples reached the 1093 K melting point. Figures 4-7 and 4-8 show the global average temperature and maximum thermal stress for different grain sizes, respectively. These plots are snapshots obtained at the instants when the melting points were reached.
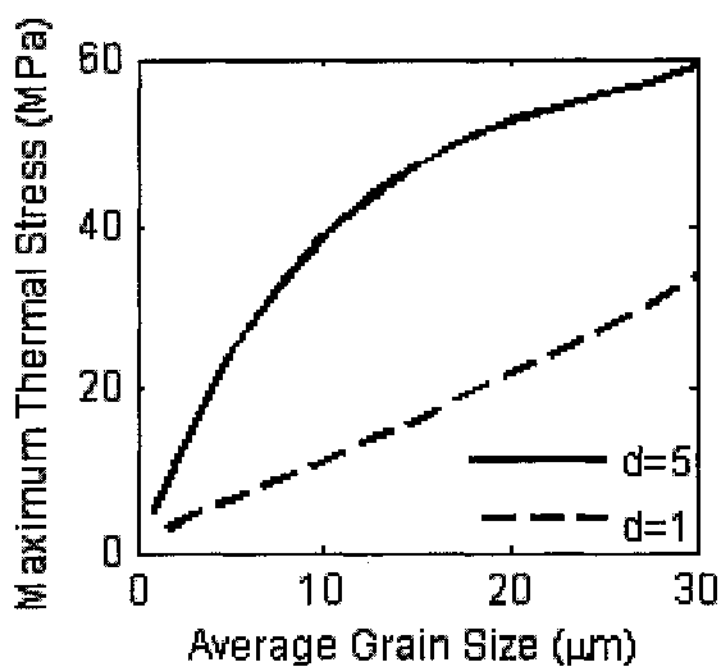
Figure 4-8. Variation of maximum thermal stress with ZnO average grain size when the maximum temperature is 1093°K.

In Figures 4-7 and 4-8, the smaller the grain size, the higher the global average temperature and smaller the maximum thermal stress. Also, the lower the disorder parameter, (d=1), yields a higher global average temperature and smaller maximum thermal stress. Furthermore, the smaller the grain size, the lower the difference in average temperature and maximum thermal stress between the d=1 and d=5 cases. For

example, for the 1 μm average grain size, the differences in temperature and stress were as small as 9.2 K and 3.04 MPa, respectively, between the d=1 and d=5 configurations. These differences were the highest at 150.7 K and 25.32MPa for a 30 μm average grain size. Very simply, these results imply that if the average grain size can be made sufficiently small, individual variances in grains will have a minimal affect on the thermal characteristics of ZnO varistors. In addition, the maximal thermal stress is predicted to be the lowest for smaller grains, indicating an optimal strategy for practical varistor design. The small granular structures would also be less prone to cracking and heat failures.

Qualitatively, the smaller the average grain size, the higher the predicted bias field necessary for maintaining a given average current density in a given sample. This arises from the larger number of grain boundaries presented in smaller average grain size samples. Hence, the Joule heating is correspondingly larger with smaller grains and leads to increased internal temperatures. However, the thermal stress decreases with decreasing average grain size. This occurs because deviations in individual grains decrease as the average size becomes small. Since thermal stress originates from spatial gradients in temperature, small grains and more homogeneous distributions (e.g. d=1 as compared to d=5) decrease the thermal stress magnitude.

Figure 4-9 shows the global average energy density for different grain sizes and the disorder parameters d=1 and d=5. Here again, time-dependent simulations were run for the bias voltages of Figure 4-5 until the maximum temperature of the samples reached the 1093 K melting point. The average energy density with samples where d=1 is about 40%-50% higher than that for d=5. This again underscores the possibility of having

strong non-uniform current flows and localized heating in the more heterogeneous d=5 samples. In such cases, while specific regions would get quite hot, the overall average energy dissipated in the entire sample need not be as large. In addition, with grain size changing from 30 μm to 1 μm, the average energy density is predicted to increase by about 20%-30%. This is simply the result of the higher bias field necessary to sustain the initial 100 A/cm² current density.
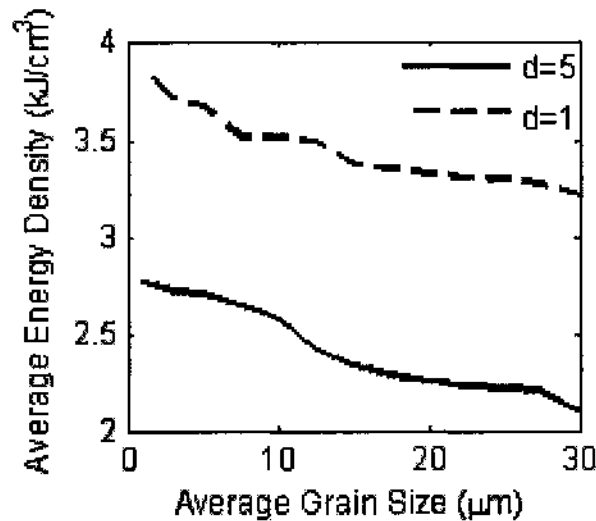
Figure 4-9. Relationship between global average energy density and grain size at times when the maximum temperature of 1093 K was reached.
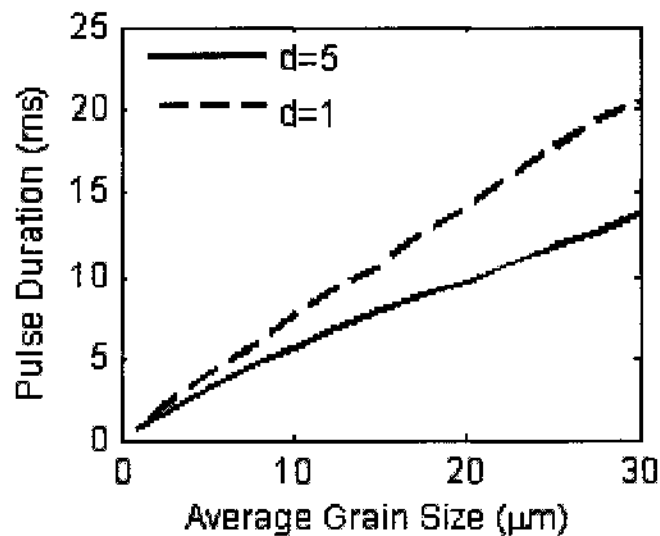
Figure 4-10. Relationship between bias durations and grain sizes corresponding to the maximum 1093 K internal threshold.

Figure 4-10 shows the variation in bias duration until localized melting for different grain sizes and disorder parameters. The relationship between the voltage duration and average grain size is roughly linear in Figure 4-10. Also, the bias duration for d = 1 is predicted to be longer than that for the d = 5 case, with the difference becoming smaller as the grain size reduces from 30 μm to 1 μm. This overall result is in keeping with the trends seen in Figure 4-7. With smaller average grains, the average internal temperatures generated are larger. Consequently, the external bias can only be applied up to a shorter duration before internal melting and sample damage. Hence, while reductions in grain size have the advantage of higher hold-off fields and more compact structures, this occurs at the expense of shorter external voltage durations. Alternatively, better thermal management and heat dissipation systems would be needed for the more compact varistors.

Table 4-1. The relative changes of properties when grain size changes from 30 to 1 μm.

Properties	d = 1	d = 5
Grain size	−96.7%	−96.7%
ZnO Sample volume	−99.996%	−99.996%
Bias voltage ($J=100A/cm^2$)	−4.4%	−7.9%
Average electric field	2767%	2663%
Average temperature	+8%	+26%
Maximum thermal stress	−94.6%	−91.7%
Average energy density	+20.4%	+31.9%
Bias duration	−95.6%	−95.1%

Table 4-1 lists the relative changes of the relevant electrical properties of the micro-structured ZnO varistors with changes in the average grain size from 30 μm to 1 μm. The benefits of down-scaling the internal granularity are obvious. Strong reductions in maximum thermal stress and sample size are predicted with negligible changes in hold-off voltage and average temperature. The average energy density is predicted to increase by about 20%, with a very large increase in average electric field. In addition, the d=1 configuration has advantages in terms of a lower temperature increase and hold-off voltage shift and smaller energy density. Hence, greater uniformity within small-grained samples should be preferred as a general rule of thumb.

4.3.3 Spatial Distribution of Current and Temperature Under High Current Density

Internal temperature profiles and current distributions were also obtained from the time-dependent simulations. For concreteness, the case of d=5 and 10 μm average grain size is presented first and shown in Figure 4-11A. The plot is a 5.8 ms snapshot of the internal maximum current magnitude distribution. The highest density in Figure 4-11 is roughly at the lower left side, around the (0.2, 0.05) region. This also corresponds to the localized melting zone (maximum temperature of 1093°K) as predicted in Figure 4-12A.

For completeness, the above calculations of the time-dependent internal temperatures and thermal stresses were repeated for a lower (d=1) disorder parameter. The spatial distribution of the internal current magnitude and local temperature are given in Figures 4-11B and 4-12B, respectively. The internal current distribution shows much greater homogeneity as compared to that in Figure 4-11A. This is to be expected given

the smaller disorder (d=1) value. Also, a much smaller fraction of the simulation space exhibits high currents. The temperature profile of Figure 4-12B similarly exhibits lesser channeling and filamentary features.
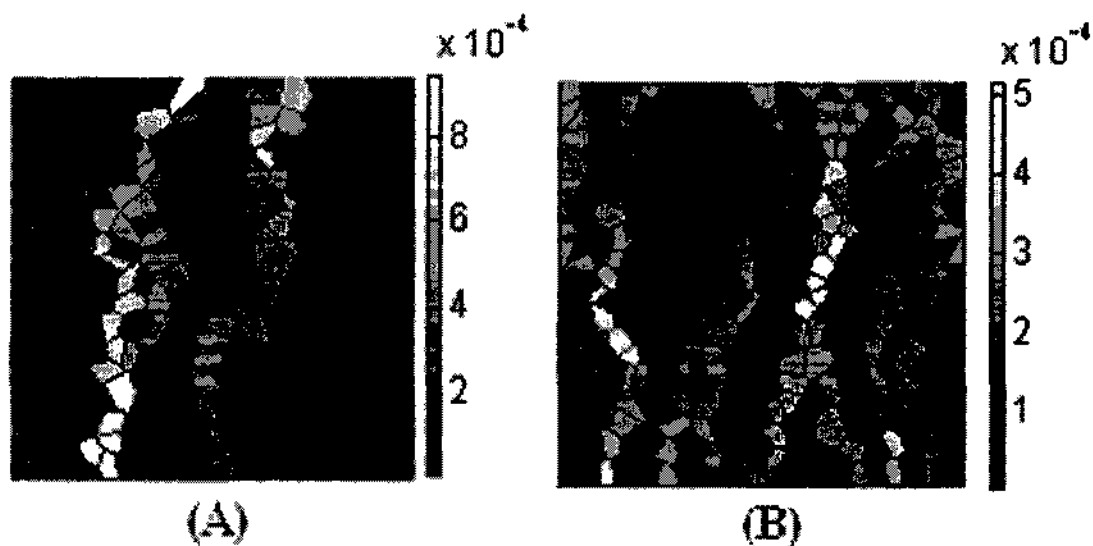
Figure 4-11. Snapshot of the internal current magnitude distribution, (A) d=5, (B) d=1. (Average grain size = 10 μm, and vertical scale denotes current in Amperes.)
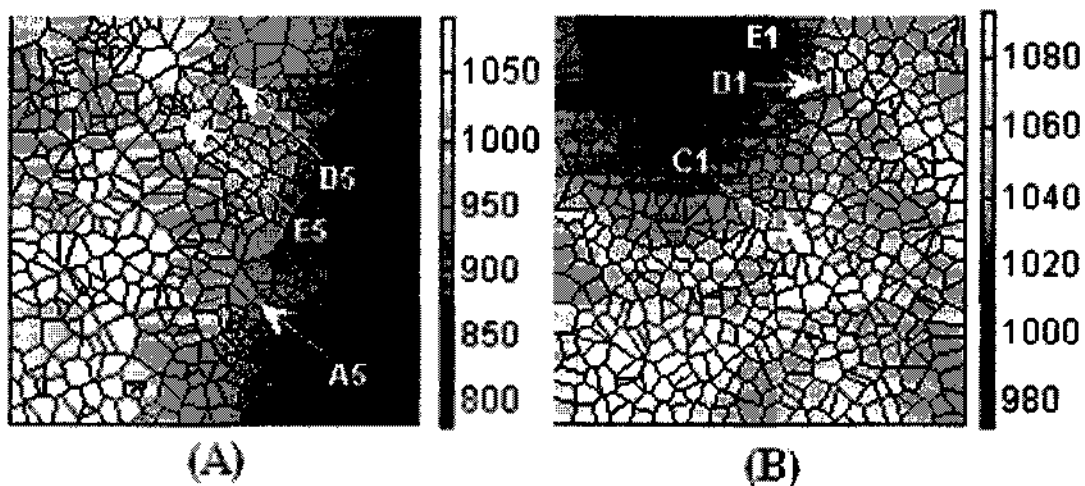
Figure 4-12. Snapshot of the temperature distribution. (A) d=5, (B) d=1. (Average grain size = 10 μm. Vertical scale denotes temperature in Kelvin. Some specific locations are marked.)
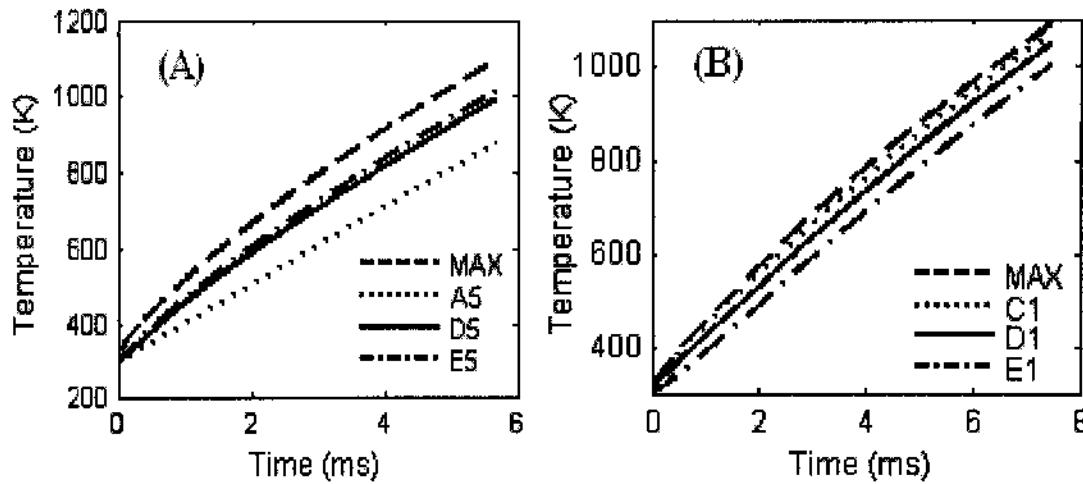
Figure 4-13. Time dependent temperatures at locations shown in Figure 4-12. (A) d=5, (B) d=1. (Average grain size = 10 μm. The simulation was terminated when the maximum temperature reached 1093°K)
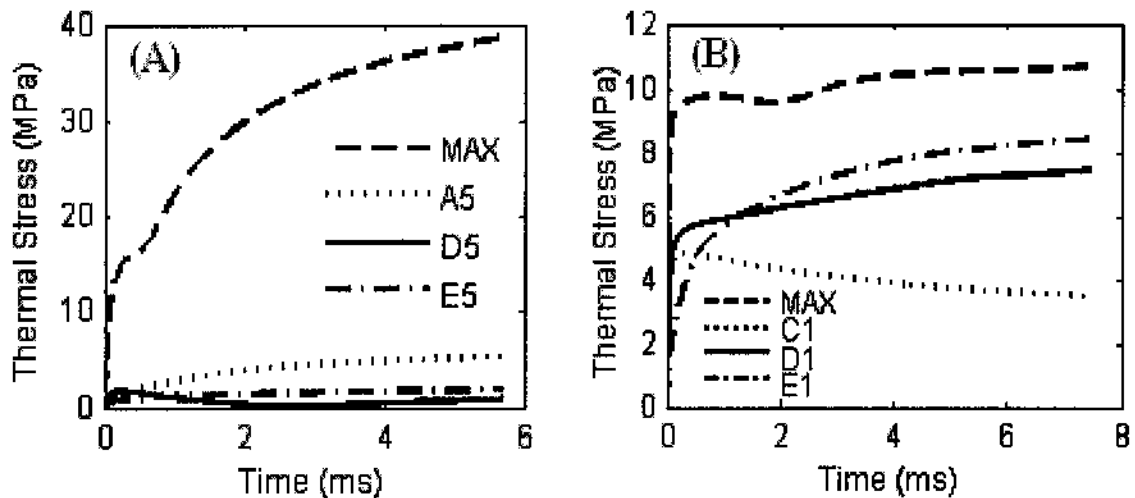
Figure 4-14. Dynamic thermal stress at locations shown in Figure 4-12. (A) d=5, (B) d=1. (Average grain size = 10 μm.)

4.3.4 Dynamic Temperatures and Thermal Stresses

For concreteness, simulation results of the internal temperature evolution at four specific locations within the sample (as indicated in Figure 4-12A) are shown in Figure 4-13A. As might be expected, the temperatures increase at all the chosen points as currents

continually flow. However, the non-uniformity in heating is obvious. The lowest temperature at ~5.8 ms is about $875°K$, while the highest is at the 1093 K melting point. Time-dependent changes in thermal stress at the same four locations within the sample are shown in Figure 4-14A. For some of the locations, the order of the thermal stress curves is different from that for the temperatures. The maximum stress in Figure 4-14A is predicted to be about 39 MPa and is much less than the 137.9 MPa critical threshold needed for material cracking.

The internal temperature evolution for d=1 and average grain size of 10 μm, at the locations indicated in Figure 4-12B, is shown in Figure 4-13B. The curves are similar to those of Figure 4-13A but with much less spread. Simulation results for the time-dependent internal thermal stress are shown in Figure 4-14B. Again, the behavior is similar to that of Figure 4-14A but with much less variability. The thermal stresses at the locations follow a different relative sequence from their corresponding temperatures. The largest thermal stress in Figure 4-14B is predicted to be much smaller at about 10.5 MPa, as compared to ~39 MPa in Figure 4-14A.

4.3.5 Dynamic Grain Boundary Melting Sequences

Figure 4-15 shows the snapshot of GB melting and its temporal sequence for the d=5, ZnO sample of Figure 4-11A. The localized melting and transition into a more resistive state, changes the current distribution and forces the conductive flow around the hot spot. Subsequently, neighboring regions around the initiating zone begin to get hot. A progression of hot spots and the affected grain boundaries is evident in Figure 4-15. The sequence of internally melted GBs is numbered and can be seen moving on either

side of an initial "seed GB". For clarity, the cluster of GBs in the bottom-right region of Figure 4-15 has been enlarged to better show the sequence numbering. This spatial disturbance affects the internal current flow and subsequent heat generation.

The sequence of internal GB melting for the d=1 case is shown in Figure 4-16. The regions marked correlate well with the hot spots of Figure 4-12B. Since the non-uniformity in current distributions for this d=1 case is less pronounced than for the d=5 situation, there are fewer regions with large temperature differentials. Hence, instead of a few localized regions of very high temperature and melted GBs, a more gradual and smoother heating pattern results. The net effect is that after a suitably long pulsing duration, more numerous melted GB regions occur within the sample. Thus, the number of "melted GBs" seen in Figure 4-16 is higher and relatively more spread out than in Figure 4-15.
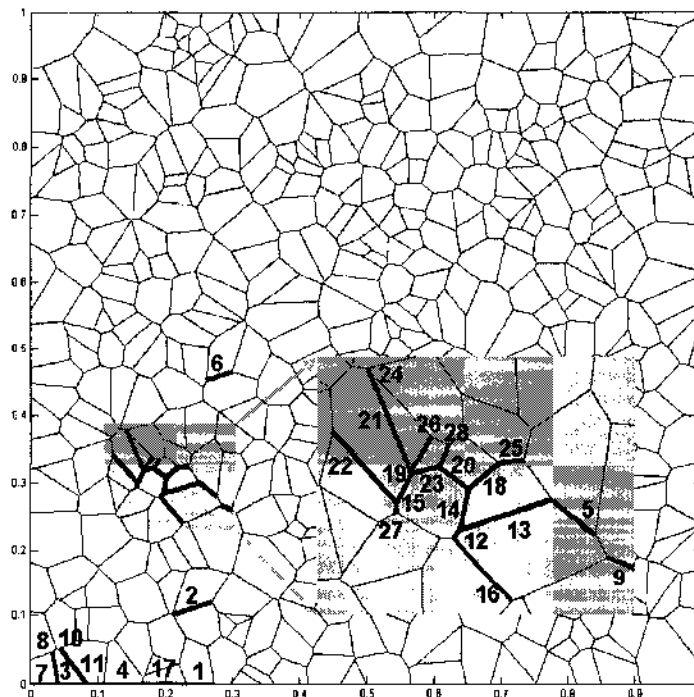
Figure 4-15. A 5.8 ms snapshot showing the grain boundaries in the granular ZnO sample with d=5. The numbers denote the melting sequence and the bottom-left shaded portion has been enlarged to reveal the numbers.
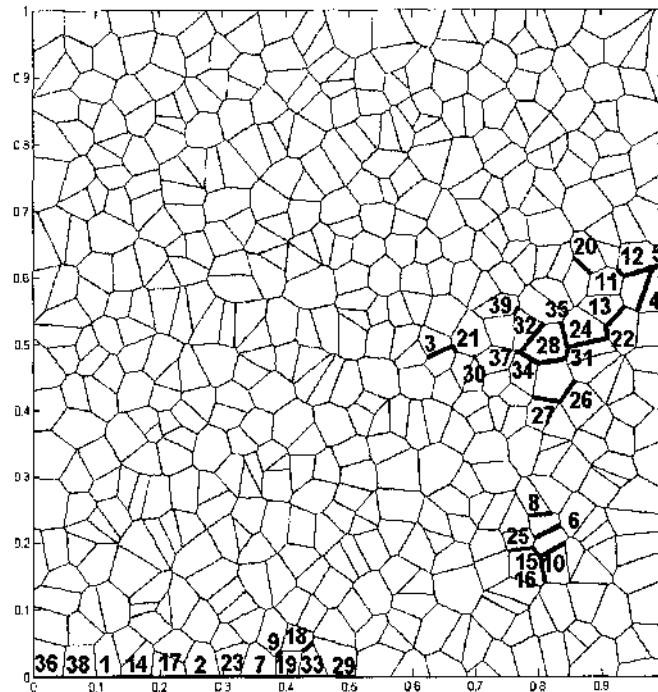
Figure 4-16. Snapshot showing the grain boundaries in a d=1, ZnO sample. The numbers denote the melting sequence.

4.3.6 The Influence of Pores

In order to investigate the effect of microscopic pores within the ZnO structure, simulations with pores were carried out with disorder parameters of d=1 and d=5. The detail results are listed in Table 4-2. Figures 4-17~18 show the comparisons of dynamic stress and temperature with the case of no pores. The simulation shows that the sample with pores has higher thermal stress, larger resistance, and needs a slightly higher bias voltage to maintain the current density of $100A/cm^2$. Also, such pored samples had lower power dissipation and reached the 1093 K melting temperature with a shorter pulse duration. Also, the average temperature was somewhat lower.

Table 4-2. Comparison of simulations with/without pores.

Average grain size = 10 μm	d = 5		d = 1	
	no pores	pores	no pores	pores
Max Stress (MPa)	38.68	43.31	10.74	21.30
Energy (10^{-4} J)	9.582	8.965	13.59	11.90
Energy density (J/cm^3)	2480	2320	3517	3080
Average temperature (K)	950.8	901.7	1045	1017
Duration (ms)	5.676	5.346	7.477	6.557
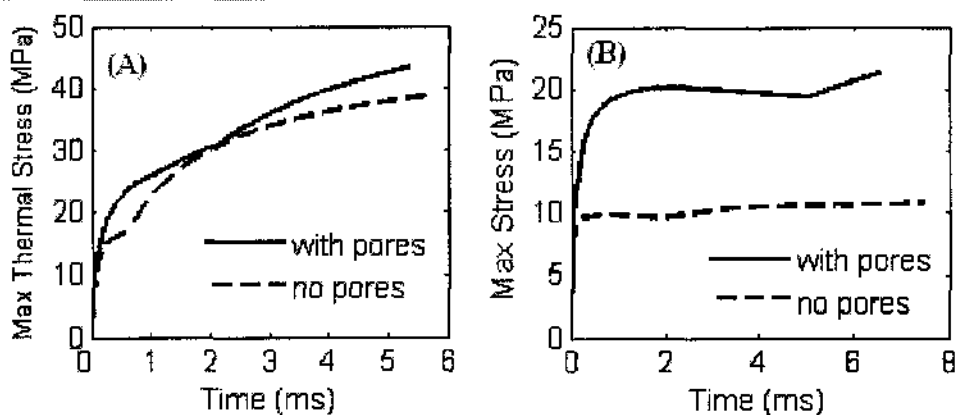
Figure 4-17. Comparison of max thermal stresses, (A) d = 5, (B) d = 1. The average grain size was 10 μm.
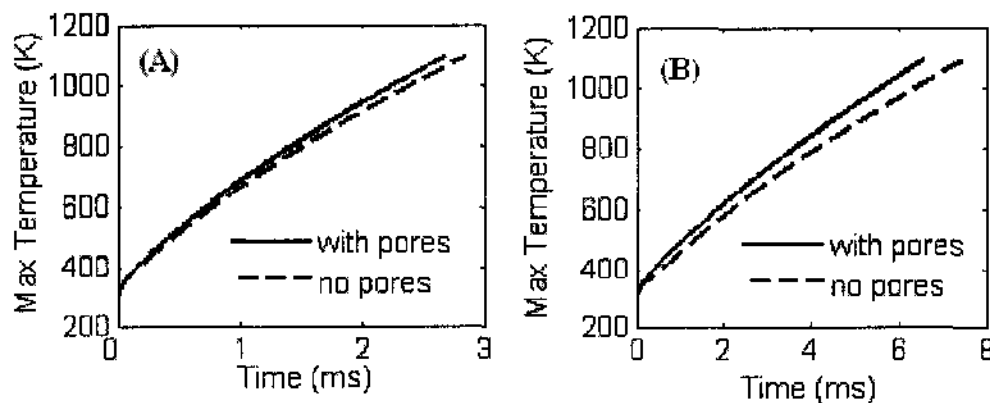
Figure 4-18. Comparison of max temperatures, (A) d = 5, (B) d = 1. Average grain size was 10 μm.

4.4   Simulation Results and Discussion of TiO₂ Breakdown Under Pulsed Conditions

Based on the model introduced in Section 3.4, simulations were carried out for two different voltage waveforms applied to a TiO_2 sample. One was a linear ramp with variable slope to mimic the slow turn-on voltage actually used under experimental testing conditions. The other waveforms were rectified sine pulses. The breakdown voltage and the time instant were obtained from the simulation when the device current began increasing without bound. Results for the linear ramp excitation (i.e., quasi-DC), starting from 0V, are given in Table 4-3. The breakdown times for the 10^7 V/s, 10^8 V/s, and 10^9 V/s ramped cases were 0.157 ms, 0.01628 ms, and 1.775 μs, respectively. Clearly, a faster ramp is seen to produce a higher breakdown voltage.

Table 4-3. Breakdown voltage under ramp DC bias.

Ramp Slope (V/sec)	10^7	10^8	10^9
Breakdown voltage (V)	1569.7	1628	1775
Breakdown field (V/cm)	628	651	710

The bias V(t) for rectified sine-wave excitation was taken to be:

$$V(t) = \left| A \cdot \sin\left(\frac{\pi \cdot t}{A \cdot k \cdot 10^{-9}} \right) \right| ,$$ (4-1)

The parameter "k" in Equation (4-1) above is a measure of the initial slope, and hence, provides a rough comparison with the ramped voltage case. Multiple sine-waves were used until device breakdown. The results obtained are tabulated in Table 4-4. The "front"

and "tail" in Table 4-4 denote the rising and falling portions of the applied sinusoidal waveform.

The following features become evident from Table 4-4. (i) As the peak field is reduced, there is a greater chance that breakdown occurs later in time and requires more pulses. For example, the 655 kV/cm case is predicted to break down within the first pulse, while the reduced 628 kV/cm bias requires six-pulses before breakdown. (ii) A cumulative, memory effect is thus manifested in the device response. (iii) For a slower rise in voltage (i.e. a higher "k" value in Equation (4-1)), the breakdown field decreases, all other parameters being fixed. This is again indicative of finite time-requirements for the inherent processes leading to final breakdown. (iv) Under multiple-pulse bias, the breakdown voltage changes rapidly with the pulse peak value. A small change in the peak value can lead to a big change in breakdown field. Hence, multi-pulse breakdown voltages cannot be used as a unique measure of the insulation strength. (v) In comparison to "quasi-DC" excitation, *lower breakdown voltages can result* under multiple pulsing. This is in agreement with the experimental data of Table 2-1. For example, breakdown voltages of 1569.7 V and 1775 V are predicted for the 10^7 and 10^9 V/s ramps. However, a much lower threshold of 1374.1 V results for the sinusoidal pulsed excitation.

Table 4-4. Breakdown fields under sine-pulses.

Slope / Peak field	10^9 V/sec		2×10^9 V/sec	
655 kV/cm	653 kV/cm	1st tail	571 kV/cm	1st tail
640 kV/cm	639 kV/cm	2nd front	636 kV/cm	4th tail
636 kV/cm	608 kV/cm	2nd tail	611 kV/cm	6th tail
632 kV/cm	550 kV/cm	3rd tail		
628 kV/cm	628 kV/cm	6th tail		

The cumulative effect can be seen more clearly from the time-dependent free-electron population during different pulses, shown in Figure 4-19. The applied voltage pulses are also included for brevity. The maximum bias was 1570 V and corresponds to the last row of Table 4-4. The gradual and progressive rise in free-carrier density (on a "semi-log" scale) is obvious. In this multiple short-duration "pulsed-burst" scenario, trapped electrons are periodically released within the device upon voltage application. These electrons do not have the requisite time, nor are they subjected to the continued high fields necessary for driving them out of the semiconductor. Hence, a cumulative build-up of mobile charge occurs. This, in turn, progressively enhances the electron production through impact ionization as the "baseline electron population" increases. Eventually an electron driven avalanche breakdown occurs.
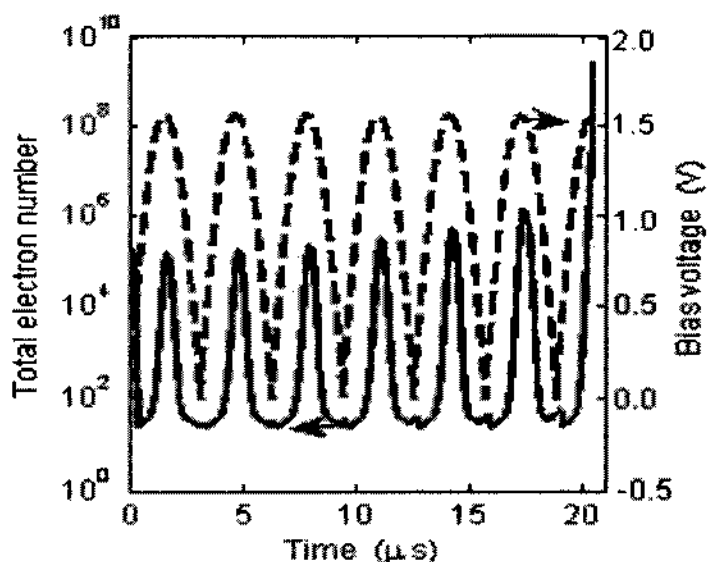
Figure 4-19. Time dependent free-electron density in TiO_2. The applied voltage pulses are also shown for brevity.

The cathode emission current in the TiO_2 device shows negligible cumulative effects as illustrated in Figure 4-20. This implies that the breakdown is mainly due to

bulk impact ionization and not through cathode emission. The simulations also indicated that breakdown was initiated from the cathode end. The free electron density profile just prior to breakdown is given in Figure 4-21. The electron density at the cathode end is almost 1000 times larger than that at the central part. A high electric field magnitude of ~ 1.2 x 10^8 V/m at the cathode surface (not shown) was predicted. The movement of avalanching electrons to the right (anode) leaves a net positive charge close to the cathode and enhances that local field.
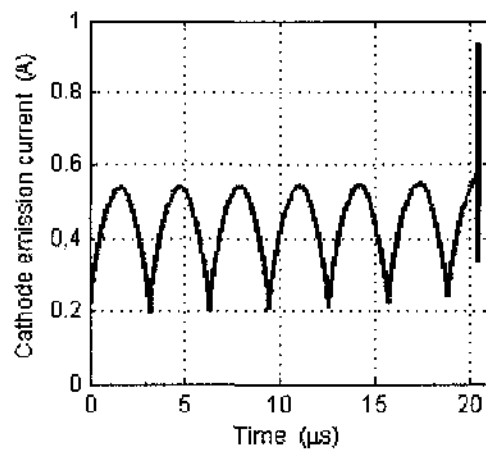
Figure 4-20. Time dependent cathode emission current corresponding to the voltage pulses of Figure 4-19.
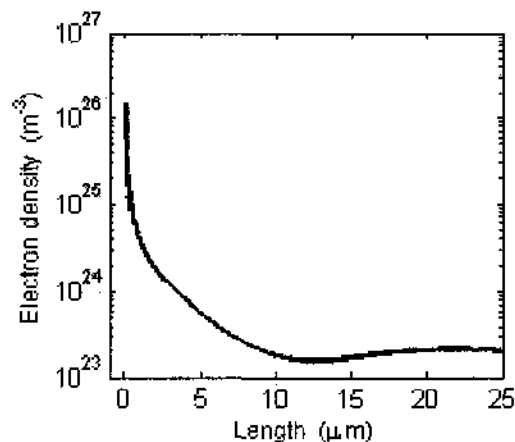
Figure 4-21. Electron density profile just prior to breakdown.

4.5 Results and Discussion on Nonlinear Transmission Line Simulations for Rise-Time Sharpening

Numerical simulations were also carried out to obtain the voltage dependent capacitance for a given BST sample. This work was to evaluate the possibility of rise-time decreases based on applying input voltages to transmission lines fabricated from barium strontium titanate material. Such rise-time shortening is very important for a number of high-voltage, pulsed-power applications. The overall analysis requires the following aspects: (a) analysis of the voltage across each individual grain boundary within the overall BST sample based on a Voronoi-type analysis; (b) evaluation of the voltage-dependent capacitance associated with each grain boundary; (c) computation of the overall sample capacitance with collective contributions from all the grain boundaries; (d) voltage waveform analysis based on a transmission-line model with the elemental capacitances appropriately chosen to reflect the overall BST sample capacitance.

Thus, the Voronoi network, described previously, was used as the basis for representing the internal structure with a mean GB size and variance. The corresponding non-linear capacitance has been given in Figure 3-10. All of the curves depicted in Figure 3-10 are monotonically decreasing with voltage. For the largest applied voltage amplitudes, the capacitance will be the smallest, and hence, the propagation velocity will be the highest ($velocity = 1 / \sqrt{LC}$).

The expected rise time for voltages applied to such a nonlinear transmission line and the pertinent controlling parameters can be evaluated through a simple analytical model. The analytic approach ignores interactions between various voltage components of the waveform. Thus, we consider a pulse of amplitude A injected into a nonlinear

transmission line of length l terminated with a matched resistance R_L. In the present case, R_L will depend on A in addition to the properties of the transmission line, for maximum power transfer. Let t_1 and t_2 denote the first times at which the voltage at $x=0$ equals 0.1A and 0.9A, respectively. Then, the 10-90% rise time of the input pulse is defined by: $\Psi_i \equiv t_2 - t_1$. For a lossless transmission line, the portion of the pulse with amplitude 0.1A

will propagate with velocity $v_1 = \dfrac{1}{\sqrt{LC(0.1A)}}$. Therefore, this portion of the pulse

(ignoring interactions) will reach the terminal end at time $\overline{t_1} = t_1 + \dfrac{l}{v_1}$. Similarly, the

portion of the pulse with amplitude 0.9A will reach the terminal end at: $\overline{t_2} = t_2 + \dfrac{l}{v_2}$,

where $v_2 = \dfrac{1}{\sqrt{LC(0.9A)}}$. Thus, the 10-90% rise time of the output pulse is:

$$\Psi_o \equiv \overline{t_2} - \overline{t_1} = \Psi_i + l\sqrt{L}\left[\sqrt{C(0.9A)} - \sqrt{C(0.1A)}\right]. \tag{4-2}$$

The rise-time at the output is lower than that at the input side, since the capacitance decreases monotonically with voltage amplitude. As evident from equation (4-2), sharpening of the output rise-time can be facilitated by: (i) increasing the transmission line length, (ii) increasing the inductance per unit length (L), and/or (iii) choosing the amplitude A of the input pulse that minimizes the function: $F(A) = \sqrt{C(0.9A)} - \sqrt{C(0.1A)}$. For the curves depicted in Figure 3-10, F is monotonically decreasing with amplitude A. Hence, increasing the input amplitude A decreases the output rise time.

Next, the effect of the transmission line on an input pulse was simulated according to the partial differential equation (PDE) given in Section 3.5.4. In particular, the transmission line parameters listed in Table 3-4 were used. The input pulse had a 60 V

amplitude, a rise time of 472 ns, and a 472 ns fall time. The simulation was performed for each grain size using the charge Equations (3-26) ~ (3-28). The terminal resistance R_L was varied for minimum back reflection for each dielectric type. The results obtained have been given in Table 4-5. Figure 4-22 plots the output produced at the terminal end when the dielectric was modeled according to Equation (3-26) with $R_L = 33.6 \ \Omega$. This plot of the output pulse and its rise-times agree with some reported experimental results obtained by Freeman and Karbowiak [95]. It may also be mentioned that a reduction in the rise time with some delay is clearly evident in the output voltage.

Table 4-5. Output rise-times and load resistances.

	Rise Time (ns)	C(V)	$R_L (\Omega)$
Input	472	-	-
Output 1	207/208	Equation (3-26)	33.6
Output 2	212/211	Equation (3-27)	23.6
Output 3	126/126	Equation (3-28)	19.3
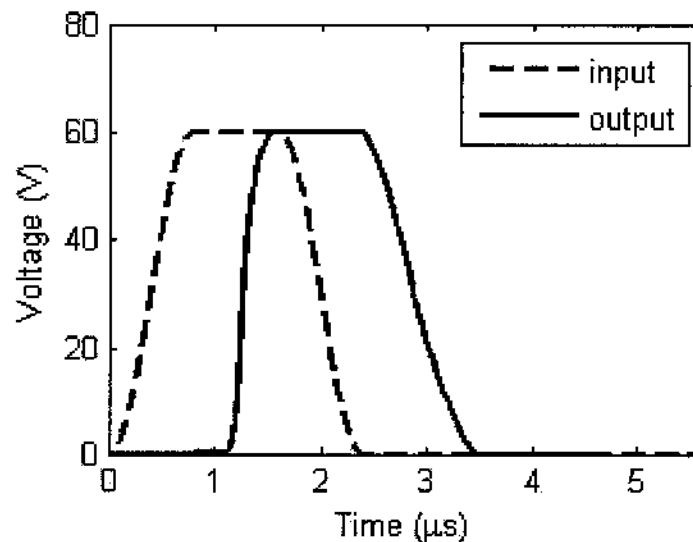
Figure 4-22. Rise time decrease and drop time increase after traveling through 10 meters of transmission line.

Table 4-5 shows both the simulated and theoretically expected rise times for the output pulse produced by the samples having the three different mean grain sizes. The expected rise-times were calculated according to Equations (4-2). The very close agreement between the numerical simulation results and the simple analytic expression helps validate the simulation scheme, its implementation and the output results.

Numerical simulations were also carried out to probe the effects of varying the resistance per unit length R, and conductance per unit length G. Though not shown here, the changes in R and G parameters were only seen to affect the ripple amplitude and its decay speed. The rise-times and sharpening effects were unaltered, as might be expected. Thus, the present results and the numerical scheme proposed here, appear to offer a very practical approach to the design and performance prediction of sharpening for pulsed-power applications. For completeness, it may be mentioned that the use of higher voltages and input pulse amplitudes would require the additional evaluation of potential breakdown and of electro-thermal effects. Such analyses could become important with higher pulsed power conditions and will be reported elsewhere.

Figure 4-23 shows the simulated output pulse produced by a transmission line subjected to a 60V input wave. The simulation was performed for a nonlinear transmission line modeled with the Table 3-4 parameters and a terminal resistance R_L = 33 Ω. In this case, the rise time of the input was 472 ns, while the predicted rise-time at the output end was roughly 208ns. Moreover, this simulation result was in close agreement with the experimental results listed by Wilson et al. [96].
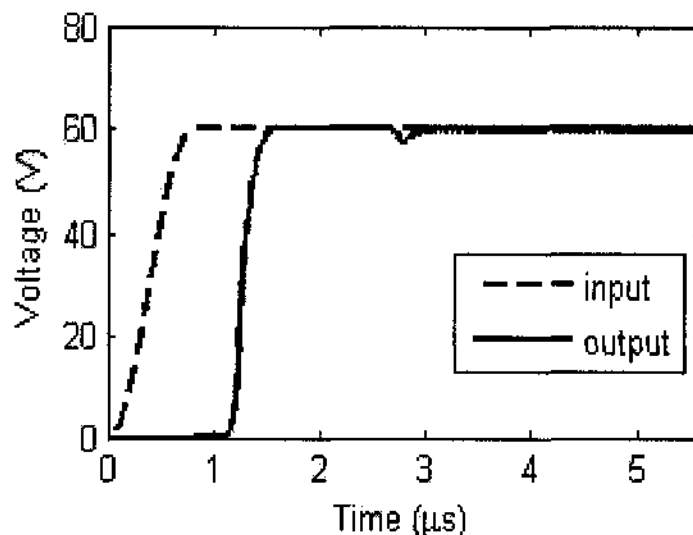
Figure 4-23. Rise time reduction after traveling through a 10-meter nonlinear BST transmission line.

Finally, given the voltage dependent propagation velocity of waves in such circuits, and the potential for waveform distortion, a simple analysis for the harmonic content was carried out for completeness. This was examined by choosing a standard sine wave function at the input of the transmission line model and evaluating the output waveform. Figure 4-24 shows the input and output waveforms. Some distortion and waveform change is clearly evident. The corresponding frequency spectrum is given in Figure 4-25. It shows that three harmonics are mainly present in the output. These are the 3rd, 5th, and 7th harmonics.
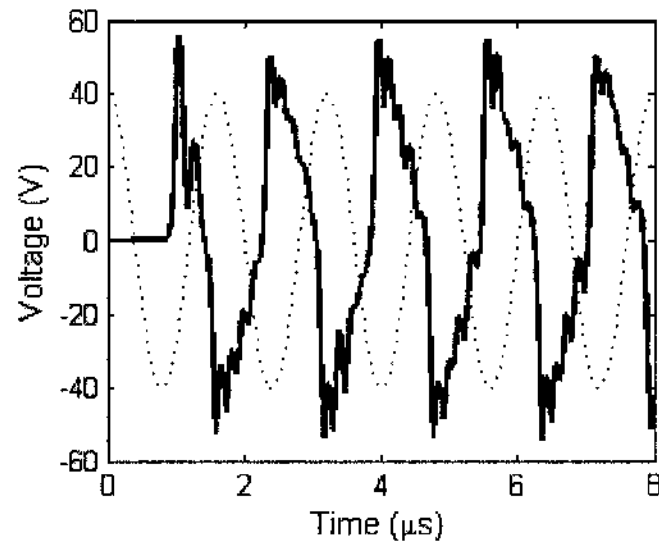
Figure 4-24. Calculated response to a sine-wave input.
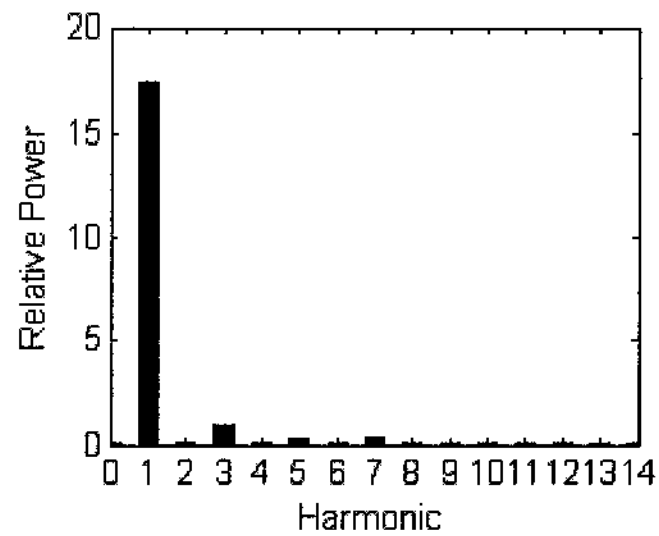
Figure 4-25. Frequency spectrum of the signal at the output of the nonlinear transmission line.

CHAPTER V

CONCLUSIONS AND FUTURE WORK

5.1   Research Summary

We have studied and analyzed the electrical and thermal characteristics of granular ZnO ceramics, probed TiO_2 breakdown under pulsed conditions, and analyzed BST (barium strontium titanate) based nonlinear transmission lines for their application in pulse sharpening. The primary focus was to study high field effects including breakdown and electro-thermal failure processes. In these studies, Voronoi networks were used not only in ZnO varistor simulations, but also in BST nonlinear capacitance analyses. It is shown to be a really powerful tool to study dielectric and semiconductor materials with granular microstructures.

(A)   For ZnO varistors, time-dependent, two-dimensional simulations based on random Voronoi networks have been developed to study the current-voltage characteristics, current spacial distribution, internal heating and related breakdown effects in response to high-voltage pulsing. Our simulations allowed for dynamic predictions of internal failures and tracking of the progression of hot-spots and thermal stresses in samples. The focus included effects of internal grain-size variations and the influence of relative internal disorder. The impact on several relevant electrical parameters and their scaling behavior was also examined. Though the numerical calculations were carried out for ZnO, the underlying theory and approach are general and could be applied to other nano-crystalline materials with internal grain boundaries as well.

Our results showed that application of high voltage pulsing can lead to internal ZnO melting. Such phase change is known to permanently damage the non-linear GB character associated with the Bi_2O_3 present in such material. The simulations also indicated an accelerated progression towards failure. Comparisons between relatively homogeneous (d=1) and more random (d=5) granular distributions were carried out. Our results demonstrated that parameters such as the device hold-off voltage, the average internal temperature, and average dissipated energy density would be higher with more uniform grains. This is beneficial from a practical device operational standpoint. The d=1 case was also predicted to produce lower thermal stresses and to allow for the application of longer duration pulses. Furthermore, it was shown that scaling down the average grain size offered similar advantages of increasing the device voltage hold-off capability, dramatic reductions in internal stresses and the advantage of tolerating longer pulses. The latter equivalently translates into higher voltage surge tolerance for a given pulse duration. While some of these results may be qualitatively intuitive, no quantitative assessment has previously been reported to our knowledge.

Finally, it was shown that for the situations studied, the principle failure mechanism would arise from internal localized melting and the transformation of grain boundary characteristics associated with the phase transitions. Thermal cracking was predicted to be absent with thermal stresses well below the requisite thresholds. Here again, the more uniform (d=1) granular configuration or the smaller average grain size were predicted to have inherent advantages. However, the important remaining question and issue in the ZnO varistor context is then material improvement and a more precise control over the fabrication technologies to achieve a more uniform granular configuration. This

processing aspect and the fabrication of smaller, yet more uniform grain sizes, will be an important research topic for the future.

On a final note, our simulation results and conclusions are based on ZnO varistors with micro-meter scale average grain sizes. For much smaller grain size, such as in the nano-meter scale, our conclusion may or may not be valid. This is an aspect that would currently be hard to compare and corroborate with physical data since there has not been much research or experimentation on nano-scale ZnO samples reported in the literature. However, with advances in processing and fabrication techniques, such results would begin to emerge. It would then also become possible to study, both experimentally and through simulations, the electrical and thermal characteristics of nano-scale ZnO varistors.

(B)   For TiO$_2$ electrical breakdown, numerical studies of current conduction and breakdown in TiO$_2$ were carried out based on a 1D, time-dependent model. Our results indicate that electrical breakdown of TiO$_2$ under multiple pulsed conditions can occur at *lower voltages* as compared to quasi-DC biasing, in agreement with experiments. Usually, the breakdown voltages are always higher under pulsing conditions, as compared to dc biasing. The experimentally obtained results were successfully explained using one possible mechanism. This involved the slow but continuous electron release from traps, followed by their impact ionization. We hypothesized that the lower breakdown voltages under pulsed conditions are direct rise-time effects, coupled with cumulative detrapping. In addition, the multi-pulse breakdown voltage has been shown to dramatically depend on the peak value of the applied pulse.

(C)   For nonlinear transmission line based on BST dielectric, the generation of high-voltage electrical pulses with very fast rise-times was probed. This is important for several pulsed power applications. A nonlinear transmission line approach to pulse sharpening was investigated based on numerical simulations of BST dielectrics. This is a relatively new, yet promising material with a high dielectric constant and a strong voltage dependent permittivity. Hence, it lends itself to macroscopic voltage-dependent capacitance variations. This allows for variable speeds for waveforms along the transmission lines, with the instantaneous velocities depending on the local voltage amplitude. The non-linear concept was based on utilizing the voltage-dependent capacitance of the granular material. The presence of internal grains in BST worked to increase the breakdown strength. These grains required the development of a more complicated and comprehensive model for performance predictions.

A Voronoi network representation was used to model the BST material with variable grains. The presence of a random number of internal grain boundaries was incorporated. The method is quite general and could be applied to other material systems as well.

Results were obtained for the nonlinear sample capacitances. The output characteristics of transmission lines based on such nonlinear material were then simulated. Our results clearly demonstrated rise-time shortening. The results were in agreement with previously published experimental data. Finally, it may also be mentioned that the present predictions apply as long as the input voltages are not excessively large. More complicated electro-thermal models may have to be developed for excessively large power applications. These would be similar in nature to schemes

developed by our group for ZnO varistors [90]. Besides, more sophisticated numerical techniques, such as those based on flux-corrected transport [97-99], might need to be applied for sub-nanosecond, ultra-high voltage pulse analysis. Both the spatial and temporal discretizations would become very small, while the voltage gradients could become excessively large for such analysis.

5.2 Future Work

Some useful and continued research in these and other interesting areas can be carried out. Elements of the modeling presented and discussed in this dissertation could also be extended. Some of the potential studies and modeling work relevant to the Voronoi network, nonlinear transmission line are briefly mentioned below. None of the following aspects were addressed in this dissertation, but they are very relevant and merit subsequent study.

1. After a period (such as several years) of usage, a ZnO varistor can be expected to degrade and age as internal defects may be generated with time. The origin of such defects would be the atomic displacement and migration due to energy deposition during high voltage and current surges in the device and circuits. Such defects would become electrically active and trap mobile carriers, leading to internal polarization and the creation of localized electric fields. Hence, it would be important and relevant to develop a fatigue and aging simulation model as an extension of our current simulation model of ZnO after suitable modifications. With such a model, it would become possible to predict the time-dependent failure

probabilities of ZnO varistors and estimate the times to failures. The modeling and simulation results would also provide some constructive instructions on the usage and maintenance of the ZnO varistor and arrestor. It is envisioned that the energy generation and temperature increases currently calculated in the melting would be the basis for Arrhenius-type, stochastic defect formation rates.

2. Extending our simulation tool of the Voronoi network to the simulation research of other granular structure materials, such as dielectrics, semiconductor materials, and even to tissues and cells of organism, will be very interesting. Actually Dr. R. P. Joshi and Dr. K. H. Schoenbach have begun using the Voronoi network to study the electrical breakdown of cell membranes in the context of tissues [100]. Such simulations would be very useful in predictions of irregularly shaped cells. In addition to the currently used 2D Voronoi network, a 3D Voronoi network will be more exact to represent grains and cells in the real world. For example, with a 3D Voronoi network, the voltage dependent capacitance of BST will be more valuable and comparable with experiment measurements, and it will make the design of a nonlinear transmission line more practical. The influence of aspect ratios would also be made available.

3. The topic of pulse-sharpening using BST based nonlinear transmission lines also merits further research. In this dissertation, the amplitude of voltage pulse was taken to be less than 100V. For more useful, interesting and applicable scenarios in the "pulsed-power" field, this amplitude would need to be increased to the kilo-Volt and Mega-Volt ranges. With such high voltages, both the electrical breakdown and internal Joule heating can be expected to become important factors affecting the

BST characteristics and its voltage dependent capacitance. In addition, with high voltage amplitudes, a much stronger voltage and electric-field gradients can conceivably arise within the device subjected to such voltages. The numerical calculations may then run into stability problems due to the existence of sharp local gradients. This is a well known problem in shock-wave analysis. Under this extreme condition, more complicated electro-thermal models and numerical schemes (e.g., the flux corrected transport methods) may have to be developed and applied.

REFERENCES

1. K. Eda, "Zinc oxide varistors," *IEEE Electrical Insulation Magazine*, vol. 5, no. 6, pp. 28-41, 1989.

2. P. J. Hansen, V. Vaithyanathan, Y. Wu and T. Mates, S Heikman, U. K. Mishra, R. A. York, D. G. Schlom, and J. S. Speck, "Rutile films grown by molecular beam epitaxy on GaN and AlGaN/GaN," *the Journal of Vacuum Science and Technology B*, vol. 23, no. 2, pp. 499-506, 2005.

3. P. Castro, J. Buchenauer, J. Gaudet, and E. Schamiloglu, "Studies of dielectric breakdown under pulsed power conditions," *Proceedings of 15th IEEE Pulsed Power Conference* (Monterey, USA), pp. 978-981, 2005.

4. Y. C. Chen, S. C. Wang, and J. Y. Lin, "Tunable capacitor composed of Al_2O_3-doped barium strontium titanate for application in voltage control oscillator," *Japanese Journal of Applied Physics*, vol. 46, pp. 1557-1561, 2007.

5. S. C. Huang, H. M. Chen, S. C. Wu, and J. Y. Lee, "Time dependent dielectric breakdown of paraelectric barium-strontium-titanate thin film capacitors for memory device applications," *Journal of Applied Physics*, vol. 84, pp. 5155-5157, 1998.

6. M. Matsuoka, "Nonohmic properties of zinc oxide ceramics," *Japan Journal of Applied Physics*, vol. 10, pp. 736-746, 1971.

7. http://varistortechnology.com/

8. G. D. Mahan, L. M. Levinson, and H. R. Philipp, "Theory of conduction in ZnO varistors," *Journal of Applied Physics*, vol. 50, no. 4, pp. 2799-2812, 1979.

9. S. C. Pillar, J. M. Kelly, D. E. McCormack, P. O'Brien and R. Ramesh, "The effect of processing conditions on varistors prepared from nano-crystalline ZnO," *Journal of Materials Chemistry*, vol. 13, pp. 2586-2590, 2003.

10. M. Tao, Bui Ai, O. Dorlanne, and A. Loubiere, "Different 'single grain junction' within a ZnO varisotr", *Journal of Applied Physics*, vol. 61, no. 4, pp.1562-1567, 1987.

11. M. Bartkowiak, G. D. Mahan, F. A. Modine, M. A. Alim, R. Lauf and A. McMillan, "Voronoi network model of ZnO varistors with different types of grain boundaries," *Journal of Applied Physics*, vol. 80, no. 11, pp. 6516-6522, 1996.

    M. Bartkowiak, G. D. Mahan, F. A. Modine, and M. A. Alim, "Influence of ohmic grain boundaries in ZnO varistors," *Journal of Applied Physics*, vol. 79, no. 1, pp. 273-281, 1996.

12. Q. Chen, J. He, K. Tan, S. Chen, M. Yan and J. Tang, "Influence of grain size on distribution of temperature and thermal stress in ZnO varistor ceramics", *Science in China (Series E)*, vol. 45, no. 4, pp 337-347, 2002.

13. J. He, R. Zeng, Q. Chen, S. Chen, Z. Guan, S. Han, and H. Cho, "Nonuniformity of electrical characteristics in microstructures of ZnO surge varistors," *IEEE Transactions on Power Delivery*, vol. 19, no. 1, pp.138-144, 2004.

14. E. Olsson, G. L. Dunlop, and R. Osterlund, "Development of functional microstructure in ZnO varistor material," in Advances in Varistor Technology (L. M. Levinson, ed.), vol. 3, *Ceramic Transactions*, pp. 57-64, The American Ceramic Society Inc., 1988.

15. J. T. C. van Kemenade and R. K. Eijinthoven, "Direct determination of barrier voltage in ZnO varistors," *Journal of Applied Physics*, vol. 50, no. 2, pp. 938-941, 1979.

16. E. Olsson, L. K. L. Falk, G. L. Dunlop, and R. Osterlund, "The microstructure of a ZnO varistor material," *Journal of Materials Science*, vol. 20, pp. 4091-4098, 1985.

17. H. Cerva and W. Russwurm, "Microstructure and crystal structure of bismuth oxide phases in zinc oxide varistor ceramics," *Journal of the American Ceramic Society*, vol. 71, pp. 522-530, 1988.

18. W. D. Kingery, J. B. Vander Sande, and T. Mitamura, "A scanning transmission electron microscopy investigation of grain-boundary segregation in a ZnO-Bi2O3 varistor," *Journal of the American Ceramic Society*, vol. 62, pp. 221-222, 1979.

19. F. Stucki, P. Bruesch, and F. Greuter, "Electron spectroscopic studies of electrically active grain boundaries in ZnO," *Surface Science*, vol. 189/190, pp. 294-299, 1987.

20. L. M. Levinson and H. R. Philipp, " The physics of metal oxide varistors," *Journal of Applied Physics*, vol. 46, pp. 1332-1341, 1975.

21. J. O. Levine, "Theory of varistor electronic properties," *CRC Critical Reviews in Solid State Sciences*, vol. 5, pp. 597-608, 1975.

22. W. G. Morris, "Physical properties of electrical barriers in varistors," *Journal of Vacuum Science & Technology*, vol. 13, pp. 926-931.

23. J. Bernasconi, S. Strassler, B. Knecht, H. P. Klein, and A. Menth, "Zinc oxide based varistors: a possible mechanism," *Solid State Communications*, vol. 21, pp. 867-870, 1977.

24. P. L. Hower and T. K. Gupta, "A barrier model for ZnO varistors," *Journal of Applied Physics*, vol. 50, pp. 4847—4855, 1979.

25. P. R. Emtage, "The physics of Zinc Oxide varistors," *Journal of Applied Physics*, vol. 48, pp. 4372-4383, 1977.

26. K. Eda, "Conduction mechanism of non-ohmic zinc oxide ceramics," *Journal of Applied Physics*, vol. 49, pp. 2964-2972.

27. R. Einzinger, "Metal oxide varistor action - a homojunctions breakdown," *Applications of Surface Science*, vol. 1, pp. 329-340, 1978.

28. R. Einzinger, "Grain junction properties of ZnO varistors," *Applications of Surface Science*, vol. 3, pp. 390-408, 1979.

29. G. E. Pike, "Electronic properties of ZnO-varistors: a new model," *Materials Research Society Proceedings*, vol. 5, pp. 369-379, 1982.

30. G. E. Pike, "Semiconductor grain boundary admittance: theory," *Physical Review B*, vol. 30, pp. 795-802, 1984.

31. G. E. Pike, S. R. Kurtz, and P. L. Gourley, "Electroluminescence in ZnO varistors: Evidence for hole contributions to the breakdown mechanism," *Journal of Applied Physics*, vol. 57, pp. 5512-5518, 1985.

32. G. Blatter and F. Greuter, "Carrier transport through grain boundaries in semiconductors," *Physical Review B*, vol. 33, pp. 3952-3966, 1986.

33. G. Blatter and F. Greuter, "Electrical breakdown at semiconducting grain boundaries," *Physical Review B*, vol. 34, pp. 8555-8572, 1986.

34. K. Eda, "Electrical properties of ZnO- Bi2O3 metal oxide heterojunctions- A clue of a role of intergranular layers in ZnO varistors," in *Materials Research Society*

Symposia Proceedings: Grain Boundaries in Semiconductors, edited by H. J. Leamy, G. E. Pike, and C. H. Seager, New York: Elsevier, pp. 381-392, 1982.

35. H. R. Philipp, G. D. Mahan, and L. M. Levinson, "Advanced metal oxide varistor concepts," Final Report ORNL/Sub/84-17457/1, 1984.

36. Y. Suzuoki, A. Ohki, T. Mizutani, and T. Ieda, "Electrical properties of ZnO-Bi2O3 thin film varistors," *Journal of Physics D: Applied Physics*, vol. 20, pp. 511-517, 1987.

37. K. Eda, "Destruction mechanism of ZnO varistors due to high currents," *Journal of Applied Physics*, vol. 56, pp. 2948-2955, 1984.

38. M. Bartkowiak, M. G. Comber, and G. D. Mahan, "Energy handling capability of ZnO varistors, " *Journal of Applied Physics*, vol. 79, pp. 8629-8633, 1996.

39. M. Bartkowiak, M. G. Comber, and G. D. Mahan, "Failure modes and energy absorption capability of ZnO varistors," *IEEE Transactions on Power Delivery*, vol. 14, no.1, pp. 152-162, 1999.

40. M. V. Lat, "Thermal properties of metal oxide surge arresters," *IEEE Transactions on Power Apparatus and Systems*, vol. PAS-102, no. 7, pp. 2194-2202, 1983.

41. A. Vojta and D. R. Clarke, "Microstructural origin of current localization and "puncture" failure in varistor ceramics," *Journal of Applied Physics*, vol. 81, pp. 985-993., 1997.

42. M. A. Ramirez, P. R. Bueno, W. C. Ribeiro, J. A. Varela, D. A. Bonett, J. M. Villa, M. A. Marquez and C. R. Rojo, "The failure analyses on ZnO varistors used in high tension devices," *Journal of Materials Science*, vol. 40, pp. 5591-5596, 2005.

43. M. Bartkowiak, M. G. Comber, and G. D. Mahan, "Influence of Nonuniformity of ZnO varistors on their energy absorption capability," *IEEE Transactions on Power Delivery*, vol. 16, no.4, pp.591-598, 2001.

44. M. Bartkowiak and G. D. Mahan, "Nonlinear currents in Voronoi networks", *Physical Review B*, vol. 51, no.16, pp.10825-10832.

45. G. E. Pike and C. H. Seeger, "The dc voltage dependence of semiconductor grain-boundary resistance," *Journal of Applied Physics*, vol. 50, no. 5, pp. 3414- 3422, 1979.

46. R. P. Joshi and R. F. Wood, "Molecular dynamics Monte Carlo simulations of grain boundary electron transport in n-silicon," *Journal of Applied Physics*, vol. 84, no. 6, pp. 3197-3206, 1998.

27. S. Li, J. Li, F. Liu, M. A. Alim, and G. Chen, "The dimensional effect of breakdown field in ZnO varistors," *Journal of Physics D: Applied Physics*, vol. 35, no. 15, pp. 1884-1888, 2002.

48. C. L. Li, T. M. Barton, and R. E. Miles, "Avalanche breakdown and surface deep-level trap effects in GaAs MESFET's," *IEEE Transactions on Electron Devices*, vol. 40, no. 4, pp.811-816, 1993.

49. T. M. Barton, C. M. Snowden, J. R. Richardson, and P. H. Ladbrooke, "Narrow pulse measurement of drain characteristics of GaAs MESFETs," *Electronics Letters*, vol. 23, no. 13, pp. 686-687, 1987.

50. For example, J. T. Krile, A. A. Neuber, J. C. Dickens, and H. G. Krompholz, "DC and Pulsed Dielectric Surface Flashover at Atmospheric Pressure," *IEEE Transactions on Plasma Science*, vol. 33, no.4, pp. 1149-1154, 2005.

51. K. H. Schoenbach, B. Hargrave, R. P. Joshi, J. F. Kolb, C. Osgood, R. Nuccitelli, A. Pakhomov, J. Swanson, M. Stacey, J. A. White, S. Xiao, J. Zhang, S. J. Beebe, P. F. Blackmore, and E. S. Buescher, "Bioelectric effects of intense nanosecond pulses," *IEEE Transactions on Dielectrics and Electrical Insulation*, vol. 14, pp. 1088-1109, 2007.

52. Yu. V. Aristov, V. B. Voronkov, I. V. Grekhov, A. K. Kozlov, S. V. Korotkov, and A. G. Lyublinskii, "A high-power semiconductor switch of high-voltage pulses with a rise time of nanosecond duration," *Instruments and Experimental Techniques*, vol. 50, pp. 224–227, 2007.

53. I. V. Grekhov, V. M. Efanov, A. F. Kardo-Sysoev, and S. V. Shenderei, "Power Drift Step Recovery Diodes (DSRD)," *State Electronics*, vol. 28, pp. 597-599, 1985.

54. R. J. Focia, E. Schamiloglu, and C. B. Fleddermann, "Simple techniques for the generation of high peak power pulses with nanosecond and sub-nanosecond rise times," *Review of Scientific Instruments*, vol. 67, pp. 2626-2629, 1996.

55. G. M. Loubriel, W. D. Helgeson, D. L. McLaughlin, M. W. O'Malley, F. J. Zutavern, A. Rosen, and P. J. Stabile, "Triggering GaAs Lock-On switches with laser diode arrays," *IEEE Transactions on Electron Devices*, vol. 38, pp. 692-695, 1991.

56. D. M. Giorgi, A. H. Griffin, D. E. Hargis, I. A. McIntyre, and S. F. Zucker, "High power, light activated switching: experiment and applications," *Proc. 8th IEEE Pulsed Power Conference*, ed K Prestwich and R White (New York: IEEE), pp 122–125, 1991.

57. W. R. Cravey, E. K. Freytag, D. A. Goerz, P. Poulsen, and P. A. Pincosy, "Picosecond high pressure gas switch experiment," *Proc. 9th IEEE International Pulsed Power Conference*, ed K Prestwich and W Baker (New York: IEEE), pp 483–486, 1993.

58. P. Champney, D. A. Curry, C. C. Eichenberger, and J. Fockler, "The Development and testing of subnanosecond-rise, kilohertz oil switches," *Proceedings of 8th IEEE International Pulsed Power Conference*, ed K Prestwich and R White (New York: IEEE), pp 863–869, 1991.

59. K. H. Schoenbach, J. F. Kolb, S. Xiao, S. Katsuki, Y. Minamitani, and R. P. Joshi, "Electrical breakdown of water in small gaps," to appear in *IEEE Transactions on Dielectrics and Electrical Insulation*, August 2007.

60. S. Xiao, J. Kolb, S. Kono, S. Katsuki, R. P. Joshi, M. Laroussi, and K. H. Schoenbach, "High power water switches: postbreakdown phenomena and dielectric recovery," *IEEE Transactions on Dielectrics and Electrical Insulation*, vol. 11, pp. 604-612, 2004.

61. N. D. Jameroski, J. M. Lehr, J. R. Woodworth, J. R. Blickem, K. C. Hodge, Z. R. Wallace, V. Anaya, J. P. Corley, and J. A. Lott, "Multimegavolt laser-triggered gas switching with a green laser and beam transport through water," *IEEE Transactions on Plasma Science*, vol. 35, pp. 696-701, 2007; and references therein.

62. J. Qian, R. P. Joshi, J. Kolb, K. H. Schoenbach, J. Dickens, A. Neuber, H. Krompholz, E. Schamiloglu, and J. Gaudet, "Micro-Bubble based model analysis of liquid breakdown initiation by a sub-microsecond pulse," *Journal of Applied Physics*, vol. 97, 113304/1-113304/9, 2005.

63. N. M. Jordan, Y. Y. Lau, D. M. French, R. M. Gilgenbach, and P. Pengvanich, "Electric field and electron orbits near a triple point," *Journal of Applied Physics,* vol. 102, pp. 033301/1-033301/10, 2007.

64. I. G. Katayev, *Electromagnetic Shock Waves.* London: Iliffe, 1966.

65. N. Seddon and E. Thornton, "A high-voltage, short-risetime pulse generator based on a ferrite pulse sharpener," *Review of Scientific Instruments,* vol. 59, pp. 2497-2498, 1988.

66. T. M. Benson, R. Pouladian-Kari, and A. J. Shapland, "Novel operation of ferrite loaded coaxial lines for pulse sharpening applications," *Electron. Lett.,* vol. 27, pp. 861–863, 1991.

67. M. J. W. Rodwell, M. Kamegawa, R. Yu, M. Case, E. Carman, and K. Giboney, "GaAs nonlinear transmission lines for picosecond pulse generation and millimeter-wave sampling," *IEEE Transactions on Microwave Theory Techniques,* vol. 39, pp. 1194–1204, 1991.

68. E. Afshari and A. Hajimiri, "Nonlinear transmission lines for pulse shaping in silicon," *IEEE Journal of Solid-State Circuits,* vol. 40, pp. 744-752, 2005.

69. R. Landauer, "Parametric Amplification along Nonlinear Transmission Lines," *J. Appl Phys,* vol. 31, pp. 479-484, 1960; S. T. Peng and R. Landauer, "Effects of dispersion on steady state electromagnetic shock profiles," *IBM Journal of Research and Development,* vol. 17, pp. 299-306, 1973.

70. G. Branch and P. W. Smith, "Fast-rise-time electromagnetic shock waves in nonlinear, ceramic dielectrics," *Journal of Physics D: Applied Physics,* vol. 29, 2170–2178, 1996.

71. D. E. Kotecki, J. D. Baniecki, H. Shen, R. B. Laibowitz, K. L. Saenger, J. J. Lian, T. M. Shaw, S. D. Athavale, C. Cabral, Jr., P. R. Duncombe, M. Gutsche, G. Kunkel, Y. J. Park, Y. Y. Wang, and R. Wise, "(Ba,Sr)TiO$_3$ dielectrics for future stacked-capacitor DRAM," *IBM Journal of Research and Development*, vol. 43, pp. 367-382, 1999.

72. B. Acikel, T. R. Taylor, P. J. Hansen, J. S. Speck, and R. A. York, "A new high performance phase shifter using Ba$_x$Sr$_{1-x}$TiO$_3$ thin films," *IEEE Microwave and Wireless Components Letters*, vol. 12, pp. 237-239, 2002.

73. S. W. Kirchoefer, E. J. Cukauskas, N. S. Barker, H. S. Newman, and W. Chang, "Barium – strontium – titanate thin films for application in radio-frequency-microelectromechanical capacitive switches," *Applied Physics Letters*, vol. 80, pp. 1255-1257, 2002.

74. N. K. Pervez, P. J. Hansen, and R. A. York, "High tunability barium strontium titanate thin films for RF circuit applications," *Applied Physics Letters*, vol. 85, pp. 4451-4453, 2004.

75. Q. Wen and D. R. Clarke, "Modeling the electrical characteristics of polycrystalline varistors using individual grain boundary properties," in *Ceramic Translations*, vol. 41, Grain Boundaries and Interfaces in Electronic Ceramics, pp. 217-230, 1994.

76. D. Weaire and N. Rivier, "Soap, cells and statistics - random patterns in two dimensions," *Contemporary Physics*, vol. 25, pp. 59-99, 1984.

77. M. V. Lat, "Thermal Properties of Metal Oxide Surge Arresters", *IEEE Transactions on Power Apparatus and Systems*, vol. 102, pp. 2194-2202, 1983.

78. W. B. Joyce, "Thermal Resistance of Heat Sinks With Temperature-Dependent Conductivities," *Solid State Electronics*, vol. 18, pp 321-322, 1975.

79. Y. S. Touloukian, R. W. Powell, C. Y. Ho, and P. G. Klemens, "Thermal-Physical Properties of Matter," IFI/Plenum, New York, vol.2, pp.243-245, 1970.

80. B. A. Boley and J. H. Weiner, Theory of Thermal Stresses, John Willey & Sons, Inc., New York, Chapter 5, 1960.

81. J. Nelson, "Continuous-time random-walk model of electron transport in nanocrystalline TiO2 electrodes," *Physical Review B*, vol. 59, pp. 15374-15380, 1999.

82. F. A. Grant, "Properties of Rutile (Titanium Dioxide)," *Review of Modern Physics*, vol. 31, no. 3, pp. 646-674, 1959.

83. P. E. de Jongh and D. Vanmaekelbergh, "Trap-Limited Electronic Transport in Assemblies of Nanometer-Size TiO2 Particles," *Physical Review Letter*, vol. 77, no. 16, pp. 3427-3430, 1996.

84. R. G. Breckenridge and W. R. Hosler, *Physical Review*, vol. 91, no. 4, pp. 793-802, 1953.

85. R. Konenkamp, "Carrier transport in nanoporous TiO2 films," *Physical Review B*, vol. 61, no. 16, pp. 11057-11064, 2000.

86. P. A. Montano, G.W. Fernando, B. R. Cooper, E. R. Moog, H. M. Naik, S. D. Bader, Y. C. Lee, Y. N. Darici, H. Min, and J. Marcano, "Two magnetically different, closely lying states of fcc iron grown on copper (100)," *Physical Review Letters*, vol. 59, no. 9, pp. 1041-1044, 1987.

87. S. M. Sze, *Physics of Semiconductor Devices*, 2nd edition. (Wiley, New York, 1981).

88. R. B. Darling, "Electrostatic and current transport properties of n+/semi-insulating GaAs junctions," *Journal of Applied Physics*, vol. 74, no. 7, pp. 4571-4589, 1993.

89. I. A. Khan and J. A. Cooper, Jr., "Measurement of high-field electron transport in silicon carbide," *IEEE Transactions on Electron Devices*, vol. 47, no. 2, pp. 269-273, 2000.

90. G. Zhao, R. P. Joshi, V. K. Lakdawala, and H. Hjalmarson, "Electro-Thermal Simulation Studies for Pulse Induced Energy Absorption in Nano-Crystalline ZnO Varistors," *IEEE Transactions on Dielectrics and Electrical Insulation*, vol. 14, pp. 1007-1015, 2007.

91. J. H. Lee and S. W. Rhee, "Chemical vapor deposition of barium strontium titanate films with direct liquid injection of single-mixture solution", *Journal of The Electrochemical Society*, vol. 146, pp. 3783-3787, 1999.

92. H. D. Park and D. A. Payen, "Grain Boundary Phenomena in Electronic Ceramics" (American Ceramic Society, Columbus, 1981), vol. 1, p. 242.

93. K. Mukae, K. Tsuda, and I. Nagasawa, "Capacitance-vs-voltage characteristics of ZnO varistors," *Journal of Applied Physics*, vol. 50, pp. 4475-4476, 1979.

94. G. Zhao, R. P. Joshi, and V. K. Lakdawala, "Percolative breakdown model for ceramics based on a random grain-boundary network", *Proceedings of 2005 IEEE Conference on Electrical Insulation and Dielectric Phenomena* (Nashville, Tennessee), pp. 544-547.

95. R. H. Freeman and A. E. Karbowiak, "An investigation of nonlinear transmission lines and shock waves", *Journal of Physics D: Applied Physics*, vol. 10, pp. 633-643, 1977.

96. C. R. Wilson, M. M. Turner, and P. W. Smith, "Pulse sharpening in a uniform LC ladder network containing nonlinear ferroelectric capacitors", *IEEE Transactions on Electron Devices*, vol.38, pp. 767-771, 1991.

97. J. P. Boris and D. L. Book, "Flux-Corrected Transport I. SHASTA, A fluid Transport Algorithm That works," *Journal of Computational Physics*, vol. 11, no. 1, pp. 38-69, 1973.

98. D. L. Book, J. P. Boris, and K. Hain, "Flux-Corrected Transport II: Generalizations of the method," *Journal of Computational Physics*, vol. 18, pp. 248-283, 1975.

99. J. P. Boris and D. L. Book, "Flux-Corrected Transport III. Minimal-Error FCT Algorithms," *Journal of Computational Physics*, vol. 20, pp. 397-431, 1976.

100. R. P. Joshi, A. Mishra, and K. H. Schoenbach, "Model Assessment of Cell Membrane Breakdown in Clusters and Tissues Under High-Intensity Electric Pulsing," *IEEE Transactions on Plasma Science* – special issue on "Nonthermal Medical /Biological Applications Using Ionized Gases and Electromagnetic Fields", currently under review.

VITA

Guogang Zhao

EDUCATION

- Ph.D. in Electrical & Computer Engineering, Old Dominion University, Norfolk, VA, USA, 2007
- M.S. in Electrical Engineering, China Electric Power Research Institute, Beijing 100085 China, 1994
- B.S. in Electrical Engineering, Tsinghua University, Beijing 100084 China, 1991.

PAPERS PUBLISHED

1. G. Zhao, R. P. Joshi, V. K. Lakdawala, and H. P. Hjalmarson, "Electro-Thermal Simulation Studies for Pulsed Voltage Induced Energy Absorption and Potential Failure in Microstructured ZnO Varistors," *IEEE Transactions on Dielectrics and Electrical Insulation*, vol.14, no.4, pp.1007-1015, August 2007.
2. G. Zhao, R. P. Joshi, V. K. Lakdawala, E. Schamiloglu, and H. Hjalmarson, "TiO2 breakdown under pulsed conditions," *Journal of Applied Physics*, vol. 101, 026110 (2007).
3. R. P. Joshi, J. Qian, G. Zhao, J. Kolb, and K. H. Schoenbach, "Are microbubbles necessary for the breakdown of liquid water subjected to a submicrosecond pulse?" *Journal of Applied Physics*, vol. 96, 5129 (2004).
4. R. P. Joshi, G. Zhao, and H. P. Hjalmarson, "Electro-Thermal Simulation Studies for Pulsed Voltage Induced Energy Absorption and Potential Failure in Microstructured ZnO Varistors," *2007 IEEE International Pulsed Power and Plasma Science Conference proceedings*, in printing
5. G. Zhao, R. P. Joshi, V. K. Lakdawala, E. Schamiloglu, and H. Hjalmarson, "Studies of TiO2 Breakdown Under Pulsed Conditions," *2006 IEEE CEIDP conference proceedings*, pp. 349-352.
6. G. Zhao, R. P. Joshi, and V. K. Lakdawala,, "Percolative breakdown model for ceramics based on a random grain-boundary network", *2005 IEEE CEIDP conference proceedings*, pp. 544-547.
7. Su Zhiyi, Zhao Guogang, Liu Simei, Zhu Gengfu, Lin Chengan, "A model system of pollutant accumulation on transmission and transformation equipment related to the atmospheric diffusion in urban and typical industrial areas", *1998 International Conference on Power System Technology proceedings*, vol.1, pp. 543-546.